# Investigation of Liquid Metal Embrittlement in Advanced High Strength Steels

by

Liu He

A thesis

presented to the University of Waterloo

In fulfillment of the

thesis requirement for the degree of

Master of Applied Science

in

Mechanical and Mechatronics Engineering

Waterloo, Ontario, Canada, 2020

©Liu He 2020

# Author's Declaration

This thesis consists of materials all of which I authored or co-authored: See Statement of Contributions included in the thesis. This is a true copy of the thesis, including any required final revisions, as accepted by my examiners.

I understand that my thesis may be made electronically available to the public.

# Statement of Contributions

This thesis was solely written by the candidate. Professors N. Zhou and E. Biro contributed to editing the entire thesis. Additional contributions were made by other members of the Centre for Advanced Material Joining research group. Specific contributions to this work, other than those already noted, are listed below.

Chapter 6 of this thesis is based on a journal paper which has been published in *Science and Technology of Welding:*

> L. He, C. DiGiovanni, X. Han, C. Mehling, E. Wintjes, E. Biro & N.Y. Zhou, "Suppression of liquid metal embrittlement in resistance spot welding of TRIP steel." Sci. Technol. Weld. Join. 2019;24:579–586.

The experimental design, analysis, and writing were conducted soley by the candidate. The paper was co-authored by the candidiate, Mr. C. DiGiovanni, Mr. X. Han, Mr. C. Mehling, Ms. E. Wintjes, Prof. E. Biro and Prof. N.Y. Zhou. Prof. Biro and Prof. Zhou both participated in technical discussions and editing of the manuscript.

# Abstract

Third-generation advanced high strength steels (AHSS) are typically given a zinc coating that provides excellent resistance to corrosion. During the resistance spot welding (RSW) process, the melted zinc coating enables liquid metal embrittlement (LME) where the liquid zinc, acting as an embrittling agent, induces cracking in the weld indent, compromising weld strength. This work investigates the various factors that influence LME in AHSS and provides a viable solution to suppress LME.

Hot tensile testing was first used to evalute the LME susceptiblility of the studied steels. It was discovered that the austenite content of the steels' microstructure, Si content in the steels' chemistry and the type of Zn coating all influence the behavior of the ductility trough of the examined steels. As the austenite content of the steel increased, the ductility loss caused by LME increased as well. Approximately 18 vol.% to 31 vol.% austenite is the minimum amount required to trigger the rise in ductility loss of all the studied steels. In addition, steels containing a low Si content are more likely to form a layer of Fe-Zn intermetallic that acts as a barrier to suppresses LME at temperatures below 670°C. It was also discovered that the GA coated steels are far less susceptible to LME than their GI coated counterparts due to it being thinner and containing 25 wt.% Fe in its coating.

A mathematical model capable of estimating the crack index within the weld lobe of each material was also developed through resistance spot welding. The model showed that the weld lobe of materials where not equally affected by LME. Furthermore, it identified regions within the weld lobe where welds of sufficient size could be made while minimizing LME cracks.

Using the hot tensile testing data and the results from RSW, LME susceptibility of the studied steels are ranked. QP1180GA is the most LME susceptible steel while DP980GA is the least. The ductility loss obtained via hot tensile testing shows good correlation with the intensity of LME cracks found in resistance spot welds.

Finally, LME was suppressed in AHSS by placing aluminum interlayers added between the electrode and steel contact surface. Compared to welds exhibiting LME, TRIP 1100 with aluminum interlayers showed complete strength recovery while TRIP 1200 with aluminum interlayers resulted in a recovery of strength by 90%. Aluminum interlayers suppress LME of TRIP steel by formation of iron aluminides that hinder liquid zinc from coming in contact with the steel substrate, thus preventing LME.

# Acknowledgements

I would first like to thank my supervisors, Prof. Norman Zhou and Prof. Elliot Biro for their time, guidance and support throughout my master's study. I grew as a person under their guidance.

Secondly, I would like to thank Mr. Mark Griffett and Mr. Mark Whitney for their time and assistance in the materials labotory. They are invaluable to CAMJ and a great reservior of practial engineering knowledge.

I also wish to acknowledge my colleagues in the CAMJ research group, especialy Chris Digiovanni, Xu Han, James Choi, Erica Wintjes, Bruna Figueredo and our newest additon Ali Ghatei Kalashami! I enjoyed everyday at the office with you guys. I am going to look back at this period in my life foundly.

In addition, I would like to thank my Co-op students Cornnor Mehling, Urban Pistek, Connor Hawkins, and Jan Dabrowski for their hard work on the project. I am not the greatest supervisor in the world and I did make mistakes along the way. I hope you guys grew under my leadership and become great engineers in the future!

Finally, I wish to thank my friends and family for all their support and encouragement, without which I would not be able to complete this degree.

# Table of Contents

# List of Figures

# List of Tables

# List of Abbreviations

| | |
|---|---|
| AHSS | Advanced high strength steel |
| ANOVA | Analysis of variance |
| AWS | American Welding Society |
| DP | Dual phase |
| EDX | Energy dispersive x-ray spectroscopy |
| GA | Hot-dip galvannealed |
| GI | Hot-dip galvanized |
| LME | Liquid metal embrittlement |
| MFDC | Medium frequency direct current |
| MWS | Minimum weld size |
| QP | Quench and partition |
| RSW | Resistance spot welding |
| SEM | Scanning electron microscope |
| TRIP | Transformation induced plasticity |
| TWIP | Twinning induced plasticity |
| UTS | Ultimate tensile strength |
| YS | Yield strength |

# Chapter 1 Introduction

## 1.1 Background

In 2004, Moomba Gas Plant, South Australia, a fire caused by a mechanical failure led to the hospitalization of four workers and the death of one. What triggered the mechanical failure was a phenomenon called liquid metal embrittlement (LME) [1]. Liquid metal embrittlement is where certain metals experience loss in mechanical properties due to exposure to specific liquid metals [2]. Liquid metal embrittlement is also a safety concern during automotive manufacturing. During body-in-white assembly, resistance spot welding (RSW) is used to join galvanized automotive steels. The combination of welding process and auto material triggers liquid metal embrittlement in the weld which leads to a loss in its mechanical performance [3]. At the moment, it is uncertain what types of auto steels are susceptible to LME and the degree at which mechanical performance of the weld is affected. This uncertainty poses a safety concern for automotive manufactures. As a result, there is a need to better understand liquid metal embrittlement in automotive steels and the methods to suppress it.

## 1.2 Objectives

The objective of this thesis is to investigate the various factors that influence LME in AHSS and provide a viable solution to suppress LME. The specific objectives are as follows:

1. Explore the factors that influence LME only from a materials level through hot tensile testing.
2. Investigate the LME susceptibility of AHSS in a welding environment. Use the welding results to validate the hot tensile testing method.
3. Propose a method to suppress LME cracking and investigate its effectiveness and suppression mechanism

## 1.3 Criteria and constraints

The resistance spot welding parameters used in this study were based on the Automotive and Steel Partnership standard, and the American Welding Society standard [4,5]. Details regarding these standards is in Chapter 3 of the thesis. The hot tensile testing procedures and methods to quantify LME cracking can also be found in Chapter 3. Research in this thesis is limited to the 3 grades of AHSS and two types of Zn coatings (QP980GI, QP980GA, DP980GI, DP980GA, QP1180GI, QP1180GA) due to interest from industry sponsors.

## 1.4 Thesis outline

The thesis is organized into the following eight chapters.

Chapter 1 introduces the background and necessity of the work, the objectives of the thesis, and constraints involved.

Chapter 2 summarizes the published literature relevant to the thesis. This includes AHSS, RSW and LME. It also points out the gap in knowledge that this thesis intends to fill

Chapter 3 explains the material, experimental procedure, and analysis methods used to fulfill the objective

Chapter 4 uses hot tensile testing to investigate the influence of various factors such as microstructure and material chemistry on the LME susceptibility of AHSS. The studied AHSS are also ranked from most LME susceptible to least.

Chapter 5 uses CCD to investigate the influence of various welding parameters on LME cracking. new weld lobes are established for each material that leads to minimal LME cracking. The welding results are used to validate the hot tensile results in Chapter 4.

Chapter 6 explores the use of aluminum interlayers to suppress LME cracking. The degree of LME suppression was quantified, and the suppression mechanism was investigated.

Chapter 7 summarizes the findings from previous chapters and identifies future work to complement this study

# Chapter 2 Literature Review

## 2.1 Advanced High Strength Steel (AHSS)

In recent years, environmental concerns have pushed automotive manufacturers to seek more fuel efficient cars in order to combat climate change [6–8]. Advanced high strength steels (AHSS) give an optimal balance of vehicle weight reduction while retaining mechanical performance, making them one of the ideal options to increase vehicle fuel efficiency.

Advanced high strength steels (AHSS) are a group of steels possessing unique microstructures that are strengthened by complex deformation and phase transformation processes. Different types of AHSS can achieve a variety of strength and ductility, as shown in Figure 2.1. The AHSS investigated in this thesis are dual phase steel (DP), quench and partitioned steel (Q&P), and transformation induced plasticity steel (TRIP), due to interest from industry. The characteristics of these steels will be discussed in the following sections.

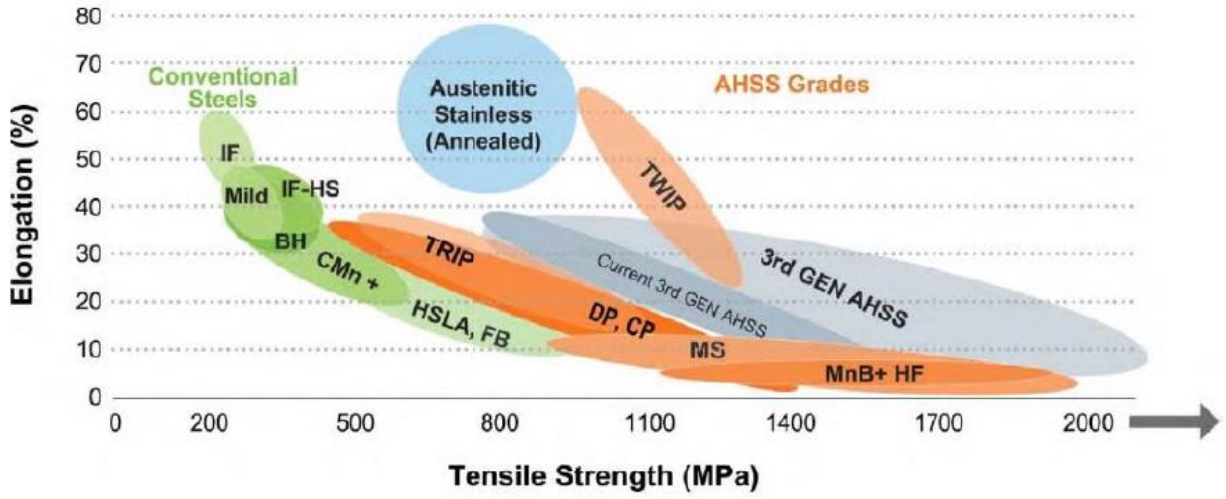


**Figure 2.1: Steel strength-ductility diagram illustrating that AHSS can possess a wide range of mechanical properties [9].**

### 2.1.1 Dual Phase (DP) Steel

DP steel consists of a ferrite matrix with 10-40% of martensite or martensite-austenite islands as shown in Figure 2.2. Ferrite contains small amounts carbon in its solid solution and it is ductile due to its body center cubic crystal structure [10]. Martensite, however, consist of a supersaturated solution of carbon in iron. The high carbon content in martensite distorts its iron crystal lattice, which makes martensite strong but brittle [10]. In DP steel, the martensite islands provides strength to the steel while the ferrite matrix

provides ductility. As shown in Figure 2.1, DP steels typically have a tensile strength between 500 – 1200 MPa while also displaying elongation superior to HSLA steels of the same strength [9,11].

DP steels are manufactured by inter-critical annealing the steel first so a portion of its microstructure is austenite at the elevated temperature. Then the steel is quenched to enable the transformation of austenite to martensite [9,11].

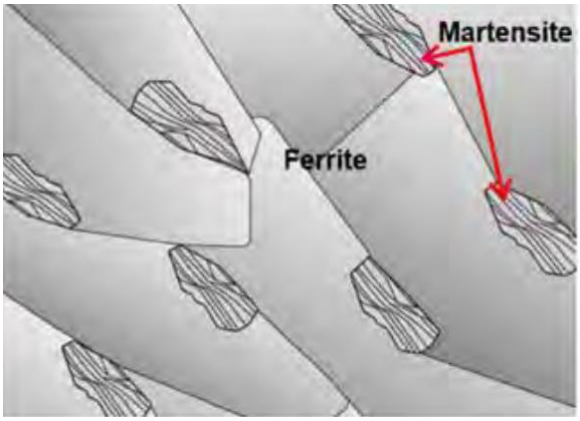


**Figure 2.2: Schematic of DP steel microstructure [9].**

### 2.1.2 Transformation Induced Plasticity (TRIP) Steel

TRIP steels consists of a ferrite matrix with martensite, bainite and a minimum of 5 vol.% retained austenite islands embedded in the ferrite matrix as shown in Figure 2.3. More carbon and alloying elements such as manganese and silicon are added to TRIP steel as compared to DP steel to stabilize its retained austenite at room temperature [10]. Similar to DP steel, the harder phases such as martensite, bainite and retained austenite gives the material strength while the softer ferrite matrix provides ductility. When strained, the retained austenite phase transforms into martensite, which improves the work-hardening and ductility of the TRIP steel [9,11,12].

TRIP steel is manufactured by first slowly cooling the steel from the austenite region to an intermediate temperature above room temperature, producing a partially ferritic microstructure. Then an isothermal hold is applied to the steel to produce bainite before it is quenched to room temperature [9,11]. Some austenite is retained after quenching due to high concentrations of carbon and manganese stabilizing the austenite while the remainder austenite is transformed to martensite [9,11,12].

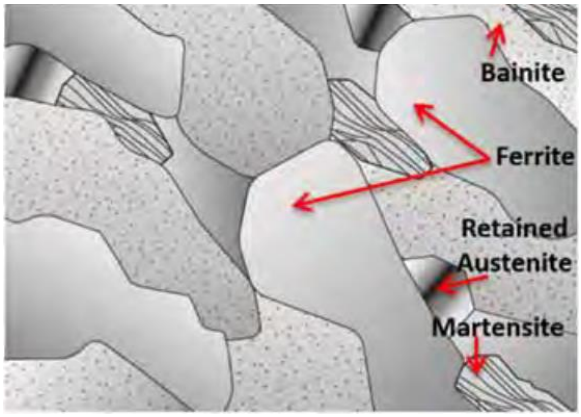


**Figure 2.3: Schematic of TRIP steel microstructure [9].**

### 2.1.3 Quench and Partitioned (Q&P) Steel

Q&P steel mainly consists of a ferrite matrix with tempered martensite and retained austenite islands embedded in the ferrite matrix as shown in Figure 2.4. Q&P steel has similar chemical composition as conventional TRIP steel where more carbon and additional alloying elements added to stabilize its retained austenite at room temperature [13,14]. The harder phases in Q&P steels such as tempered martensite and retained austenite gives the material strength while the softer ferrite matrix provides ductility. Similar to TRIP steel, the retained austenite phase transforms into martensite when strained, which improves the work-hardening and ductility of the Q&P steel [12]. However, Q&P steel can attain higher strength levels than TRIP steels due to its higher martensite content and the heat treatment process [13,14].

Q&P steel is manufactured by first quenching the steel from the austenite region to below the martensite-start temperature, but above the martensite-finish temperature. This process forms a controlled volume fraction of martensite [13,14]. Then during the partitioning step, the quenched steel is held at a higher temperature than the quench temperature. In this step, the carbon partitioning from martensite into the austenite stabilizes the austenite at room temperature [13,14].

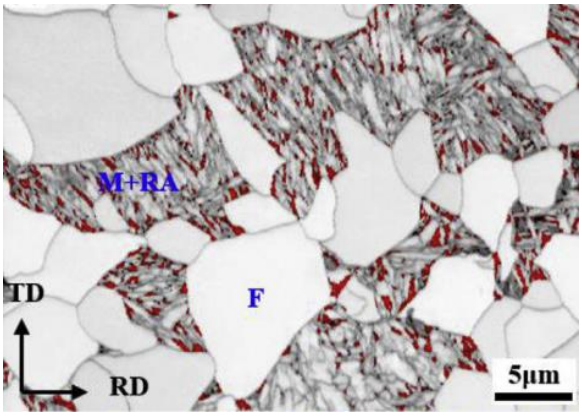


**Figure 2.4: Schematic of Q&P steel microstructure [14].**

## 2.2 Hot-Dip Galvanizing

AHSS are usually Zn coated to protect the steel against corrosion. When the Zn coating is undamaged, it grants barrier protection where the coating physically separates the steel from the corrosive environment. When the Zn coating is damaged and some parts of the steel is exposed, the Zn grants galvanic protection where Zn acts as the anode and sacrificially corrodes in place of the steel.

In this study, the Zn coating have been applied onto the steels via the hot dip galvanization process. During hot-dip galvanization, the steel sheet is first pre-heated to the temperature of the zinc bath to facilitate adhesion of Zn. Then, the steel sheet is passed through the molten zinc bath where the zinc adheres to the steel sheet, hence "hot-dip". Finally, the excess zinc is removed using air knives to obtain the desired coating thickness [9][15]. Typically, the Zn bath contains 0.005 – 0.02 wt.% of aluminum to improve the appearance of the coating [15]. This type of coating is referred to as hot-dip galvanized (GI) coating.

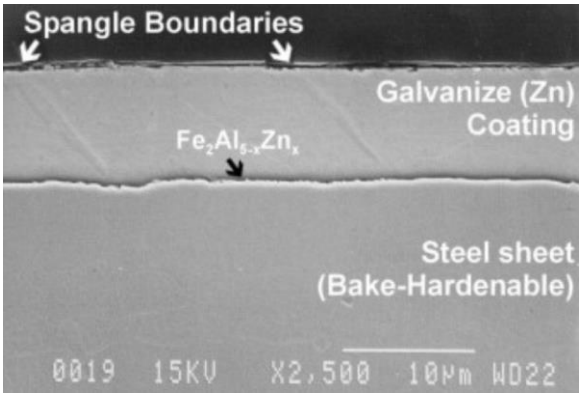


**Figure 2.5: Cross-sectional view of hot-dip galvanized coating on steel [16].**

The Zn coating can go through an additional annealing process after hot-dip galvanizing to produce galvannealed (GA) coating. Right after the hot-dip process, the Zn coating is annealed at a temperature between 450 – 600°C [15] to promote diffusion between the Zn coating and the steel substrate. The final galvannealed coating contains 8 – 12 wt.% Fe in the form of Γ, δ, and ζ intermetallic phases as shown in Figure 2.6. The GA coating is weaker in terms of galvanic protection than GI coating but it is sometimes preferred over GI coating due to its superior paintability and weldability.

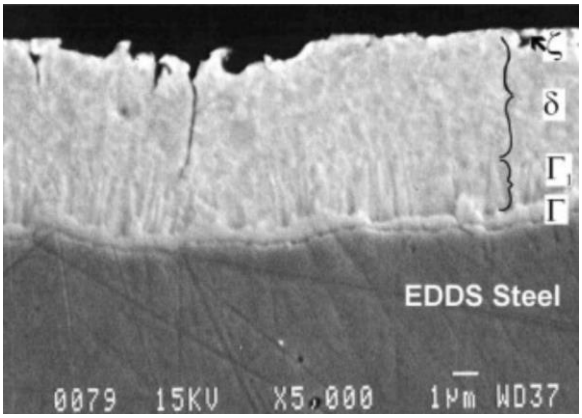


**Figure 2.6: Cross-section of galvannealed coating etched to show the Γ phase at the steel interface, along with δ and ζ phases [16].**

## 2.3 Resistance Spot Welding (RSW)

RSW Resistance spot welding (RSW) is a fusion welding process where the work piece is melted by a high electric current passing between the electrodes and through the work piece [17–19]. RSW is low cost, low cycle time and easy to operate, making it the most popular welding process in the automotive industry. On average, 3000 – 6000 spot welds are required to assemble a vehicle [20,21].

### 2.3.1 RSW Fundamentals

The RSW process consists of five stages in sequence: clamp, squeeze, heat, hold, and release, as shown in Figure 2.7.

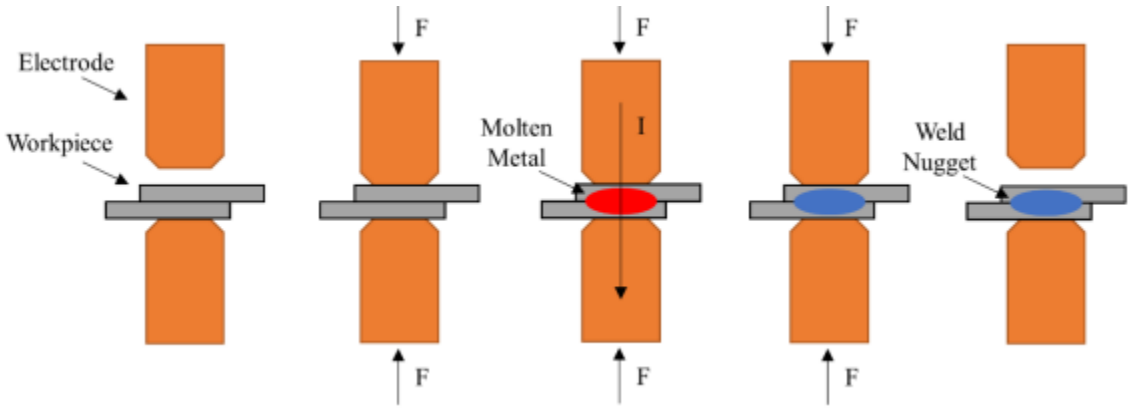


**Figure 2.7: Steps in making a resistance spot weld [22].**

In the first stage, the work piece is clamped between the electrodes to secure them in place. In the second stage, a squeezing force is applied between the electrodes to minimize the air gaps and asperities. In the third stage, an electric current is applied for an amount of time, melting the sheet to sheet interface and forming a "weld nugget". In the fourth stage, the current is turned off while the work piece remains to be held between the electrodes. This allows the molten metal to solidify. The amount of time the work piece is being held is known as the hold time. In the final stage, the electrodes are released. Resistance spot welds are completed so fast that the time required to complete a single weld is only on the scale of hundreds of milliseconds.

The heat generation via electric current is based on joule heating, as shown in Eqs. (2.1). Q is the amount of heat generated, I is the current, R is the resistance across the electrodes, and t is the duration of the applied current [17].

$$Q = I^2Rt \tag{2.1}$$

The resistance across the electrodes consists of five individual resistances that are in series as shown in Figure 2.8. The five resistances can be categorized into either bulk resistances or interfacial resistances. R2 and R4 in Figure 2.8 are bulk resistances of the work pieces. As for interfacial resistances, R1 and R5 are the interfacial resistances between the electrodes and work pieces and R3 is the interfacial resistance between the two work pieces. The interfacial resistance R3 is generally the highest of the five resistances. As a result, the majority of the heat generated during RSW is concentrated between the work pieces, forming a weld nugget [23]. Because the resistances are in series, they can be summed up to the total resistance R in Eqs. (2.1).

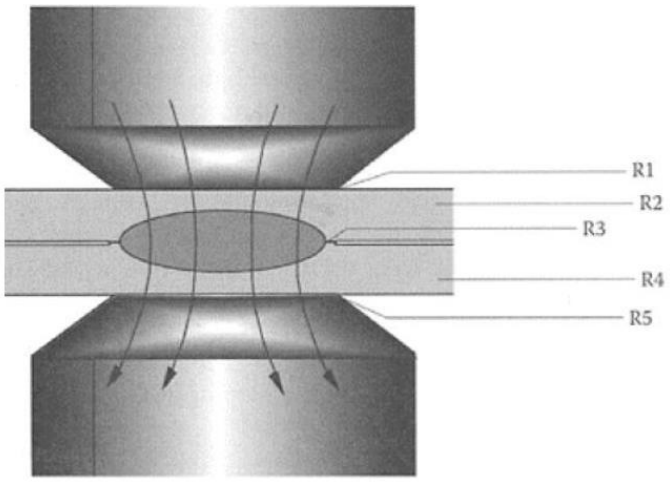


**Figure 2.8: Breakdown of electrical resistances during RSW [24].**

The interfacial resistance R3 is dependent on the surface condition of the steel. In RSW of GI coated steel, the GI coating reduces R3 due to melting of the GI coating. As a result, around 10% more welding current or weld time is required to weld GI coated steel than its bare counterpart [17]. On the other hand, the GA coating is more resistive than GI coating due to its Fe content, making the effect of GA coating on the weldability of the steel less pronounced.

The resistance R also does not remain constant during the welding process. A schematic of the resistance R over the period of a weld is shown in Figure 2.9. As the weld progresses, a series of reactions such as elimination of the oxide layer, softening of the asperities, and melting of the work piece take place, which changes the resistance R [25,26].

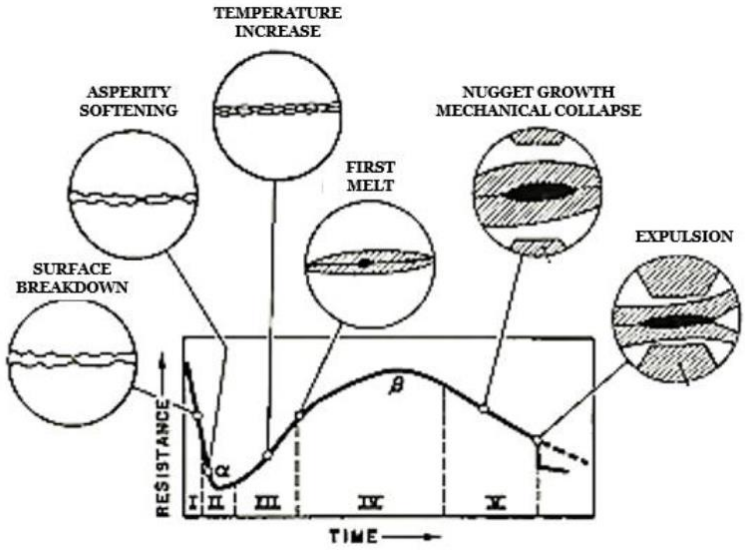


**Figure 2.9: Generalized dynamic resistance curve correlated with events during RSW process [25].**

### 2.3.2 Welding Parameters

The RSW process involves many parameters such as weld current, weld time, electrode force, hold time, etc. These parameters control the nugget diameter of the resultant weld. If they are not set up correctly, they can also create weld defects. The most important parameters are weld current, weld time, and electrode force, as they have a direct effect on the nugget size [18,21].

The weld current and weld time are the most intuitive to understand. When the other parameters are held constant, the heat input increases as either the weld current or weld time increases (Eqs. (2.1)), which results in a larger nugget diameter. The heat input is a function of the current squared, meaning current has a larger impact to the process compared to weld time.

The weld force effectively changes the resistance between the electrodes. All materials' surfaces are uneven and materials that appear to be in contact with each other are in fact only touching at the tips of their asperities. A higher electrode force pushes the work pieces closer together, creating more contact area between the two work pieces. More contact area decreases the interfacial resistance, which results in less heat input and a smaller nugget diameter [18,19,21]. The weld force also helps to contain the molten nugget between the electrodes during heating. If the weld force is not high enough, the molten nugget could eject liquid metal out from the sheet to sheet interface. This phenomenon is known as "expulsion" [18,19,21].

### 2.3.3 Weld Lobe

The nugget diameter is the major factor that determines the strength and fracture mode of a resistance spot weld [18,27]. As a result, only a certain range of nugget diameter is acceptable for engineering applications. The AWS D8.9, a standard for RSW that is widely accepted around the world [5], defines the minimum weld diameter to be

$$Minimum\ Weld\ Size = 4\sqrt{t} \tag{2.2}$$

where t is the thickness of a single work piece. Undersized welds are undesirable because it reduces the strength of the weld. However, the nugget diameter cannot be excessively large either. If the heat input is too high, the nugget could outgrow the area being squeezed by the electrode and create expulsion. Expulsion is undesirable because it could cause defects in the weld nugget and reduce the strength of the weld [28,29].

A weld lobe, such as the one in Figure 2.10, shows the range of weld current and weld time that can create acceptable weld nuggets. The welding current and time are varied while the other parameters such as weld force and hold time are kept constant. The left side of the lobe is defined by the minimum nugget size whereas the right size is defined by the occurrence of expulsion. Welds done inside the weld lobe is typically free of defect and of sufficient nugget size. The location and width of the weld lobe is heavily dependent on the characteristic of the work piece such as surface conditions, material chemistry, sheet thickness, etc [30]. It is generally accepted that a wider and larger weld lobe is better as it indicates that a wider range of parameters can be used to make an acceptable weld, making the process more tolerant to variations in a manufacturing environment [30].

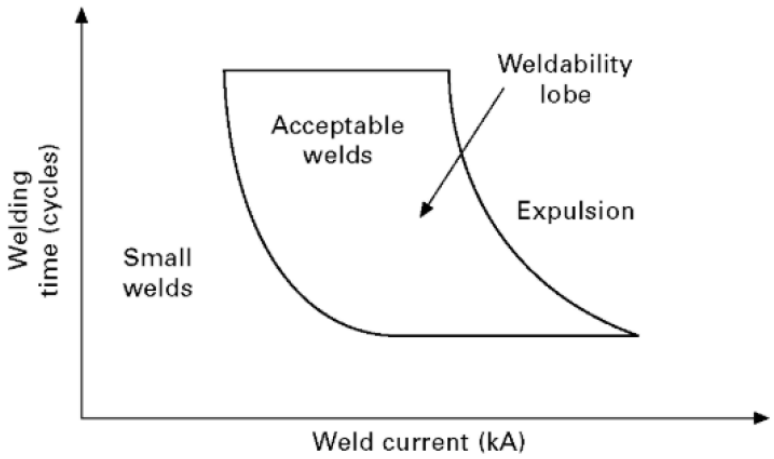


**Figure 2.10: Weld lobe of RSW [30].**

### 2.3.4 Pulsed Welding Schedules

A welding schedule without pulsing is shown in figure 1. It entails a constant current passing through the electrodes for a set amount of time. It is the most commonly used type of welding schedule. In a way, it can also be viewed as a single pulse welding schedule.

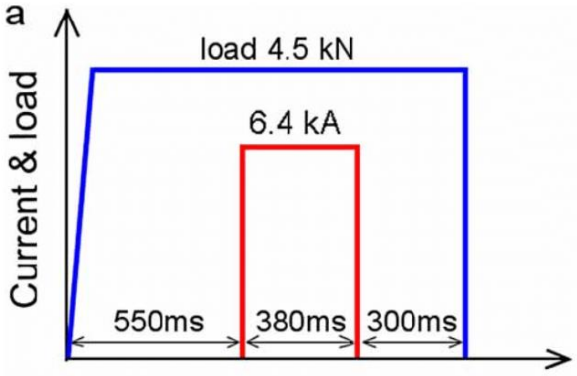


**Figure 2.11: Illustration of a RSW schedule without pulsing [31].**

The pulsed welding schedule used in this study utilizes pulsing during the welding cycle. A pulsed welding schedule, as shown in Figure 2.12, divides the main welding current into two separate pulses. When designing a pulsed welding schedule, there is no limit as to the number of pluses, the current for individual pulses and the cooling time between pulses. However, pulsed welding schedules in general require longer time to complete than welding schedules without pulsing. This reduces the overall productivity of the pulsed welding schedules. On the other hand, pulsing slows down nugget growth and delays expulsion, which widens the weld lobe [32,33]. This is heavily desired when welding AHSS as AHSS in general have

narrower weld lobes than mild and high strength steels [34]. In fact, pulsed welding schedules are recommended in RSW standards such as AWS D8.9 and the A/SP standard for welding AHSS sheets thicker than 1.3mm [4,35]

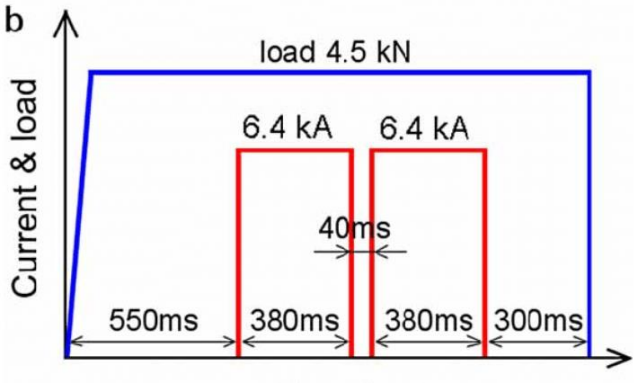


**Figure 2.12: Illustration a RSW schedule with two pulses [31].**

## 2.4 Liquid Metal Embrittlement in the Fe-Zn System

Liquid metal embrittlement refers to the phenomenon where a usually ductile metal experiences brittle fracture when stressed in the presence of a specific liquid metal [36]. There are multiple solid/liquid metal pairs that cause LME. $Cu_{solid}/Bi_{liquid}$, $Al_{solid}/Ga_{liquid}$, and $Fe_{solid}/Zn_{liquid}$ are some of the notable pairs. [2,37–41]. However, only the $Fe_{solid}/Zn_{liquid}$ pair will be discussed in this study and all mentions of LME only refer to the $Fe_{solid/}Zn_{liquid}$ pair.

The LME severity of zinc coated steels is usually evaluated by tensile testing while the steel specimens are in contact with liquid zinc. The fracture surfaces are also examined post fracture. Tensile test results reveal that LME can be characterized by the severe reduction in the materials ductility and strength at fracture [39,42]. Figure 2.13 presents the tensile curves of a TWIP steel embrittled by liquid Zn. The large reduction in the elongation to fracture of the Electro-galvanized specimen as compared to the bare specimen is characteristic of the LME phenomenon. Figure 2.13 also shows that the steels mechanical properties such as Young's Modulus, work hardening coefficient and yield strength is unchanged by LME prior to premature fracture, which is another characteristic of the LME phenomenon[39,42,43].

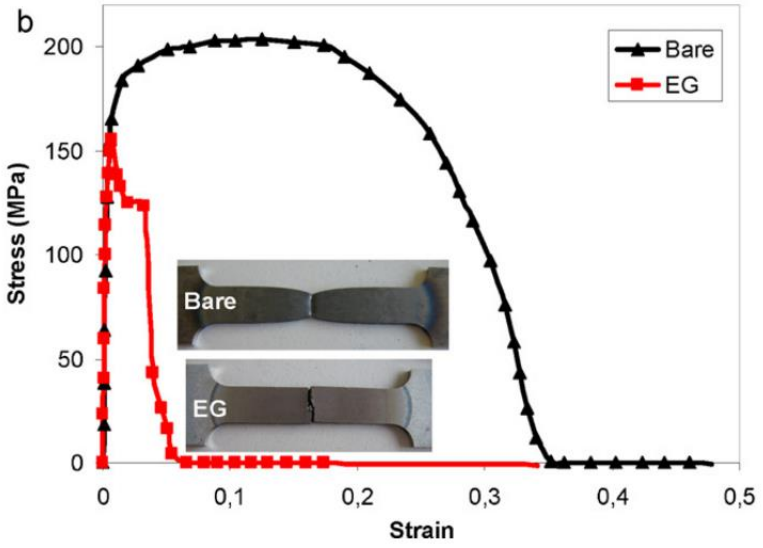


**Figure 2.13: Tensile Curve of a TWIP steel embrittled by liquid Zn *[2]*.**

The LME mechanism attacks the grain boundaries of steel and has a high crack propagation rate, which results in brittle, intergranular fracture at the fracture interface [44–46]. Observations in the transverse plane of a LME crack in TWIP steel as shown in Figure 2.14 clearly depicts the crack to run along the steel grain boundaries.

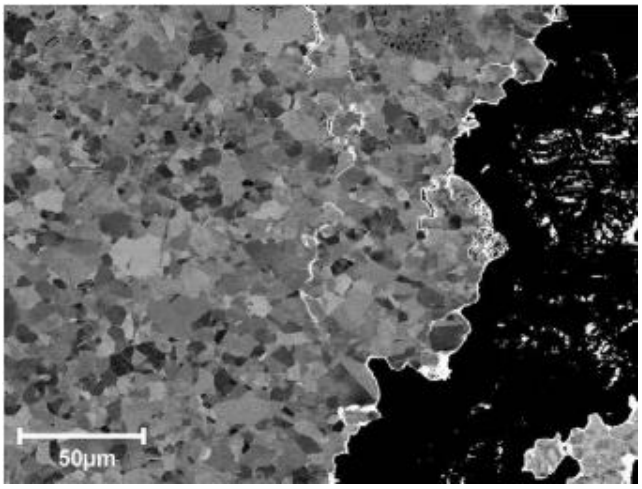


**Figure 2.14: LME crack of a TWIP steel embrittled by liquid Zn *[2]*.**

For LME to occur, three conditions must be met simultaneously: the steel type must be susceptible to LME, there must be contact between the steel and liquid zinc, and sufficient tensile stress must be present [36]. A possible scenario of LME and the resultant cracking is shown in Figure 2.15. First, the liquid zinc penetrates the grain boundaries either by diffusion or by percolation, weakening the grain boundaries (Figure 2.15(a)) [45]. In the presence of tensile stresses, these cracks are opened up and is filled in with

liquid zinc (Figure 2.15(b)). This allows zinc to penetrate further into the grain boundaries and propagate the crack (Figure 2.15(c)). There are a number of factors that influence the occurrence of LME, and they will be discussed in the following sections.

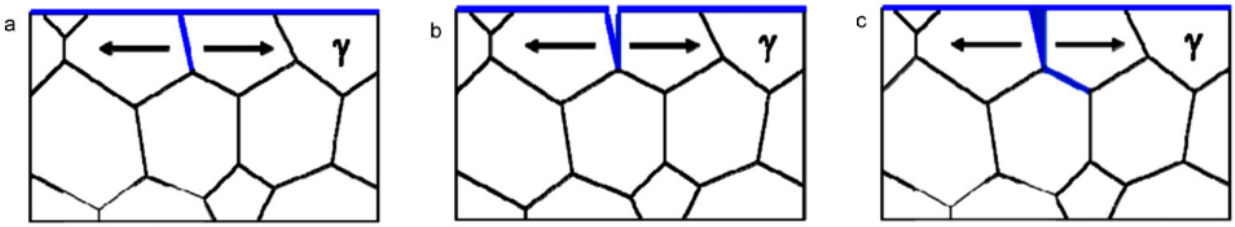


**Figure 2.15: Possible scenario of LME and crack propagation [2].**

### 2.4.1 Effect of Temperature

LME is a temperature dependent phenomenon and a critical temperature range exists in which the ductility of the steel is greatly reduced by LME. This critical temperature range is known as the "ductility trough" [36]. Since a reduction in ductility directly translates to a reduction in fracture energy, the ductility trough can be alternatively plotted as a function of the reduction of fracture energy with respect to temperature [46]. Figure 2.16 shows the ductility trough for a TWIP steel defined by the relative reduction of fraction energy due to premature fracture caused by LME. The ductility trough of this TWIP steel start at 700°C and end at 950°C.

It is generally recognized in literature that the ductility trough ends at 950°C because it is above the boiling temperature of liquid Zn (906°C) and a lack of liquid Zn stops LME. The same rule applies to other solid/liquid metal systems where their ductility troughs end at the boiling temperatures of the embrittling liquids.

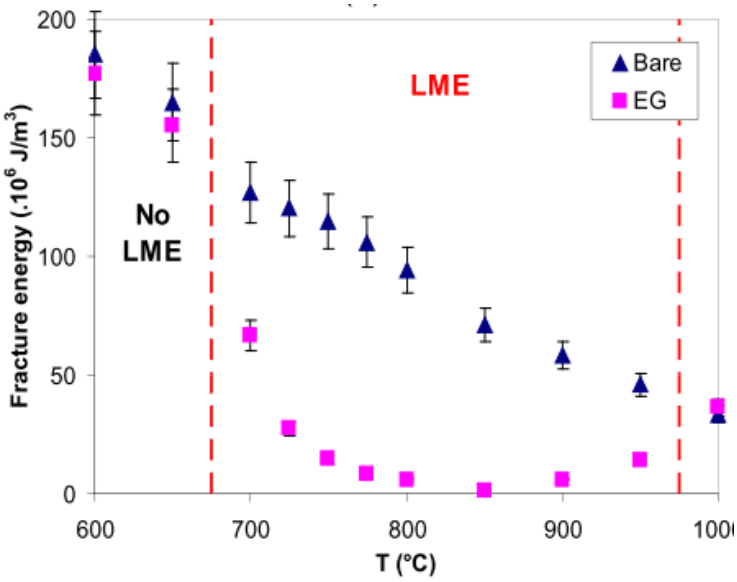


**Figure 2.16: Ductility trough of a TWIP steel [46].**

The starting temperature of the ductility trough in the Fe-Zn system, however, is different from other solid/liquid metal systems. The ductility trough for other solid/liquid metal systems start at the melting temperature of the embrittling liquid [2,37–41] while the ductility trough of the TWIP steel in Figure 2.16 start approximately 200°C above the melting point of the liquid Zn. In fact, a number of LME susceptible steels only start to be embrittled above 700°C [2,36,45,47,48].

Several explanations have been provided for this behaviour. In Figure 2.17, Beal observed that at temperatures below 700°C, the critical stress required to initiate LME cracking is higher than the UTS of the steel. This results in plastic deformation occurring before LME cracks begin to form [2,49].

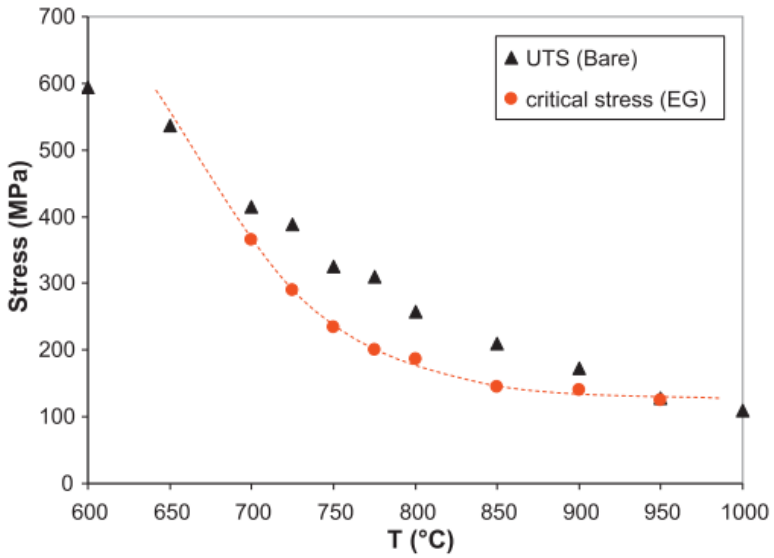


**Figure 2.17: Evolution of the critical stress and UTS with temperature [2].**

Kang observed the formation of solid Fe-Zn intermetallic compounds as the Zn-coated steel is heated during hot tensile testing [45]. He commented that the Fe-Zn intermetallic could act as a barrier that separates the liquid zinc from the steel substrate. As shown in the Fe-Zn binary phase diagram in Figure 2.18, between 672°C and the peritectic isotherm at 782°C, the $\Gamma_1$ phase could have been dissolved enough for liquid zinc to have sufficient contact with the steel substrate to cause LME. The explanations provided by Beal and Kang are both good reasons as to why LME in the Fe-Zn systems is observed at temperatures far above the melting point of Zn.

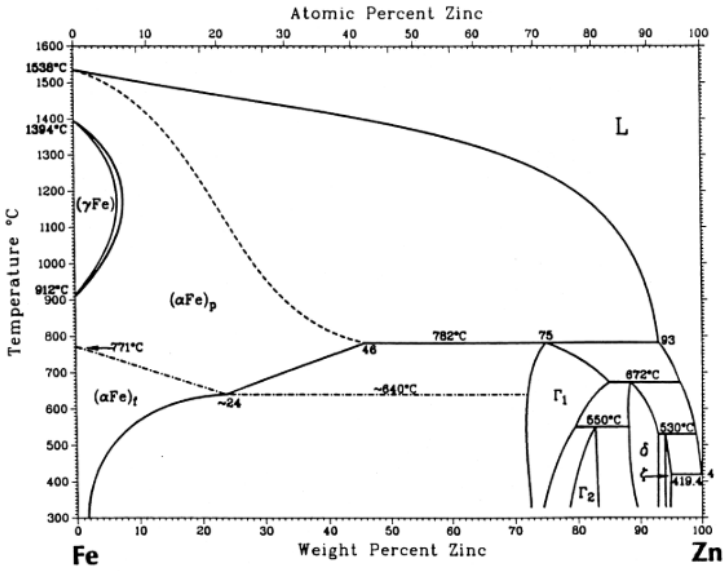


**Figure 2.18: Fe-Zn binary phase diagram [15].**

### 2.4.2 Effect of Material Strength

The strength of the steel influences its susceptibility to LME. The ductility trough of higher strength steels have been observed to be wider than lower strength steels [46]. Embrittled steels with higher strengths have also been observed to have a higher LME crack density and deeper crack penetrations than lower strength steels [50].

In terms of stress, the crack tip of higher strength steels is subjected to a higher stress state as compared to lower strength steels [45]. This higher stress state makes it more probable for steels with higher strength to reach their critical stress required to initiate LME as compared to lower strength steels [46]. The LME crack propagation mechanism, which relies on the solid state diffusion and percolation of liquid zinc, is also enhanced in high stress conditions [45].

### 2.4.3 Effect of Steel Microstructure

It is commonly recognized that TWIP and TRIP steels are more susceptible to LME compared to other types of steels [33,47,50–54]. As seen in Figure 2.19, the TWIP and TRIP steels experienced reduction of fracture energy due to LME at a lower temperature than the DP steel, with the TWIP steel experiencing reduction of fracture energy at an even lower temperature than the TRIP steel. Since TWIP and TRIP steels have higher austenite content in their microstructure compared to other steel types, it is generally assumed that LME sensitivity is related to the presence of austenite [55]. Spot welding experiments also show areas that have been transformed to austenite during the spot welding process have more surface cracks compared to areas surrounding the welds that have not been transformed to austenite [56].

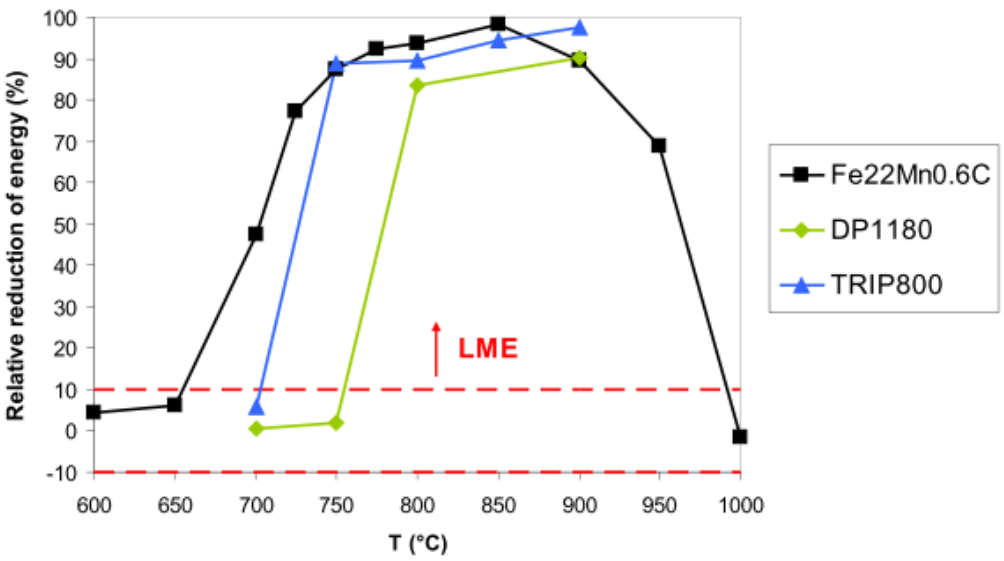


**Figure 2.19: Severity of embrittlement of different steels [46].**

There are two proposed mechanisms for austenite susceptibility to LME. The first is based on stress associated with thermal expansion and phase transformation [47]. The second is based on ease of Zn transportation between the austenite grain boundaries [45].

Thermal contraction/expansion in the constrained steel causes stress, which influences LME susceptibility of the steel. As shown in Figure 2.20, the thermal expansion of the TWIP steel is twice as high as that of the DP steel, which is attributed to the large difference in austenite fraction of their respective microstructures [55,57]. The higher thermal expansion of the TWIP steel puts the steel in a higher stress state, which makes it easier for the TWIP steel to exceed the critical stress required for LME to occur.

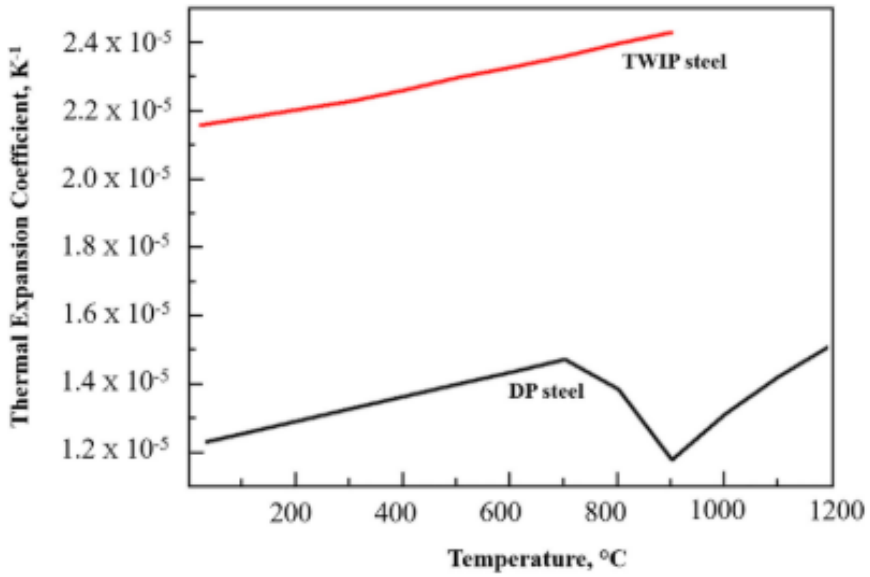


**Figure 2.20: Thermal expansion coefficient of DP and TWIP steels determined from dilatometry [45].**

Kang noticed the presence of Zn-enriched austenite ahead of the LME crack tip. This observation suggests that Zn grain boundary diffusion and liquid Zn percolation along austenite grain boundaries is the embrittling mechanism [45]. The liquid zinc favors austenite grain boundaries as the zinc diffusivity in the austenite grain boundary is higher than that in ferrite [42]. This makes steels such as TWIP and TRIP steels that have a higher austenite content easy to be embrittled by liquid Zn.

### 2.4.4 Effect of Coating Type

Although the type of Zn coating greatly influences the LME susceptibility of the steel, there are only a handful of dedicated research conducted on the subject. Only the GI and GA coatings will be discussed in this section since the steels in this study were only coated with these two types of coatings.

All studies suggest that GI coated steels are far more susceptible to LME compared to their GA coated counterparts. RSW results in Figure 2.21 show that the GI coated steel have the greatest reduction in weldable current range due to LME cracks. It has also been observed that GI coated steels have longer LME cracks compared to their GA coated counterparts [33,58].

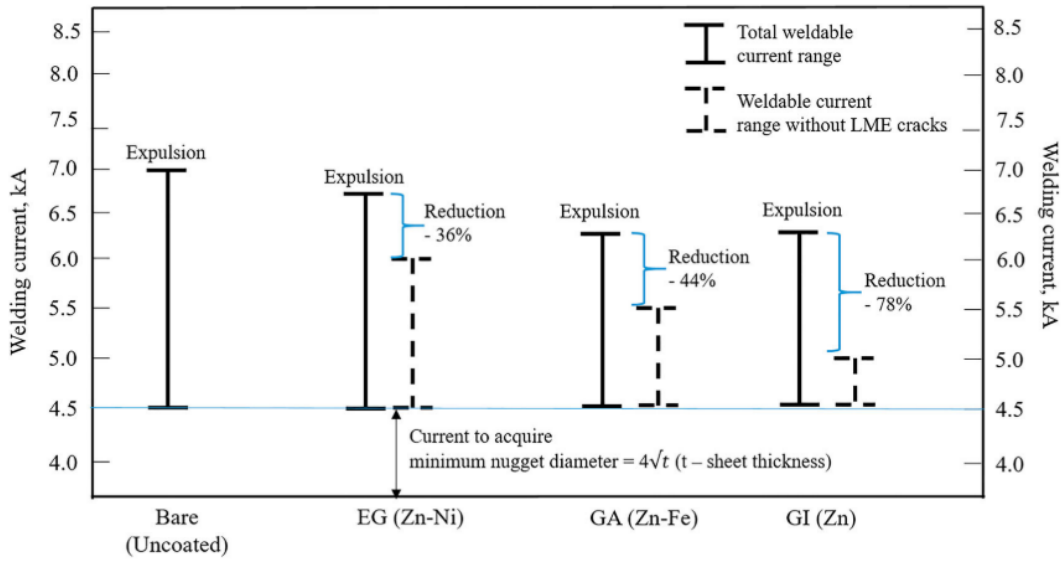


**Figure 2.21: Effect of LME on the weldable current range of TWIP steels with different Zn coatings [33,55,58].**

It is generally recognised that LME is reduced if there is intermetallic compound between the solid metal and the embrittling liquid [45,55]. The GA coatings contain 10 wt.% Fe on average in the form of various Fe-Zn intermetallic between the steel substrate and the Zn coating as shown in Figure 2.6. According to the Fe-Zn phase diagram in Figure 2.18, the $\Gamma_1$ phase has the highest melting point amongst the various Fe-Zn intermetallic and it only begins to dissolve above 672°C. Below this temperature, the layer of $\Gamma_1$ intermetallic physically separates the steel from liquid zinc, which reduces the risk of LME in GA coated steels [33,55,58].

Aluminum build up may also play a minor role in higher LME susceptibility of GI coated steels. Tolf noticed aluminum buildup on the electrode from welding GI coated steels whereas no aluminum was detected on the electrodes used to weld GA coated steels [52][55]. When welding GI coated steels, the buildup of aluminum oxide increases the electrical resistance, which in turn increases the surface temperature of the spot weld. A higher surface temperature increases the probability for LME to occur [52][55].

## 2.5 LME in RSW of AHSS

LME is a concern when spot welding Zn-coated susceptible steels. LME cracks as shown in Figure 2.22 is commonly observed in embrittled welds. The LME cracks are identified by their intergranular path and Zn being detected inside the cracks [33,54,58–61].

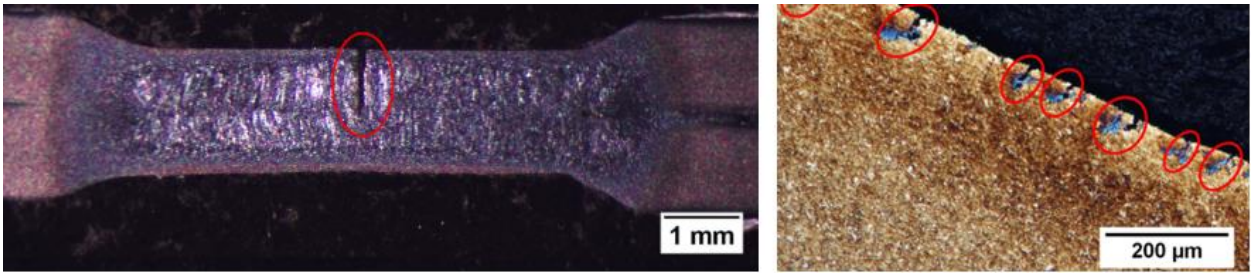


**Figure 2.22: Micrographs of resistance spot welds of a TRIP steel with LME cracks circled [62].**

As explained in Section 2.4, three conditions must be met simultaneously for LME to occur: susceptible microstructure, contact between steel and liquid zinc, and sufficient stress. During RSW of Zn coated steels, the zinc coating on the steel surface melts from the heat generated at the sheet to sheet interface, providing liquid Zn. Weld deformation, non-uniform heat transfer at specific regions, and thermal contraction during the cooling stage generates tensile stresses [55]. Both of the above factors paired with a susceptible material leads to LME cracks as shown in Figure 2.22.

### 2.5.1 Effect of Welding Parameters on LME

As discussed in Section 2.3.2, a number of factors can be adjusted in resistance spot welding. Weld current, weld time and electrode force have a direct effect on the heat input, which in turn controls the nugget diameter of the weld.

Several studies have been conducted to gauge the impact of these welding parameters on LME cracking in the spot weld[33,58,60]. In general, it is observed that a larger heat input leads to a higher LME cracking severity. This is because a high enough heat input results in a fast rate of nugget growth and thermal expansion that leads to high stress at LME susceptible locations of the weld [22]. Furthermore, its also been observed that LME cracking could only occur when the nugget exceeds a certain size [33,58].

In terms of specific weld parameters, several scholars have observed LME cracks only at high welding currents [33,56,63]. Choi demonstrated that a longer weld time not only increased heat input, but lengthened the amount of time Zn remained liquid, which increased LME severity [54]. A reduction in electrode forces decreases the contact area between the electrode and steel sheet. This increases the heat input and decreases the cooling efficiency, which leads to an increase in LME crack severity [60].

Even though hold time does not directly affect the heat input, it controls the temperature and stress state of the steel during the cooling process, which also affects the creation of LME cracks. As shown in Figure 2.23, the stress state changes from compressive to tensile when the electrodes are released. A longer

hold time gives more time for the weld nugget and surrounding area to cool, which allows the Zn to solidify and creates less tensile stress at electrode release [56,60].

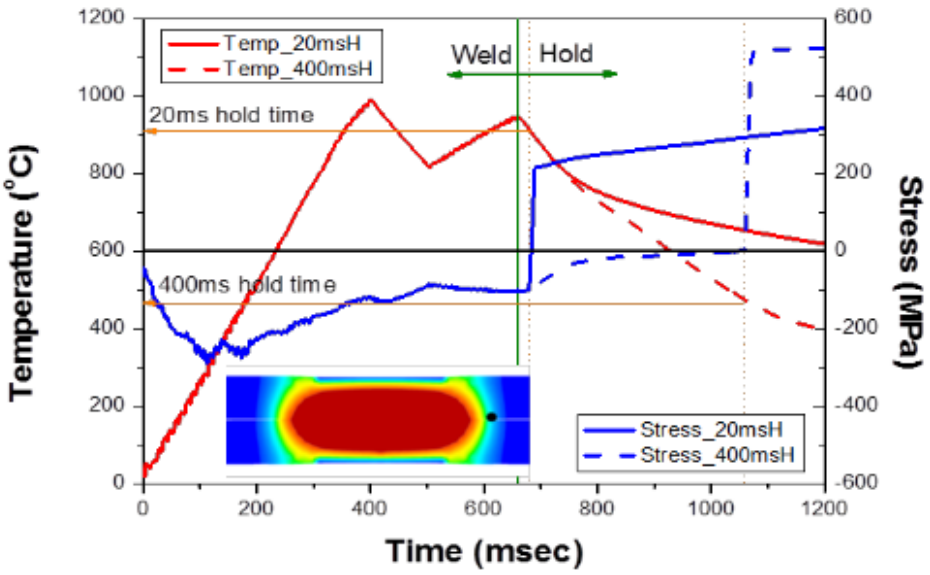


**Figure 2.23: Calculated temperature and stress profiles at Type C cracking position [60].**

### 2.5.2 Quantifying LME Severity

In the past, there wasn't any standard methods to quantify LME cracking severity in resistance spot welds. Some scholars quantified LME cracks via surface examination by recording the total length of surface cracks [52], the total crack surface area [61], and the surface cracking ratio [51]. Other scholars quantified LME cracks from the weld cross-section by recording the maximum crack length [33,54,58,64], number of LME cracks per weld [53], and mean crack length [53]. The above mentioned methods all failed to fully quantify LME cracks. This is clearly shown in Figure 2.24 where the material rankings of their LME crack severity changes depending on the quantification method used.

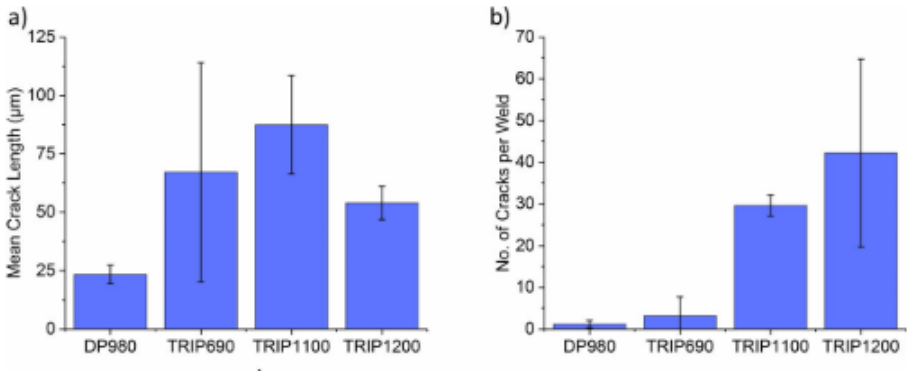


**Figure 2.24: a. Mean crack length, b. Average number of cracks per weld in samples of AHSS. Error bars represent 95% confidence interval [62].**

A recent discovery have taken a statistical approach to describe LME cracks. Wintjes et al showed that the population of LME cracks observed at the weld cross-section follow a log-normal distribution. She proposed a term called the "crack index" to describe this distribution with great accuracy. The crack index is calculated by:

$$Crack\ Index = \frac{n\mathrm{L}}{t} \tag{2.3}$$

where n is the number of cracks per weld, L is the lognormal median crack length, and t is the sheet thickness. Following the invention of the crack index, this method has been used to relate LME cracks to other influence factors with great success [65][66]. In this study, the crack index will be used to quantify LME cracks observed in resistance spot welds.

### 2.5.3 Effect of LME on Lap Shear Strength

LME cracks in resistance spot welds have been shown to negatively affect the lap shear strength of spot welds. Choi *et al*. noticed a loss in lap shear strength in GI coated TRIP1180 only when LME cracks were longer than 325 μm [54]. A study by DiGiovanni *et al*. concluded that crack location was also a significant factor in determining if LME cracks would have an impact on lap shear strength. The weld is not uniformly load during tensile lap shear testing and only cracks located in highly stressed areas were shown to reduce the weld strength [66,67]. From the research results of Choi and DiGiovanni, it seems that LME cracks must be located at certain critical regions on the spot weld and be above a minimum length to affect the lap shear strength [64].

Wintjes *et al*. discovered that welds experienced more strength loss with increasing crack index as shown in Figure 2.25. Her discovery is in line with the observations by Choi and DiGiovanni. An increase

in the crack index indicates that the LME cracks are both longer and more in number. This means that there is a higher chance that LME cracks of sufficient size will land at critical regions that will affect the lap shear strength of the weld.

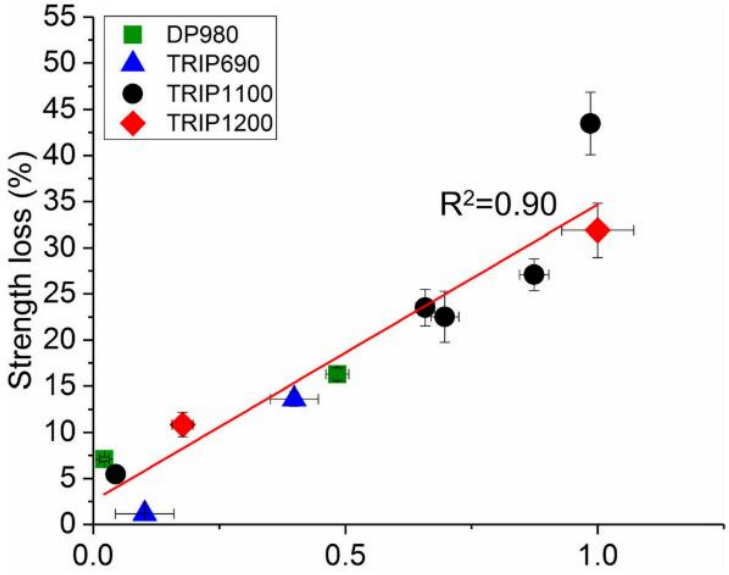


**Figure 2.25: Relationship between crack index and strength loss for AHSS[62]**

### 2.5.4 Methods for LME reduction in RSW

As discussed in section 2.5.1, the welding parameters have a large impact on the LME severity during RSW. However, LME can be reduced by selecting welding parameters that are not favourable for it to occur. This entails lengthening hold time, reducing the heat input by lowering the weld current and/or time, and increasing the electrode force [33,54,56,58,60,63].

Several alternative welding schedules have also been proposed to reduce LME. Ashiri discovered a two-pulse impulse welding schedule designed to manage the heat input better [33,58]. Kim and Wintjes both used a pre-pulse to eliminate the liquid zinc prior to the main welding current [51,65]. From the hardware side, various scholars discovered that using electrodes with a large radius is also effective at reducing LME cracks in the steel [53,56,66,68].

However, none of the mentioned methods was capable of eliminating LME cracking in highly susceptible GI coated TRIP or TWIP steels that have an ultimate tensile strength above 1GPa. Furthermore, there has been no study involving resistance spot welding that tried to remove the zinc through a chemical reaction as was done by Li et al., who used aluminium shims to

eliminate zinc vapour pores in laser lap welds in GI coated steels [69]. More work needs to be done to explore novel methods that can reduce LME in highly susceptible steels during RSW.

# Chapter 3 Methodology

## 3.1 Materials

Five grades of AHSS and two Zn based coatings were investigated in this research. Testing was designed to understand the effect of coating type (GI/GA) and material family (DP/QP) on LME in addition to ways of suppressing LME in highly susceptible TRIP steels. All of the materials were produced in an industrial environment and zinc coated using hot-dip galvanization. The chemical compositions of all materials used can be found in Table 3.1. The carbon equivalent (CE) is evaluated with the Yurioka formula [70].

**Table 3.1: Composition and coating thickness of provided materials**

| Steel Grade | Sheet Thickness (mm) | Zinc Coating Thickness (um) | Composition (wt %) | | | |
|---|---|---|---|---|---|---|
| | | | C | Si | Mn | CE |
| QP980GI | 1.4 | 12.1 | 0.18 | 1.77 | 2.25 | 0.37 |
| QP980GA | 1.6 | 6.9 | 0.18 | 1.76 | 1.78 | 0.35 |
| DP980GI | 1.5 | 9.7 | 0.09 | 0.45 | 2.14 | 0.22 |
| DP980GA | 1.4 | 6.5 | 0.09 | 0.45 | 2.69 | 0.26 |
| QP1180GI | 1.6 | 9.0 | 0.18 | 1.67 | 2.63 | 0.39 |
| QP1180GA | 1.6 | 6.7 | 0.18 | 1.67 | 2.61 | 0.39 |
| TRIP 1100 | 1.6 | 10.0 | 0.20 | 1.60 | 2.17 | 0.36 |
| TRIP 1200 | 1.6 | 10.0 | 0.20 | 1.70 | 2.30 | 0.37 |

## 3.2 Hot Tensile Testing

### 3.2.1 Principle

High-temperature uniaxial tensile tests were carried out using a Gleeble 3500 thermomechanical simulator. The tensile samples were held in place by Cu grips as shown in Figure 3.1. An electrical current was passed through the tensile sample and the sample was heated up through joule heating. Temperature of the tensile sample was controlled based on feedback from a K type thermocouple welded at the centre of the sample while tensile testing was controlled by the displacement of the grips. During the hot tensile testing, force, stroke displacement, and temperature was automatically recorded using a 1ms sample frequency. All tests were performed under regular atmosphere.

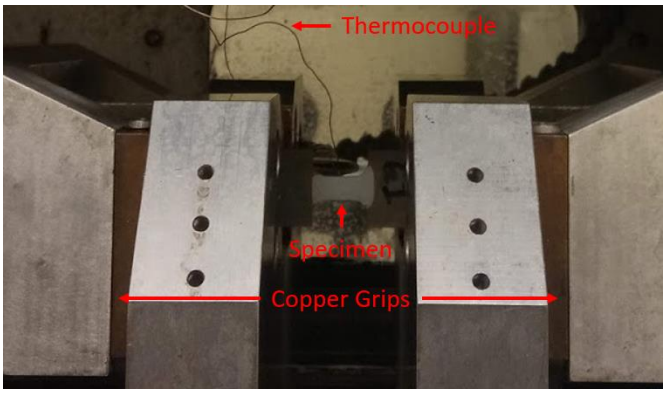


**Figure 3.1: specimen set up in Gleeble 3500 simulator**

### 3.2.2 Specimen

Hot tensile testing specimens were prepared in a dog bone shape. Bare and Zn coated specimens were both used in this study. The bare specimens were expected to exhibit no LME whereas the Zn coated specimens were expected to fracture prematurely due to LME. The tensile curves of Zn coated specimens would be compared with bare specimens to quantify the severity of LME.

For the bare specimens, the Zn coating was completely stripped off. For the Zn coated specimens, the Zn coating was stripped off all of the surfaces except for the gauge area on the side where the thermocouple was not welded on. Partially stripping Zn off Zn coated specimens prevents Zn sticking to the Cu grips when the specimens are heated. It also prevents the interaction between the Zn and the thermocouple resulting in increased LME susceptibility [46].

The methodology used to prepare the specimens is as follows. All hot tensile specimens were waterjet cut and oriented so the tensile direction is perpendicular to the rolling direction. The dimensions of the hot tensile specimens are illustrated in Figure 3.2.

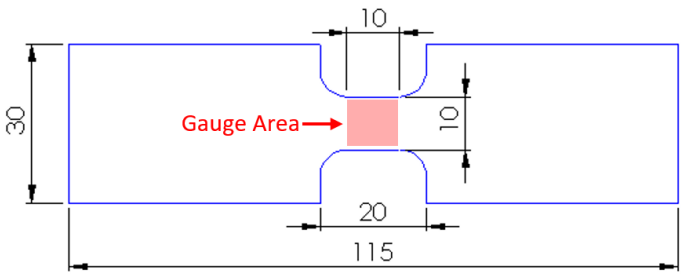


**Figure 3.2: Hot tensile specimen geometry. All dimensions are in mm.**

Before stripping the Zn coating, 3M masking tape (S-6540) was first applied on the gauge area of the Zn coated specimens where the zinc coating must remain intact. Then, both the bare and Zn coated

specimens were submerged in a solution of 50% hydrochloric acid and 50% water, for 30-60s to strip off the Zn coating. Finally, both the bare and Zn coated specimens were washed in a solution of 50% isopropanol and 50% water and dried in air. The masking tape was peeled off Zn coated specimens after drying, revealing intact Zn coating only at the gauge area.

### 3.2.3 Thermo-mechanical Cycles

Hot tensile tests were performed similar to the thermo-mechanical cycle shown in Figure 3.3. The specimen was heated in an atmospheric condition to the target temperature at a heating rate of 1000°C/s while the grips were allowed to expand with the thermal expansion of the coupon. 1000°C/s was chosen to replicate the temperature history of the steel sheets during RSW. When the target temperature was reached, the specimen was held for 0.5s for the temperature to stabilize throughout the sample before the specimen was strained at a constant displacement speed of 1mm/s until sample fracture. Additional extensometers were not used to measure strain. After fracture, the specimens were air cooled to room temperature.

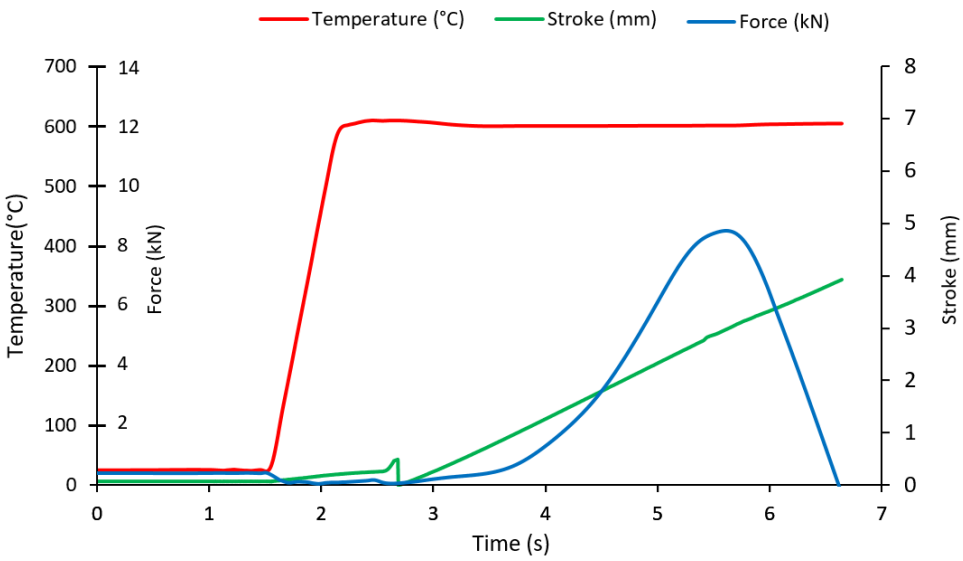


**Figure 3.3: Thermo-mechanical cycle**

The engineering stress strain curves are calculated from the recorded force and displacement values according to the equations shown in Eqs (3.1) and Eqs (3.2)

$$\sigma_E = \frac{F}{S_0} \tag{3.1}$$

$$\varepsilon_E = \frac{l - l_0}{l_0} = \frac{\Delta l}{l_0} \tag{3.2}$$

where F is the force applied to the specimen, $S_0$ is the initial section of the specimen, $\Delta l$ is displacement of the copper grips and $l_0$ is the initial gauge length of the specimen, which is 10 mm according to Figure 3.2

## 3.3 Effect of Weld Current, Time and Force on LME Cracking

### 3.3.1 Welding Equipment

The steel sheets were sheared into coupons of 25 x 25 mm for crack analysis. All coupons were cleaned with ethanol prior to welding. All spot welds were made using a 60Hz single-phase AC welding machine with class 2, female, B-type electrode caps having a face diameter of 7mm.

A triple pulse welding schedule is used for all welding procedures as shown in Figure 3.4. The welding schedule is recommended by A/SP[4] and consists of three identical pulses. Specific welding parameters such as the current, weld time and force varies depending on the thickness, material chemistry, and design of the experiments. Their exact values are discussed in Section 3.3.2.

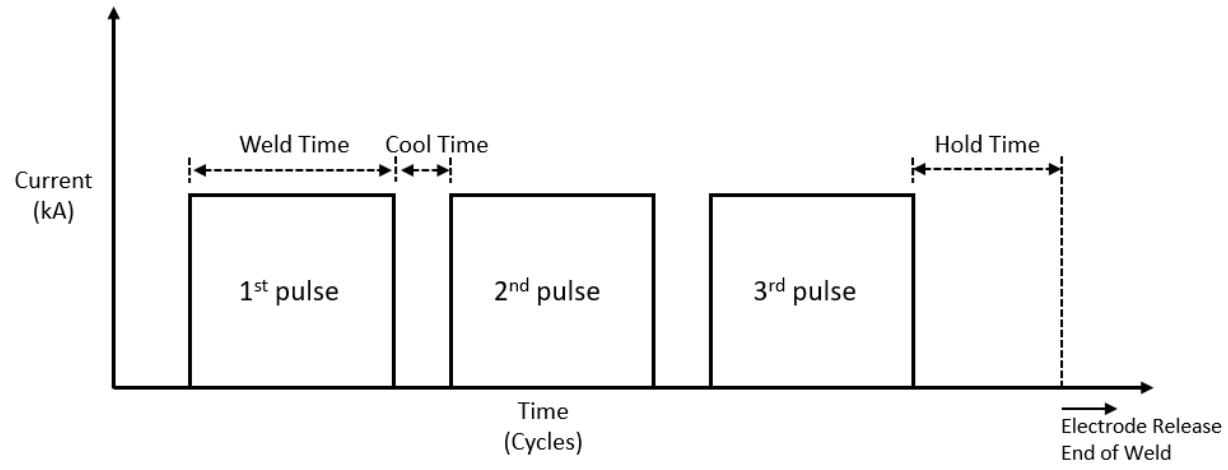


**Figure 3.4: Illustration of a triple pulse welding schedule and associated terminologies**

### 3.3.2 Central Composite Design

Studies have shown that weld current, weld time, and electrode force affect heat input, which in turn influence nugget diameter and LME severity [33,54,56,60,63]. Faced centered central composite design (CCD) was used to further quantify the effect of current, weld time and electrode force on the materials of interest while the cool time and hold time remained constant. The use of CCD allows the experimenter to check for interaction and quadratic effects between the variables. The CCD in this study was engineered so there are two replicates on both the corner and star points and five replicates on the center points.

Table 3.2 is the welding schedule used for spot welding materials in Table 3.1, having a thickness between 1.30 mm and 1.59 mm whereas

Table 3.3 is the welding schedules for materials equal to or greater than 1.60 mm thick. In both Table 3.2 and

Table 3.3, the baseline welding condition, coded as 0, is derived from recommendations given by the auto/steel partnership [4]. The low and high levels of weld current, weld time, and force are coded as -1 and +1 respectively. The cool time and hold time is constant for all levels

In both tables, $I_{min}$ is the current at which a minimum acceptable nugget size of $4\sqrt{t}$ can be achieved, where t is the thickness of a single sheet of material [5]. $I_{max}$, the expulsion current, is defined as the minimum current where three consecutive welds show expulsion. $I_{min}$ and $I_{max}$ was determined for each material as shown in Table 3.4.

**Table 3.2: Parameters and levels applied in $2^3$ factorial design for materials between 1.3mm-1.59mm thick**

| Parameters | Symbols | level | | |
|---|---|---|---|---|
| | | -1 | 0 | 1 |
| weld current (kA) | A | $I_{min}$ | $(I_{max}+I_{min})/2$ | $I_{max}$ |
| Weld time (Cycles) | B | 6 | 7 | 8 |
| Weld force (kN) | C | 3.2 | 4.2 | 5.2 |
| Cool time (Cycles) | | 1 | 1 | 1 |
| Hold time (Cycles) | | 10 | 10 | 10 |

**Table 3.3: Parameters and levels applied in $2^3$ factorial design for materials ≥1.6mm thick**

| Parameters | Symbols | level | | |
|---|---|---|---|---|
| | | -1 | 0 | 1 |
| weld current (kA) | A | $I_{min}$ | $(I_{max}+I_{min})/2$ | $I_{max}$ |
| Weld time (Cycles) | B | 7 | 8 | 9 |
| Weld force (kN) | C | 4.3 | 5.3 | 6.3 |
| Cool time (Cycles) | | 2 | 2 | 2 |
| Hold time (Cycles) | | 10 | 10 | 10 |

**Table 3.4: List of Imin and Imax for all materials of interest**

| Steel Grade | Sheet Thickness (mm) | $I_{min}$ (kA) | $I_{max}$ (kA) |
|---|---|---|---|
| QP980GI | 1.4 | 7.9 | 9.6 |
| QP980GA | 1.6 | 7.2 | 9.3 |
| DP980GI | 1.5 | 9.3 | 11.5 |
| DP980GA | 1.4 | 7.5 | 9.5 |
| QP1180GI | 1.6 | 8.3 | 9.3 |
| QP1180GA | 1.6 | 7.4 | 9.1 |

After the welds were completed according to the CCD design as outlined in Table 3.2 and

Table 3.3, the samples would be cross-sectioned and the nugget size and crack index data would be gathered following the procedures outlined in the crack analysis Section 3.4.

The statistical significance of each parameter and their combinations were evaluated using the Minitab software at 5% significance level. A multiple regression analysis was performed on a regression model, which corresponds to the following second order response function [71]:

$$y = \beta_0 + \sum_{i=1}^{k} \beta_i x_i + \sum_{i=1}^{k} \beta_{ii} x_i^2 + \sum \sum_{j<1} \beta_j x_i x_j + \varepsilon \quad \textbf{(3.3)}$$

where $\beta_0$, $\beta_i$, $\beta_{ii}$ and $\beta_{ij}$ are the coefficients of intercept, linear, quadratic and interaction variables. y is the dependent variable or the response, $x_i$ and $x_j$ are the independent variables in coded unit, and ε is the error term that accounts for the effects of excluded parameters. During the analysis, coefficients that caused the model (Eqs. (3.3)) to best fit a set of response variable data were determined by the least squares method with the aid of the Minitab software.

## 3.4 Suppression of LME via Aluminum Interlayer

### 3.4.1 Resistance Spot Welding with Aluminum Interlayer

TRIP 1100 and TRIP 1200 were the materials used in this study as they were shown in previous studies to be severely affect by LME cracking[59,64,67]. To measure how LME from the GI coating and the addition of the aluminum interlayer affect joint strength, samples were welded in three conditions. First, the zinc was stripped and the bare steel coupons were welded to measure the joint strength in the absence of LME. Secondly, the samples were welded in the as-received GI condition, to measure how joint strength is affected by LME. Lastly, samples were welded in the as-received zinc coated condition with aluminum interlayers placed between the outside surface of the joints and the electrodes.

The aluminum interlayer samples were prepared by placing aluminum foil between the zinc coated steel sheet and electrode contact surfaces. The welding electrodes would hold the sheets and foils in place during the welding process. Figure 3.5 is an illustration of the experiment setup.

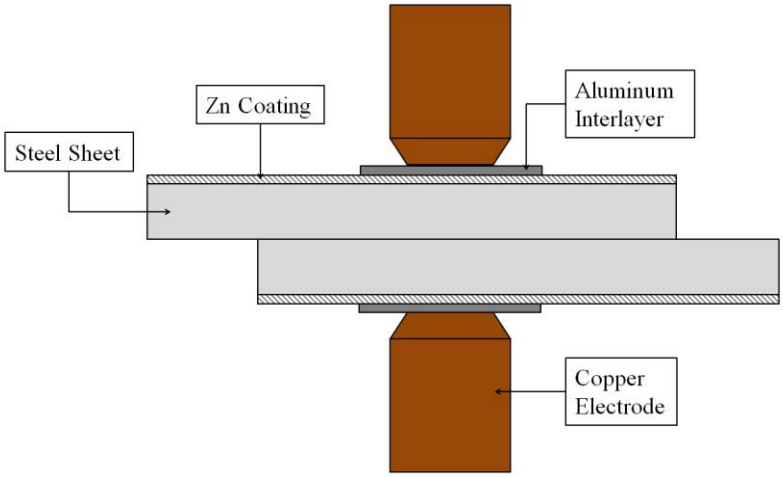


**Figure 3.5: Welding setup for aluminum interlayer**

All samples were cleaned with acetone to remove surface contamination prior to welding. All welds were performed on a medium frequency DC resistance spot welder. Aside from weld current, the welding parameters such as heating time, cooling time, hold time, and electrode force were selected based on recommendations by AWS D8.9 [35] and listed in

**Table 3.5 Weld parameters in accordance with AWS D8.9 [35].**

| Steel Grade | Thickness (mm) | Electrode Dia. (mm) | Force (kN) | Weld Time (cyc) | Hold Time (cyc) |
|---|---|---|---|---|---|
| TRIP1100 | 1.6 | 7.0 | 5.5 | 12 – 2 - 12 | 10 |
| TRIP1200 | 1.6 | 7.0 | 5.5 | 12 – 2 - 12 | 10 |

It has been shown that LME is more prominent at high welding currents [51,55]. To trigger LME as well as normalize welding conditions across different materials, coated samples of TRIP 1100 and TRIP 1200 were welded at expulsion current (Imax).

Since nugget diameter is the main determining factor for weld strength [72], the welding current for aluminum interlayer samples were increased by 8% to account for the thickness and resistance of aluminum interlayers. This ensured that the weld nuggets in the samples welded with aluminum interlayer

would be the same diameter as the weld nuggets produced in the other two conditions. The welding currents and average nugget diameters for all material conditions are listed in

Table 3.6. Five welds are examined for each material condition.

**Table 3.6: Welding current and nugget diameter for all material conditions**

| Material Condition | Welding Current (kA) | Avg Nugget Dia. (mm) |
|---|---|---|
| Coated TRIP1100 | 11 | 7.16 |
| Uncoated TRIP 1100 | 11 | 7.27 |
| Coated TRIP 1100+Al interlayer | 11.9 | 7.19 |
| Coated TRIP 1200 | 11 | 7.27 |
| Uncoated TRIP 1200 | 11 | 7.19 |
| Coated TRIP 1200+ Al interlayer | 11.9 | 7.21 |

### 3.4.2 Lap Shear Testing

The lap shear test is a common testing method for evaluating static weld strength since most welded structures are designed to carry tensile shear loads. Five samples from each material condition were lap shear tested. The lap shear samples were welded according to geometries illustrated in Figure 3.6. All lap shear tensile tests were performed using Instron Model 4206 tensile tester. A cross head speed of 2 mm/sec until failure was used for all samples. The mean lap shear strength for each material condition is plotted with 95% confidence interval.

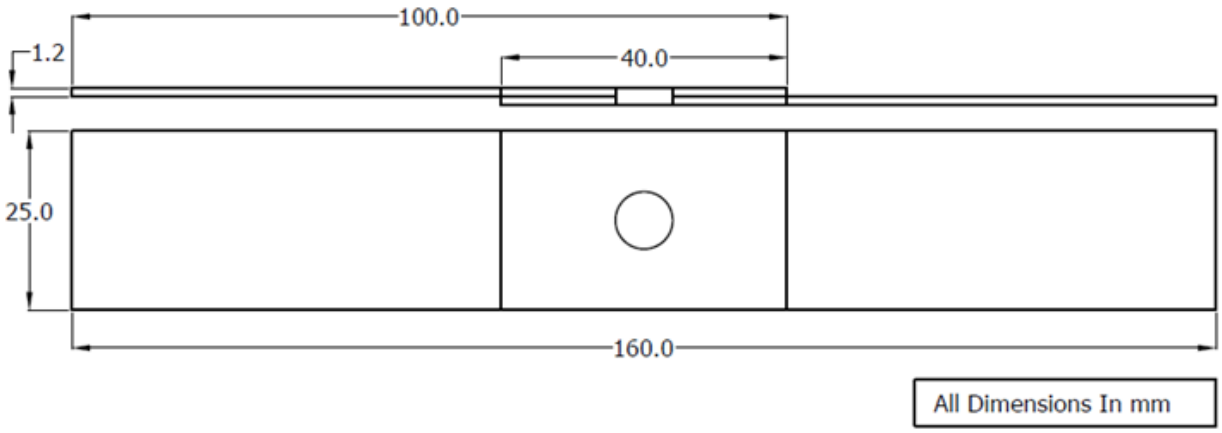


**Figure 3.6 Schematic of lap shear coupon**

## 3.5 Crack Analysis

After samples in Section 3.3 and Section 3.4 were welded, a stereo microscope at low (2 – 3 X) magnification was used to inspect for surface cracks. The cross-sectional plane for a weld was chosen so that it would intersect through both the center of the weld nugget and the greatest number of surface cracks as shown in Figure 3.7.

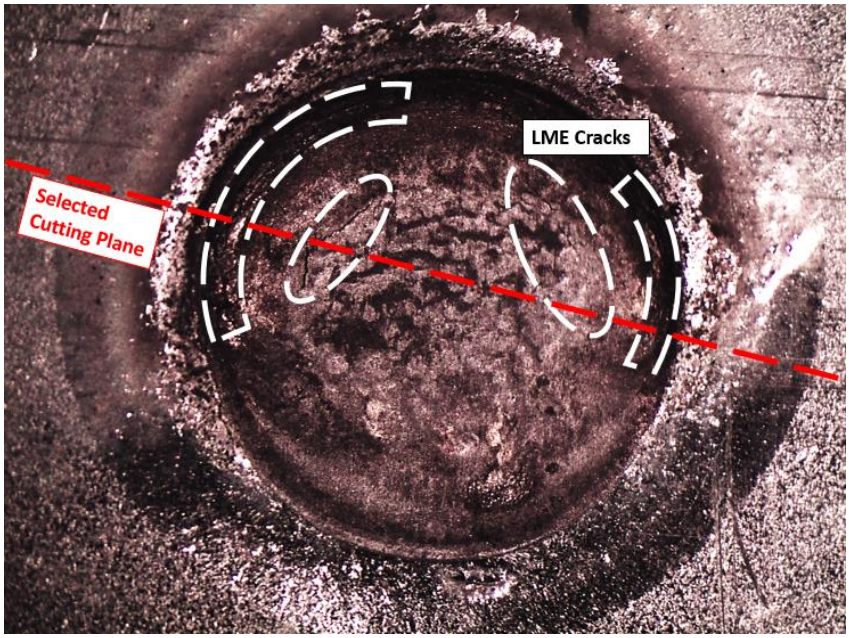


**Figure 3.7: Surface examination and cutting plane selection**

After cross-sectioning, all samples were hot mounted, ground and polished to a 1um diamond finish. Nital etching reagent at 5 wt.% concentration was used to reveal the macrostructure of the samples and LME cracks. The diameter of weld nugget and LME crack depths were measured for all the samples on the metallographic cross-sections of the welds as shown in Figure 3.8.

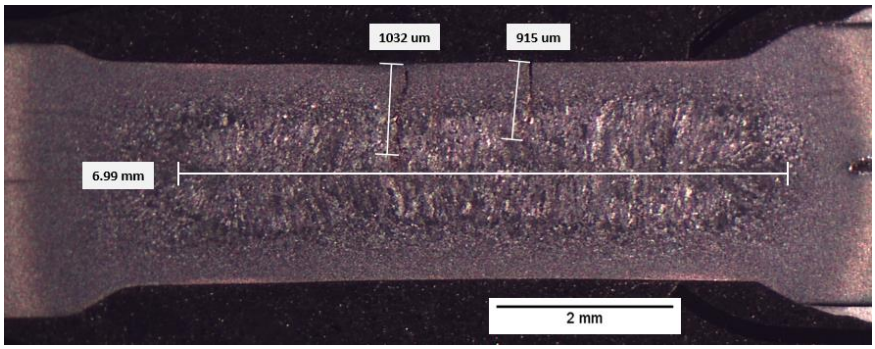


**Figure 3.8: Measurement of nugget size and LME crack depth**

The distribution of crack depths was used to calculate an LME crack index [62]. Since multiple LME cracks with varying lengths are present in a single weld as seen in Figure 3.8, the crack index simplifies the observation and provides a single value to gauge the severity of LME cracking for each crack type. The cracking index is defined in Eqs (2.3) and a higher crack index indicates a higher severity of LME cracking.

# Chapter 4 LME Susceptibility of Steels as Measured Using Hot Tensile Testing

LME susceptibility of steels is usually determined though hot tensile testing. Currently, a majority of studies evaluating LME susceptibility of steels only focuses on GI coated TWIP, TRIP and DP steels because earlier studies suggest they are highly susceptible [2,45,57,62,66]. There is little information on the LME susceptibility of QP steels because it is a newer type of steel. The LME susceptibility of GA coated steels have rarely been investigated either cause GI coated steels are more popular amongst automotive manufacturers in North America. In this study, hot tensile testing was conducted on QP1180, QP980 and DP980 that have been either GI or GA coated to study the LME susceptibility of the various combinations of steels and Zn coatings. From their ductility troughs, the influence of temperature, coating type, microstructure and material strength on LME have were established.

## 4.1 Confirmation of LME

Hot tensile results in Figure 4.1 shows that at 800°C, the GI coated QP1180 steel fractured at a strain of 0.15 whereas the bare steel fractured at a strain of 0.45. In short, the GI coated steel fractured at a substantially lower strain compared to its bare counterpart. Before any further analysis was conducted, the fracture surface of the bare and GI coated specimen were examined by SEM to determine if the premature failure of the GI coated specimen is caused by LME.

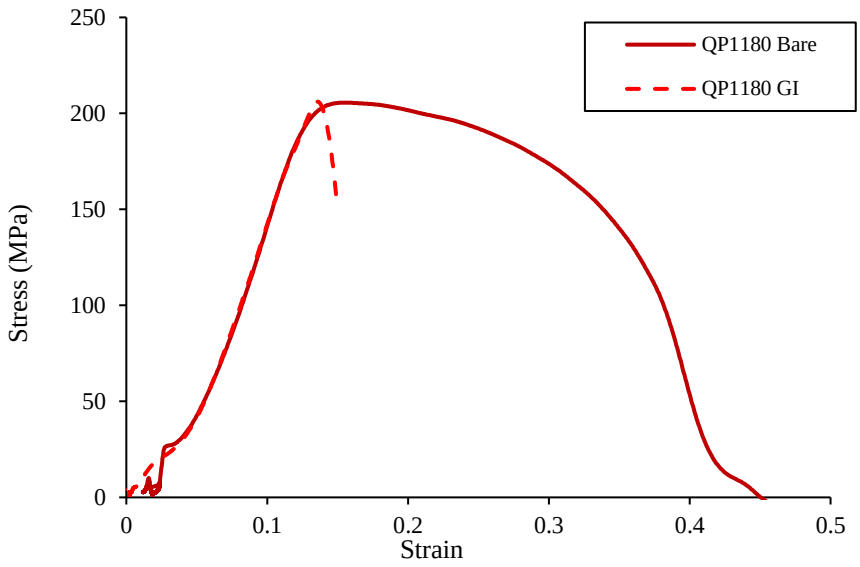


**Figure 4.1: Engineering stress strain curves of Bare and GI coated QP1180 steel hot tensile tested at 800°C.**

Figure 4.2(A) reveals high amounts of inter-granular cracking at the fracture surface of the GI coated QP1180, similar to what scholars have observed at LME cracks as shown in Figure 2.14. The sample also experienced brittle fracture as evidenced by minimal necking in Figure 4.2(B). Both observations are characteristic of the LME phenomenon [48]. In comparison, the bare steel sample experienced ductile fracture, as revealed by a high degree of necking and dimple like voids at the fracture surface shown in Figure 4.2(A) and Figure 4.2(B) respectively.

Observation of the fracture surface confirms that the premature failure is indeed caused by LME. Furthermore, the GI coated steel had the same elastic and plastic behavior of the bare steel prior to premature failure as shown in Figure 4.1. This behavior is another characteristic of the LME phenomenon [39,42,43].

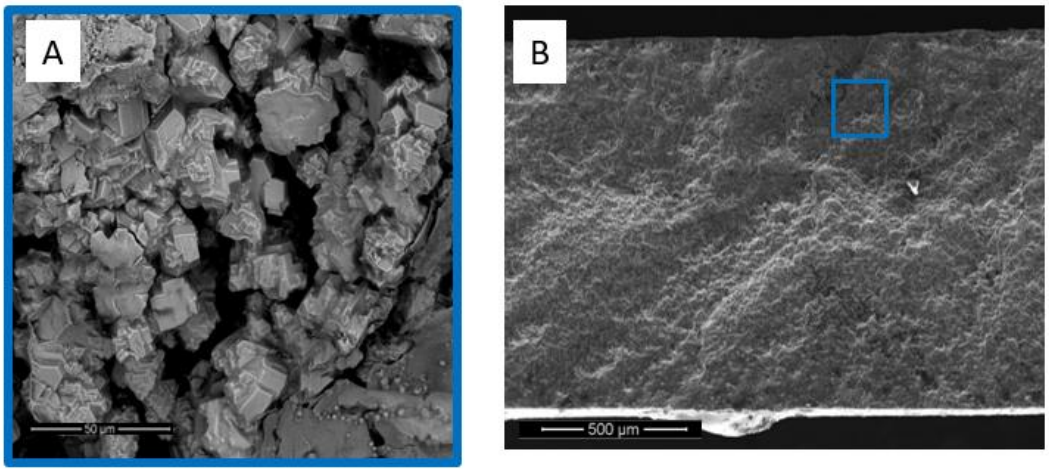


**Figure 4.2: (A) Detailed fracture surface of GI coated QP1180 steel hot tensile tested at 800°C (B) Overall fracture surface**

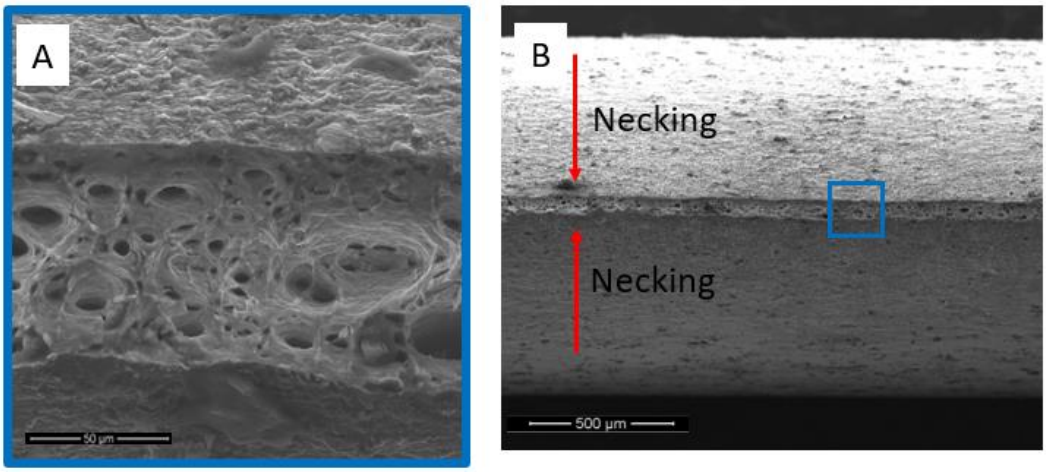


**Figure 4.3: (A) Detailed fracture surface of QP1180 bare steel hot tensile tested at 800°C (B) Overall fracture surface**

## 4.2 Influence of Temperature

The influence of temperature is investigated first because it was observed to have the most significant affect on LME susceptibility [2,36,45,47,48]. Due to the variety of steels tested in this study, the hot tensile behaviors of six types of steels and coating combinations are available. The hot tensile results of GI coated QP1180GI is used first to discuss the influence of temperature on LME because this combination was observed to be the most susceptible.

Hot tensile testing is conducted from 500°C to 1000°C at 100°C intervals for all the examined steels. The point of fracture for a Zn coated specimen is defined at the engineer stress and engineering strain when the hot tensile curve of the GI coated steel starts to deviate from the tensile curve of its bare steel counterpart. The point of fracture for a bare steel is defined at the engineering strain when its engineering stress drops to zero.

The select hot tensile results of GI coated QP1180 in Figure 4.4 shows that as temperature increased, premature fracture happened at lower engineering strains. Figure 4.4 also shows that as temperature decreased below 900°C, premature fracture only happened after necking has initiated. Both observations are consistent with the hot tensile results of DP steels observed by Jung *et al* [57].

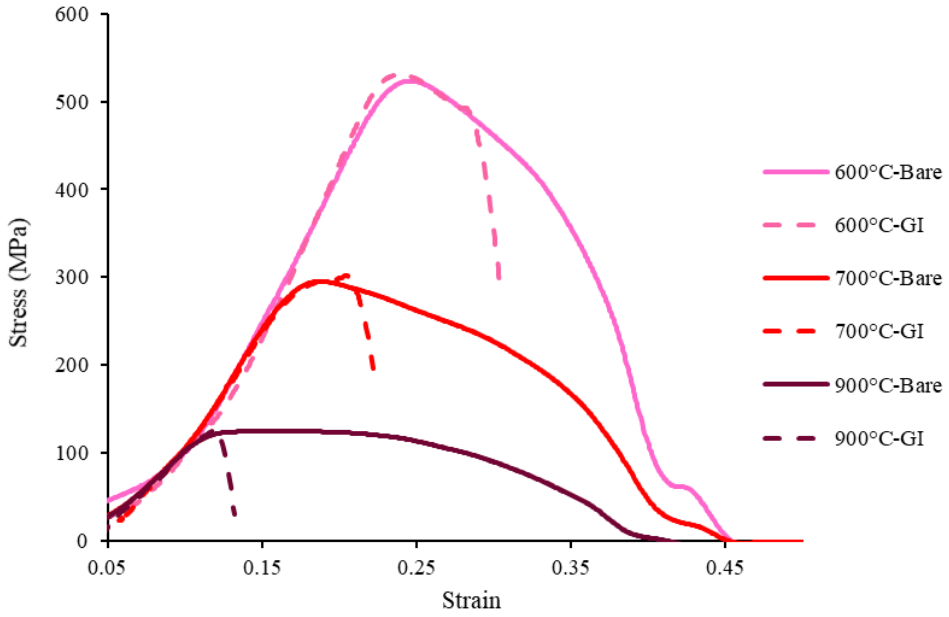


**Figure 4.4: Engineering stress strain curves of Bare and GI coated QP1180 steel hot tensile tested at 600°C, 700°C and 900°C respectively**

Fracture strain is plotted as a function of temperature for both the bare steel and the GI coated steel as shown in Figure 4.5(A). The fracture strain for the bare steel samples did not increase with increasing temperature. The dip in engineering strain for the bare steel sample observed at 900°C is likely caused by ductility-dip cracking and not an error in measurement [73]. On the other hand, the fracture strain for the GI coated samples between 500°C to 900°C dropped sharply as temperature increased due to LME [57]. At 1000°C, no ductility loss was observed.

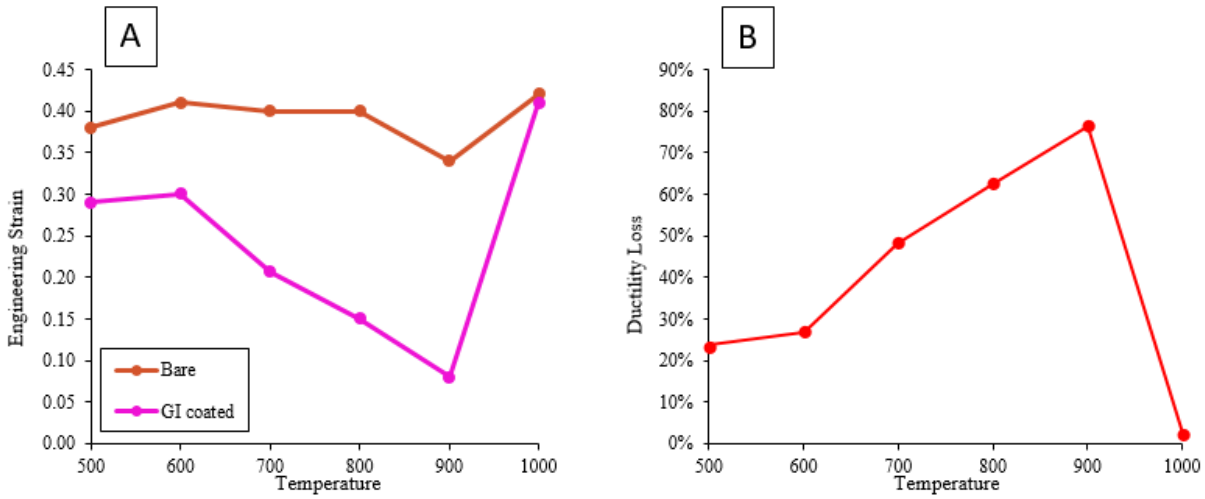


**Figure 4.5: (A) Engineering strain at fracture of bare and GI coated QP1180 steel during hot tensile testing (B) Ductility trough of GI coated QP1180 steel**

The critical temperature range in which the ductility of the steel is greatly reduced is know as the ductility trough [36,46]. The ductility trough is a popular tool to describe LME in a variety of solid/liquid systems [2,36–41,46]. The ductility trough for GI coated QP1180 steel in Figure 4.5(B) is calcuated from the engineering strain data in Figure 4.5(A) by using Eqs. (4.1). An increase in ductility loss indicates an increase in LME susceptibility.

$$Ductility\ loss\% = \frac{Strain_{Bare} - Strain_{Coated}}{Strain_{Bare}} \times 100\% \quad \textbf{(4.1)}$$

The ductility trough of GI coated QP1180 steel is between 500°C to 900°C as shown in Figure 4.5(B). From 500°C to 600°C, the ductility loss slightly increases and 25% ductility loss was observed on average. From 600°C to 900°C, the ductility loss rises sharply and peaks at 900°C with a ductility loss as high as 80%! From 900°C to 1000°C, the ductility loss decreases sharply. No ductility loss was observed at 1000°C.

Its interesting that 23% ductility loss was observed at 500°C. It is even conjectured that the ductility trough of GI coated QP1180 steel may even extend to the zinc melting point of 412°C. Little information is available for the LME susceptibility of steels below 600°C since a majority of steels are only susceptible to LME above 700°C, and the minimal test temperatures commonly only extend to 600°C. Only Barthelmie *et al* observed ductility loss in FeMn steel at temperatures as low as 450°C [53]. The LME susceptibility of

GI coated QP1180 at temperatures below what is commonly observed in literature provides new insight into the influence, or lack thereof of austenite on LME susceptibly below 600°C [57,74].

From 600°C to 900°C, the ductility loss of the GI coated steel rises with increasing temperature, which indicates a rise in LME susceptibility. This is the temperature range where a majority of reported TRIP, TWIP and DP steels start to exhibit ductility loss as well [46,48,57]. The rise in ductility loss with increasing temperature is commonly attributed to two factors. First, more liquid zinc is available as temperature increases [33,58]. Second, the critical stress required to initiate LME decreases with increasing temperature [2,49]. Both factors makes the zinc coated steel more embrittled as temperature increases, which leads to premature fractures at lower engineering strains.

QP1180 steel and other reported materials do not experience ductility loss above the zinc boiling point (904°C) [46,48,53,57]. Above this temperature, there is no liquid zinc to trigger LME, which leads to the ductility recovery of LME susceptible steels.

While the hot tensile test results of GI coated QP1180 steel is analyzed first in this section, the hot tensile behaviors of other types of GI coated steels are also available. Their ductility troughs in Figure 4.6 show that below 900°C, the ductility loss of QP980 and DP980 also increases with increasing temperature. Furthermore, no ductility loss was observed at 1000°C for both steels, similar to what was seen from the hot tensile testing of QP1180.

However, it is clear that there are differences between the ductility troughs of the investigated steels. QP1180 and QP980 experienced ductility loss at 500°C whereas DP980 only begun to experience ductility loss at 800°C. Furthermore, the degree of ductility loss is different between steels across all temperature ranges. These differences will be discussed further in Section 4.3.

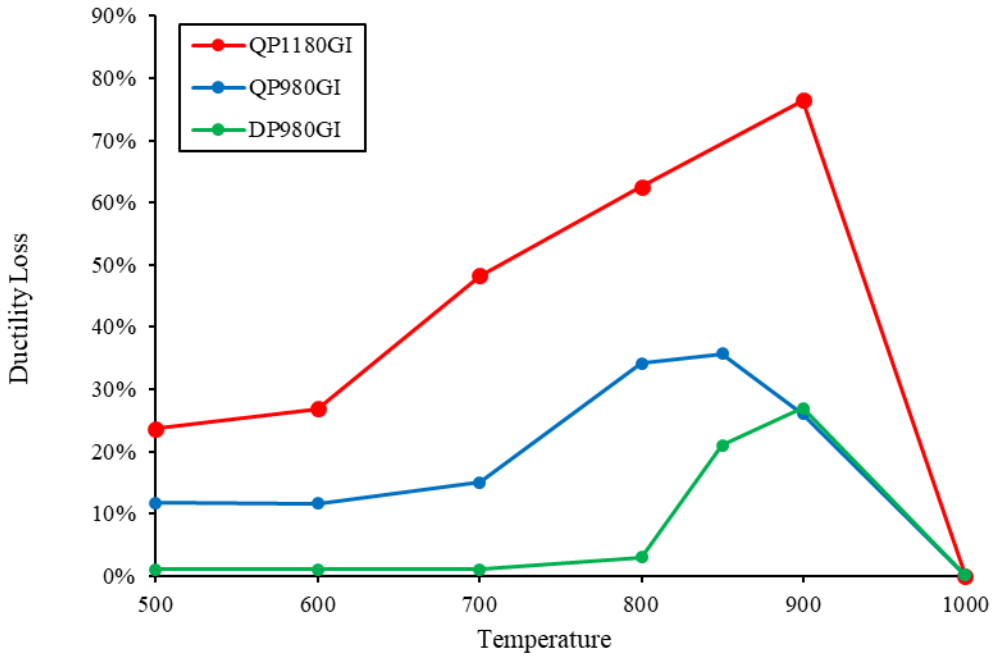


**Figure 4.6: Ductility trough of GI coated QP1180, QP980 and DP980 steels**

## 4.3 Influence of Material Microstructure and Chemistry

Since GI coated QP980 and DP980 steels are included in this study, it is convenient to compare the two steels that have the same tensile strength but different microstructures and chemistries to observe their influences on LME susceptibility.

The only notable similarity between the ductility troughs of QP980 and DP980 as shown in Figure 4.6 is that the ductility troughs of both steels generally increase with increasing temperature up to around 900°C. On the other hand, the ductility trough of QP980 begin at 500°C whereas the ductility trough of DP980 begin at 800°C. Furthermore, QP980 experiences more ductility loss than DP980 globally. The difference in the austenite content in the steels' microstructure and the Si contents in the steels' chemistry are the major differences between the two materials. The influences of theses factors on the ductility loss of the steels are discussed in Section 4.3.1 and Section 4.3.2 below.

### 4.3.1 Influence of Austenite Content

It is generally accepted that LME sensitivity is affected by the austenite phase content of the microstructure [55]. Some theorize that the austenite microstructure is inherently more sensitive to liquid

metal embrittlement [45][56]. Others say the dissimilar thermal expansion coefficients caused by austenite transformation in some materials may cause tensile stress to develop which promotes LME [57].

In order to determine the austenite content with respect to increasing temperature for the steels of interest, dilatometry was performed by heating the steels to 1100°C at a heating rate of 10°C/s. The zone of negative slop in the dilation curves shown in Figure 4.7 between 700°C and 1000°C is caused by the volumetric decrease when ferrite (α) is transformed to austenite (ɣ) [75]. The slight decrease in the dilation curves observed at 500°C for all the steels is caused by the decomposition of martensite into cementite [76].

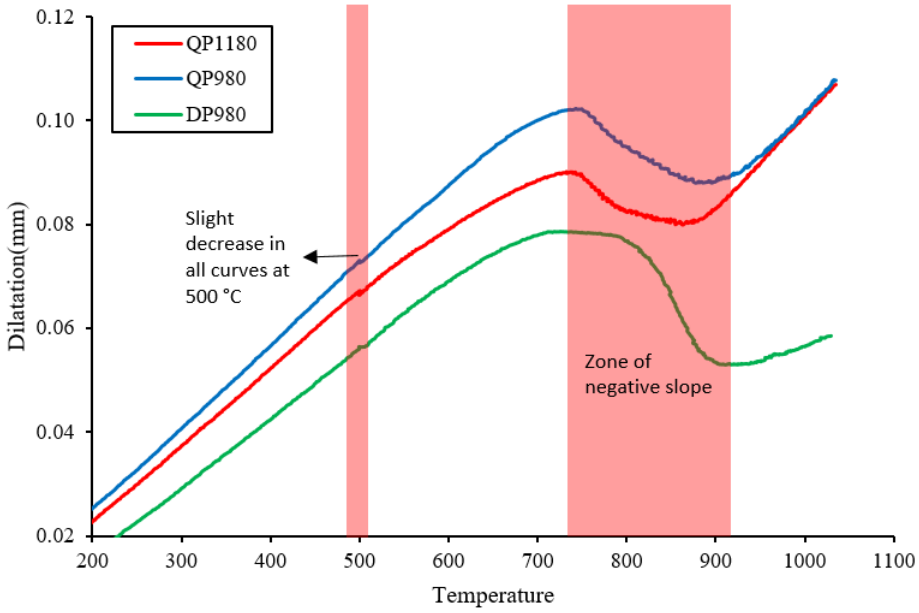


**Figure 4.7: Dilatometry curve of QP1180, QP980 and DP980 bare steel heated at a rate of 10°C/s**

It is clearly shown in Figure 4.7 that the thermal expansion coefficient is similar between all the examined steels as opposed to the findings by Jung [47]. The difference in thermal expansion did not cause the QP and DP materials to have different amounts of ductility loss.

The austenite percentage of each steel between the temperature range of 500°C and 1000°C is calculated from the dilatometry curves in Figure 4.7 by using a graphical method similar to the lever rule as shown in Figure 4.8 developed by Myers *et al* [77]. At any temperature, a vertical line may be drawn to intersect the dilation curve and the tangent lines. The volume fraction of transformed austenite at that temperature is expressed by:

$$\gamma_{trans} = \frac{AB}{AC} \qquad \textbf{(4.2)}$$

Where AB represents the amount of austenite already transformed. AC represents 100% of the transformed austenite.

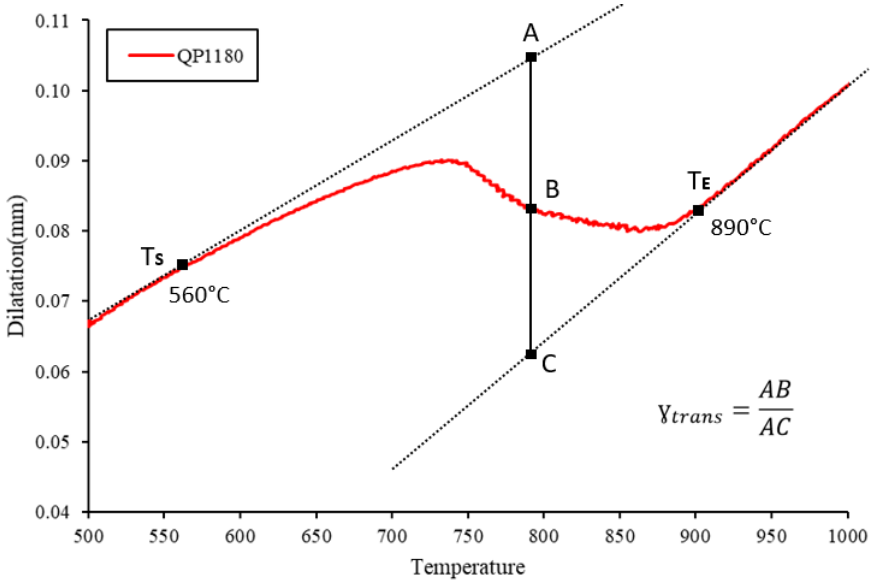


**Figure 4.8: Dilation curve showing graphical construction used to calculate fraction of phases formed. $T_S$ and $T_E$ indicate the start and end temperature of transformation.**

It is known that QP materials must have retained austenite in the room temperature condition [78]. XRD results indicate that QP1180 and QP980 contain 6 vol.% and 2 vol.% retained austenite respectively while DP materials do not have any retained austenite. The XRD results are combined with the dilatometry data to construct Figure 4.9, which depicts the austenite transformation rate with respect to temperature. In Figure 4.9, the austenite content in all the steel increases as temperature increases. At the same temperature, the difference in steel chemistry resulted in QP1180 having the highest austenite content, followed by QP980, and then DP980. DP980 is required to be approximately 50°C hotter to have the same of austenite content as QP980.

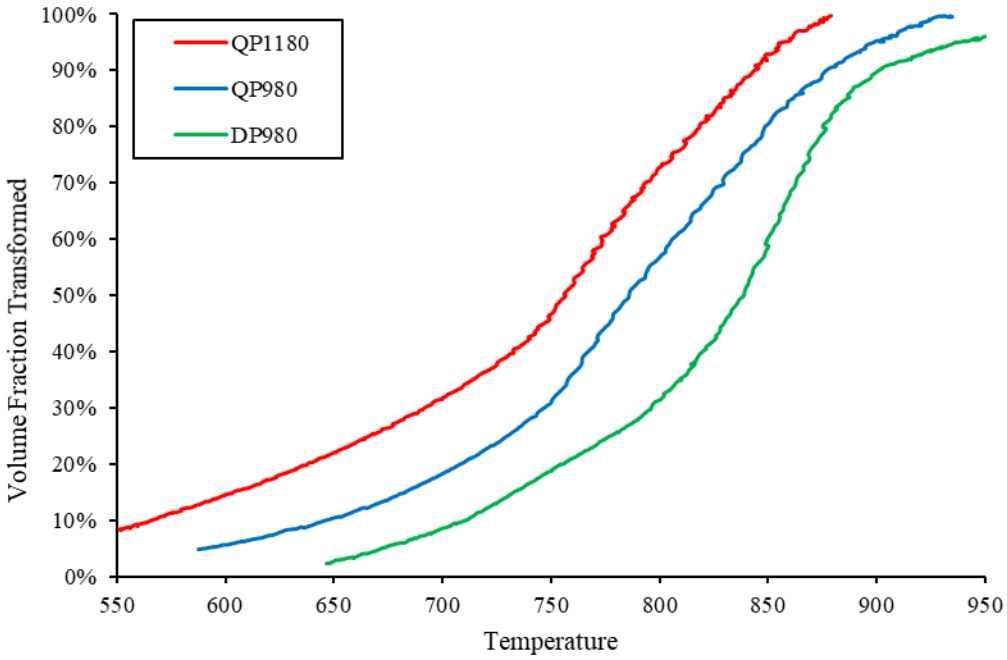


**Figure 4.9: Fraction of austenite transformed versus temperature for a heating rate of 10°C/min**

A relationship between austenite content and ductility loss is visualized in Figure 4.10 by combining the ductility loss with respect to temperature data in Figure 4.6 and the austenite content with respect to temperature data in Figure 4.9. The ductility loss of the steels in Figure 4.10 generally increases with increasing austenite content. A possible explanation is that austenite grains exacerbates LME by facilitating Zn diffusion and liquid Zn percolation along its grain boundaries [45]. The decrease in ductility loss at 100% austenite for QP980GI is due to Zn boiling off.

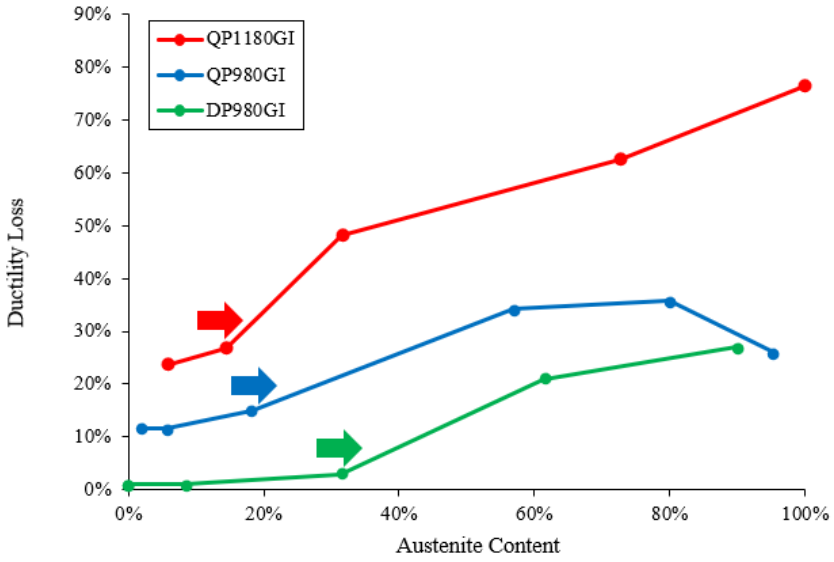


**Figure 4.10: Relationship between austenite content in the steel and the ductility loss caused by LME. Arrows indicate the point which ductility loss start to increase sharply for each material**

Some scholars argue that a minimum amount of austenite is necessary for the occurrence of LME [46], whereas others claim that a microstructure fully transformed to austenite is a key parameter for the occurrence of LME [56]. The arrows in Figure 4.10 indicate the austenite content after which ductility loss of the steel start to rise sharply. For GI coated QP1180 and QP980 steel, the ductility loss of both steels only started to increase greatly above 18 vol.% and 20 vol.% austenite respectively. Below this threshold, while the steels still experienced ductility loss due to LME, the amount of ductility loss is not greatly influenced by the austenite content of the steels. Similarly, for GI coated DP980, the ductility loss of the steel only started to increase greatly above 31 vol.% austenite. Below this threshold, GI coated DP980 experienced minimal ductility loss. From observations above, it is concluded that 18 vol.% to 31 vol.% austenite is the minimum amount required to trigger the rise in ductility loss in all the studied steels. Above this range of austenite content, an increase in austenite content leads to more ductility loss.

### 4.3.2 Influence of Si Content

As mentioned in Section 4.2, the QP980, QP1180 steel in this study, and a FeMn steel from Barthelmie *et al.* experienced ductility loss at temperatures below 600°C. On the other hand, the DP980 steel and a majority of studied steel in literature only experienced ductility loss above 700°C. It is discovered that this difference is due to the Si content of steels, which is rarely mentioned when studying the LME susceptibility of steels.

Si content in the steel plays an important role in controlling the speed of Fe diffusion into the Zn coating, which influences Fe-Zn intermetallic formation in the Zn coating. During hot dip galvanizing, Fe may diffuse into the Zn coating forming various Fe-Zn intermetallic as shown in Figure 2.5. According to the Fe-Zn binary phase diagram in Figure 2.18, the highest melting point of the Fe-Zn intermetallic start to dissolve above 672°C, which is well above the melting point of pure Zn at 419°C [15,79]. This layer of Fe-Zn intermetallic may act as a barrier that prevents contact between the liquid Zn and the steel substrate below 672°C, which should translates to no ductility loss during hot tensile testing at temperatures below 600°C [45,55].

On the other hand, the dissolution of Si from the steel into the Zn coating during hot dip galvanizing can inhibit the dissolution of Fe into the molten Zn [80][81], which suppresses the various Fe-Zn intermetallic phases. Specifically, a Si content above 0.5 wt.% is required for this reaction to occur [80][81].

The DP980 in this study only has a Si content of 0.45 wt.%, which not sufficient to suppress Fe-Zn intermetallic formation. Both QP980 and QP1180 in Table 3.1 have a Si content above 1.6 wt.%, which is more than enough to suppress the formation of Fe-Zn intermetallic. To confirm that Si content lead to a difference in Fe-Zn intermetallic formation between these steels, the thickness and composition of the zinc coating on QP980GI and QP1180GI was analyzed using EDX, as shown in Figure 4.11 and Figure 4.12 respectively. When analyzing the EDX line scans, the boundary of a material layer was defined as the point at which the height of the EDX curve decreased to half of its peak height [22].

To estimate the thickness of the Fe-Zn intermetallic layer in Figure 4.11, the half height was first determined for both Fe and Zn. A vertical line was drawn at the point where the Fe line scan intersected with the half height line of Fe to determine the transition point between the Fe and Fe-Zn intermetallic. A second vertical line was drawn where the Zn line scan intersected with the half height line of Zn to determine the transition point between the Zn and the Fe-Zn intermetallic. The distance between the two lines is the Fe-Zn intermetallic thickness[22].

The Fe-Zn intermetallic thickness for DP980GI in Figure 4.11 was approximately 3 um whereas the Fe-Zn intermetallic thickness for QP1180GI in Figure 4.12 was measured less than 0.5 um. QP1180 having a Si content above 1.6 wt.% did suppress the formation of Fe-Zn intermetallic where as DP980 having a Si content of 0.45 wt.% did not. As a result, DP980GI steel only started to exhibit ductility loss above 700°C due to the barrier effect of the Fe-Zn intermetallic whereas the QP steels in this study exhibited LME at temperatures below 600°C, as shown in Figure 4.6.

In the same line of thought, All of the GA coated steels should exhibit no ductility loss at temperatures below 700°C, as the GA coating in generally have high amounts of Fe content in the Zn

coating due to the annealing process. The difference of ductility loss in terms of Zn coating types will be discussed in detail in Section 4.4.

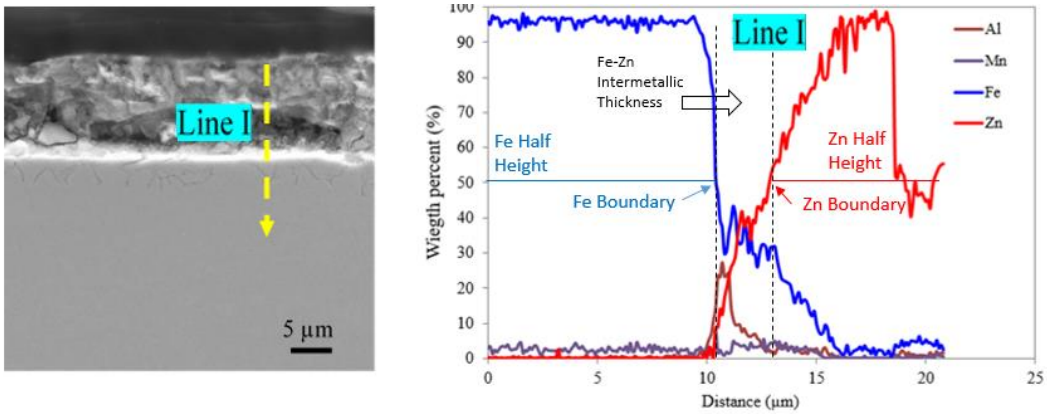


**Figure 4.11: EDX line scan of GI coated DP980 and measurement of Fe-Zn intermetallic thickness. Fe is in blue, Zn is in red.**

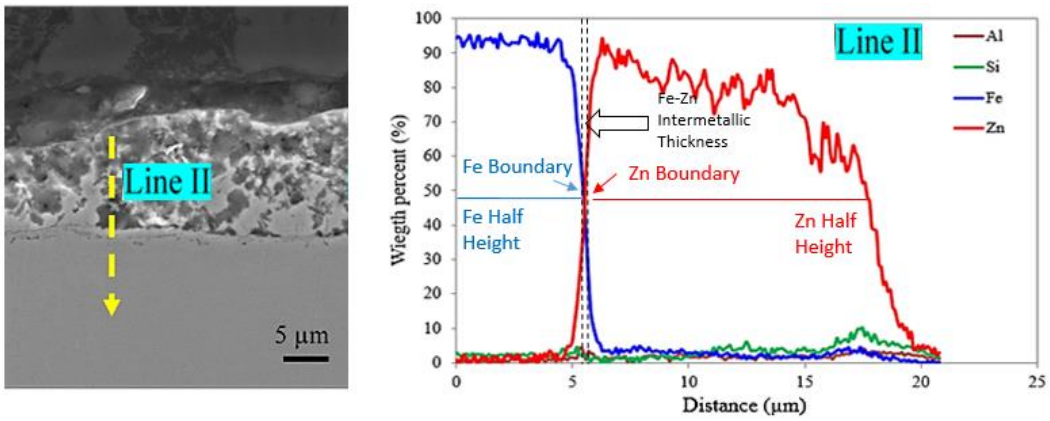


**Figure 4.12: EDX line scan of GI coated QP1180 and measurement of Fe-Zn intermetallic thickness. Fe is in blue, Zn is in red.**

## 4.4 Influence of Coating Type

As hinted in Section 4.3.2, all the GA coated steels should experience no ductility loss at temperatures below 700°C. The ductility troughs of GA coated steels in Figure 4.13 show that the GA coated steels indeed experienced no ductility loss at temperatures below 700°C. Furthermore, The GA coated steels experienced far less ductility loss globally than their GI coated counterpart.

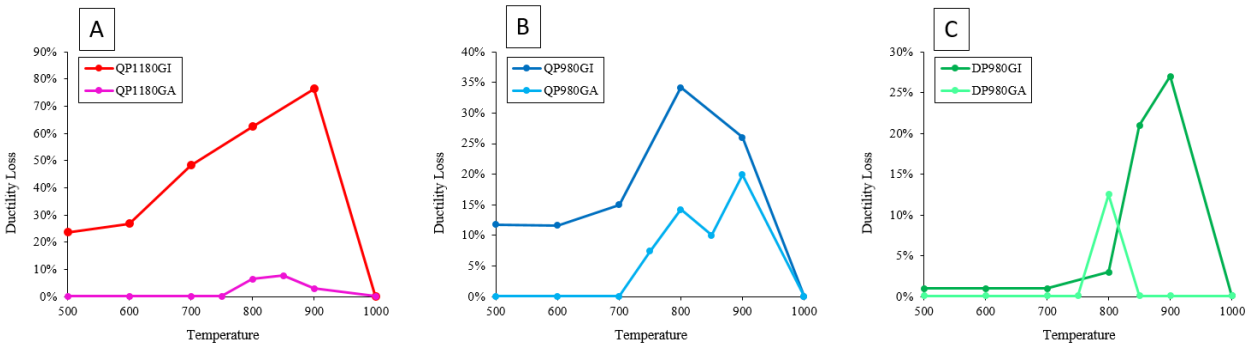


**Figure 4.13: Comparison of LME severity due to GI and GA coatings in (A) QP1180GI, (B) QP980GI and (C) DP980GI.**

It is important to note that the GA coating is on average 30% thinner than the GI coating as indicated in Table 3.1. SEM observations of the GI and GA coating in Figure 4.14 also show the GA coating to be thinner than the GI coating. EDX scans of the GA coating at Loc.1 in Figure 4.14(A) shows that the GA coating contains 21.2 wt.% Fe on average, meaning there is less Zn available in the GA coating. Overall, because the GA coating is alloyed with Fe and thinner than the GI coating, there is less liquid zinc available for LME, which translates to less ductility loss for the GA coating [45,55].

Not only is Zn less abundant for the GA coating, the GA coating is also inherently less susceptible to LME than the GI coating due to its high melting point. GA coatings in general are produced by annealing the galvanized steel at elevated temperatures, which results in a portion of the zinc layer to transform into $\alpha$-Fe (Zn) and various Fe-Zn intermetallic compounds[15,16,79,82]. EDX line scan of the GA coating on QP1180 steel (Figure 4.14(A)) confirms that the GA coating is indeed rich in Fe whereas minimal Fe is present in the GI coating (Figure 4.14(B)). EDX spectrum at Loc. 1 (Table 4.1) identifies the Fe-Zn intermetallic to be mostly $\Gamma 1$ phase, which can only start to dissolve after it has fully transformed to $\Gamma$ phase at approximately 672°C, as shown in Figure 2.18. On the other hand, EDX spectrum at Loc. 2 (Table 4.1) identifies the GI coating on QP1180 to be pure Zn, which melts at 419°C. The melting point of GA coating is approximately 250°C higher than the GI coating, which makes it less likely to cause LME cracking. Overall, the GA coating is a good alternative to minimize LME in susceptible steels.

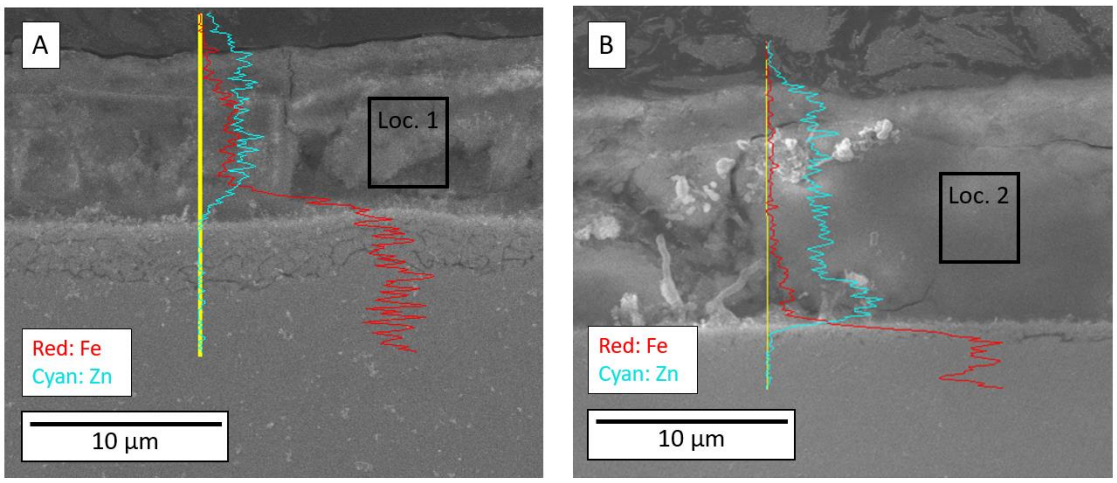


**Figure 4.14: EDX line scan of the (A) GA and (B) GI coating on QP1180 steel prior to hot tensile testing. Fe is shown in red, Zn in cyan.**

**Table 4.1: EDX spectrums showing weight percentage of Fe and Zn from Figure 4.14**

| Spectrum | Fe wt-% | Zn wt-% |
|---|---|---|
| Loc. 1 | 21.2 | 78.8 |
| Loc. 2 | 0.0 | 100.0 |

## 4.5 Material Ranking

Part of the goal of hot tensile testing is to determine the best combinations of steels and zinc coatings that are least susceptible to LME. To rank the combinations from best to worst, the average ductility loss of the respective combination is used. The average ductility loss is calculated as shown in Eqs. (4.3)

$$\text{Average ductility loss} = \frac{\int_{Tmelt}^{Tboil} DdT}{Tboil - Tmelt} \times 100\% \quad \textbf{(4.3)}$$

where $T_{melt}$ is the zinc melting point, $T_{boil}$ is the zinc boiling point and D is the ductility loss obtained from hot tensile testing at specified temperatures. The temperature range of liquid zinc is used because the presence of liquid zinc is a critical factor in triggering LME [36].

The average ductility loss can better reflect each combination's susceptibility to LME than the ductility loss at arbitrary temperatures or the maximum ductility loss for each combination. Since the LME cracks may experience maximum temperatures ranging from 700C to 900C during welding [47][33], The average ductility loss best reflects the material's susceptibility to LME on average when the welding schedule isn't specified.

The average ductility loss for each material and coating is shown in Figure 4.15. It is clear that GI coated QP1180 is most susceptible to LME whereas GA coated DP980 and QP1180 are the least susceptible. QP1180GA and DP980GA should be chosen for applications where LME susceptibility is a critical factor.

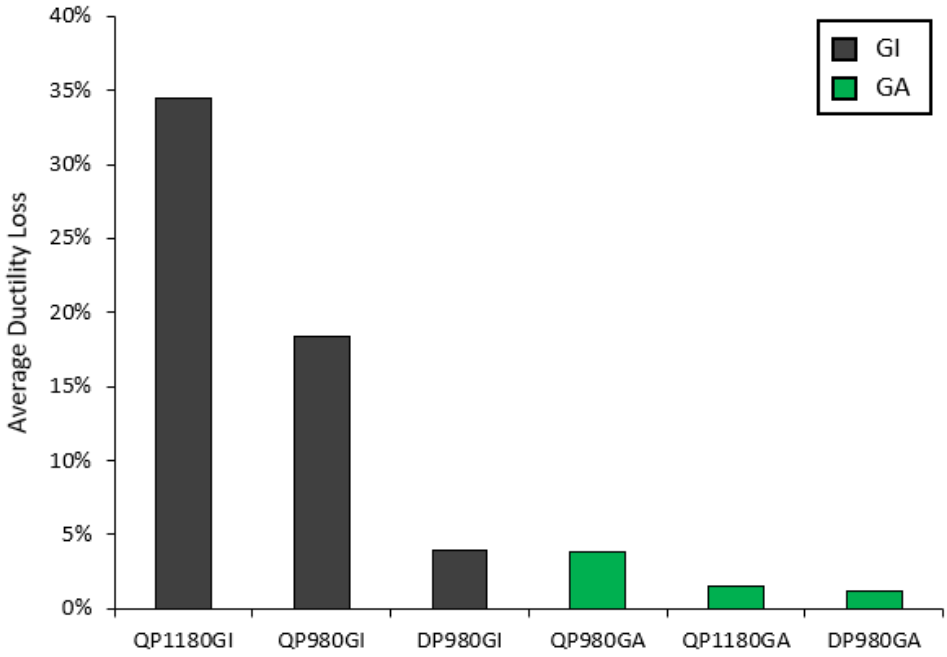


**Figure 4.15: Average ductility loss of examined steels**

## 4.6 Summary

The LME susceptibility of QP and DP steels of varying strengths and coating types have been evaluated via hot tensile testing. It was discovered that the austenite content of the steel microstructure, Si content in the steel's chemistry and the type of Zn coating all influence the behavior of the ductility trough of the examined steels.

As the austenite content of the steel increased, the ductility loss caused by LME increased as well. Approximately 18 vol.% to 31 vol.% austenite is the minimum amount required to trigger the rise in ductility loss of all the studied steels. In addition, steels containing a low Si content are more likely to form

a layer of Fe-Zn intermetallic between the steel substrate and the Zn coating. The Fe-Zn intermetallic acts as a barrier that suppresses LME at temperatures below its melting point of approximately 672°C. It was also discovered that the GA coated steels are far less susceptible to LME than their GI coated counterparts are. The GA coating contains less Zn than the GI coating because it is thinner and alloyed with Fe. The Fe alloying also causes the melting point of the GA coating to be 250°C higher than the GI coating. Finally, the LME susceptibility of the steels are ranked via their average ductility loss. QP1180GA is the most LME susceptible steel while DP980GA is the least.

# Chapter 5 Investigation into the Influence of Welding Parameters on LME via CCD

LME cracking is observed when spot welding LME susceptible steels. The LME susceptibility of the steels was investigated via hot tensile testing in chapter 4, which provided insight into the fundamental factors that influence LME susceptibility independent of the welding parameters. On the other hand, welding parameters also greatly influence the degree of LME cracking in the spot weld. In this chapter, the influence of welding parameters on the LME cracking severity in the spot weld was investigated via the central composite design (CCD) method. New weld lobes containing minimal LME cracks was also established for a majority of the studied steel.

## 5.1 Construction of CCD

Central composite experiment design (CCD) is an efficient methodology that minimizes redundant testing while also delivering robust results. It is used in this study to quantify the effect of weld current, weld time and electrode force on LME cracking severity for each steel. New weld lobes containing minimal LME cracks can also be established from the CCD results. While a CCD is constructed and implemented for each of the Zn coated QP and DP steels shown in Table 3.1, only the construction and analysis of the CCD for the GI coated QP980 steel will be discussed in detail, as the variation in material do not change the construction and analysis process.

The faced centered CCD design for GI coated QP980 with three parameters (current, time, force) and two responses (nugget diameter and crack index) are given in

Table 5.1. The experimental sequence (Run Order) was randomized in order to minimize the unexpected variability in the observed response.

**Table 5.1: CCD matrix and welding results of QP980GI**

| Standard Order | Run Order | Parameters | | | Nugget Diameter (mm) | Crack Index |
|---|---|---|---|---|---|---|
| | | A | B | C | | |
| 1 | 27 | -1 | -1 | -1 | 5.40 | 0.04 |
| 2 | 19 | -1 | -1 | 1 | 2.34 | 0.00 |
| 3 | 8 | -1 | 1 | -1 | 6.08 | 0.16 |
| 4 | 16 | -1 | 1 | 1 | 4.35 | 0.00 |
| 5 | 9 | 1 | -1 | -1 | 7.51 | 1.07 |
| 6 | 28 | 1 | -1 | 1 | 6.72 | 0.10 |
| 7 | 15 | 1 | 1 | -1 | 7.10 | 0.96 |
| 8 | 14 | 1 | 1 | 1 | 7.11 | 0.00 |
| 9 | 26 | 0 | 0 | 0 | 6.25 | 0.00 |
| 10 | 3 | 0 | 0 | 1 | 4.68 | 0.00 |
| 11 | 11 | 0 | 0 | -1 | 6.81 | 1.07 |
| 12 | 22 | 0 | 1 | 0 | 7.55 | 0.11 |
| 13 | 24 | 0 | -1 | 0 | 4.28 | 0.00 |
| 14 | 23 | 1 | 0 | 0 | 8.05 | 0.36 |
| 15 | 4 | -1 | 0 | 0 | 2.97 | 0.00 |
| 16 | 21 | -1 | -1 | -1 | 4.64 | 0.09 |
| 17 | 7 | -1 | -1 | 1 | 2.72 | 0.05 |
| 18 | 31 | -1 | 1 | -1 | 6.07 | 0.54 |
| 19 | 18 | -1 | 1 | 1 | 5.54 | 0.00 |
| 20 | 1 | 1 | -1 | -1 | 7.41 | 0.38 |
| 21 | 13 | 1 | -1 | 1 | 6.34 | 0.00 |
| 22 | 30 | 1 | 1 | -1 | 7.34 | 0.67 |
| 23 | 32 | 1 | 1 | 1 | 4.94 | 0.03 |
| 24 | 33 | 0 | 0 | 0 | 6.17 | 0.04 |
| 25 | 29 | 0 | 0 | 1 | 6.19 | 0.00 |
| 26 | 6 | 0 | 0 | -1 | 7.29 | 0.50 |
| 27 | 5 | 0 | 1 | 0 | 7.19 | 0.41 |
| 28 | 25 | 0 | -1 | 0 | 4.09 | 0.24 |
| 29 | 10 | 1 | 0 | 0 | 7.04 | 0.41 |
| 30 | 17 | -1 | 0 | 0 | 4.12 | 0.00 |
| 31 | 20 | 0 | 0 | 0 | 6.31 | 0.22 |
| 32 | 12 | 0 | 0 | 0 | 6.10 | 0.07 |
| 33 | 2 | 0 | 0 | 0 | 6.25 | 0.06 |

A: weld current; B: weld time; C: weld force

## 5.2 Regression Model for CCD

In the regression model, coefficients that caused Eqs. (3.3) to best fit the set of data collected in

Table 5.1 was determined by the least squares method with the aid of the Minitab software. All regressions were conducted on coded data. Table 5.2 shows the estimated coded coefficient (Coef) of each variable term for QP980GI in the regression model for nugget diameter and crack index along with their corresponding standard deviation (SDcoef), t-statistics (t-Stat) and probability (P) values determined at 5% significance level. Variable terms with P value smaller than 0.05 are A, B, C, AB, AC, BC, which are considered statistically significant for nugget diameter. For the crack index, the significant variables are A, B, C, AB, B2 and AC.

**Table 5.2: Estimated coefficient of the regression model**

| Term | Coef | SDcoef | t-Stat | P |
|---|---|---|---|---|
| Weld Diameter | | | | |
| Constant | 5.85 | 0.09 | 63.95 | 0.00 |
| A | 1.22 | 0.09 | 12.97 | 0.00 |
| B | 0.68 | 0.09 | 7.26 | 0.00 |
| C | -0.62 | 0.10 | -6.16 | 0.00 |
| A × B | -0.37 | 0.12 | -3.00 | 0.07 |
| A × C | 0.34 | 0.12 | 2.72 | 0.01 |
| B × C | 0.29 | 0.12 | 2.30 | 0.03 |
| | | | | |
| Crack Index | | | | |
| Constant | 0.17 | 0.01 | 11.46 | 0.00 |
| A | 0.12 | 0.02 | 6.56 | 0.00 |
| B | 0.04 | 0.02 | 2.43 | 0.02 |
| C | -0.14 | 0.02 | -7.21 | 0.00 |
| A × C | -0.10 | 0.03 | -3.81 | 0.00 |

A: current; B: time; C: force

Therefore, the second-order models for nugget diameter and crack index in terms of coded units with all significant variables are given in Eqs. (5.1) and Eqs. (5.2) respectively. $Y_1$, $Y_2$, A, B and C are nugget diameter, crack index, weld current, weld time and electrode force respectively.

$$Y_1 = 5.85 + 1.22A + 0.68B - 0.62C - 0.37AB + 0.34AC + 0.29BC \quad \textbf{(5.1)}$$

$$Y_2 = 0.17 + 0.12A + 0.04B - 0.14C - 0.1AC \quad \textbf{(5.2)}$$

The positive coefficients of variable terms in Eqs. (5.1) and Eqs. (5.2) indicate their synergistic effect, whereas negative sign indicates antagonistic effect. For example in Eqs. (5.1), 1.22A indicates that as the current increases, the size of the weld nugget also increases.

## 5.3 Model Adequacy Checking

Table 5.3 shows the analysis of variance (ANOVA) of the regression model for the nugget diameter (Eqs. (5.1)) and crack index (Eqs. (5.2)). The regression model and each variable term (linear and interaction) in the model show P values less than 0.05, thus they are statistically significant. The high P value (P > 0.05) of lack-of-fit indicates that the model is adequate for predicting the nugget diameter and the crack index. To test the global fit of the model, the coefficient of determination ($R^2$) were evaluated. The $R^2$ for weld nugget diameter was 0.932 and for the crack index 0.714. The high $R^2$ value for weld nugget diameter indicate that the model is highly significant for nugget diameter and provides a good estimate of the response within the experimental domain studied. On the other hand, the $R^2$ value of the crack index, being at 0.714, indicate that the model can only estimate the response with moderate accuracy. This is due to the difficulty in correctly quantifying the distribution of LME cracks where both the crack depth and the number of cracks have to be considered.

**Table 5.3: ANOVA of the regression model**

| Term | DF | Seq SS | F | P |
|---|---|---|---|---|
| Weld Diameter | | | | |
| Regression | 6.00 | 65.41 | 47.89 | 0.00 |
| Linear | 3.00 | 60.06 | 88.32 | 0.00 |
| Interaction | 3.00 | 5.35 | 7.83 | 0.01 |
| Residual Error | 26.00 | 4.78 | | |
| Lack-of-fit | 8.00 | 2.23 | 1.42 | 0.27 |
| Pure error | 18.00 | 2.55 | | |
| Total | 32.00 | 70.19 | | |
| | | | | |
| Crack Index | | | | |
| Regression | 4.00 | 0.86 | 24.33 | 0.00 |
| Linear | 3.00 | 0.73 | 31.04 | 0.00 |
| Interaction | 1.00 | 0.13 | 14.55 | 0.00 |
| Residual Error | 28.00 | 0.34 | | |
| Lack-of-fit | 10.00 | 0.21 | 1.55 | 0.17 |
| Pure error | 18.00 | 0.13 | | |
| Total | 32.00 | 1.20 | | |

DF=degree of freedom; Seq SS=sequential sum of squares;
F=F values from Fisher's statistical test

## 5.4 Visualization of Interactions

As shown in Eqs. (5.1) and Eqs. (5.2), current, time and force together with their interaction effects all play a part in controlling the nugget size and the crack index of the weld. The interaction between multiple factors make it difficult to gauge the change of individual factors on the response. For the ease of representation, Eqs. (5.1) and Eqs. (5.2) are converted to contour plots as shown in Figure 5.1. The interaction effects are expressed as curvatures of the contour lines. Figure 5.1 clearly identifies the effect of process variables on nugget diameter and the crack index of QP980GI in coded units.

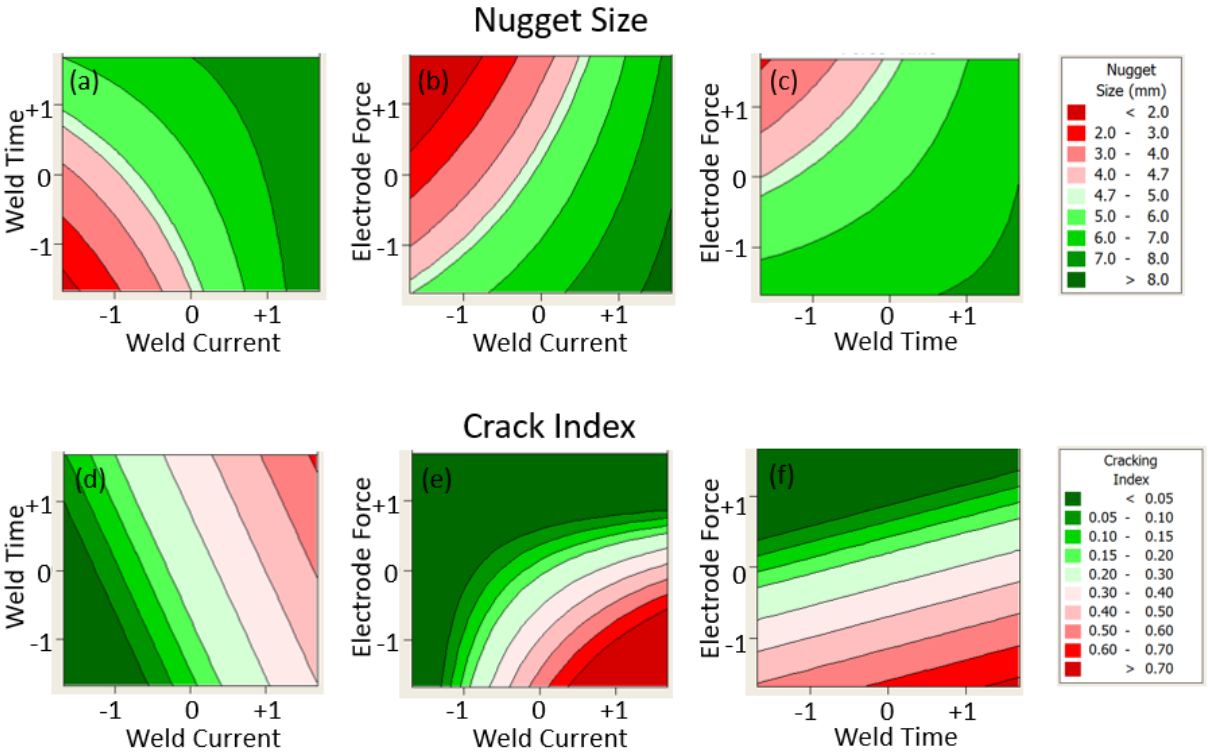


**Figure 5.1: Contour plot of nugget size and crack index of QP980GI**

In terms of nugget size, Figure 5.1 shows that increasing weld current and weld time increases the nugget size due to increases in heat input. Decreasing electrode force increases nugget size as well due to increases in sheet-to-sheet interfacial resistance. In terms of the crack index, Figure 5.1 shows that decrease weld current and weld time decreases the crack index. At the same time, electrode force should be set at high to prevent cracking at high current and high weld time.

The weld lobe diagram is a technique used to illustrate the range of weld current and weld time that can create acceptable weld nuggets [30]. In the weld lobe, the welding current and time are varied while

the other parameters such as weld force and hold time are kept constant. The left side of the lobe is defined by the minimum nugget size whereas the right size is defined by the occurrence of expulsion.

A modified weld lob of QP980GI is developed in Figure 5.2 by combining the nugget diameter information in Figure 5.1(a) and crack index information in Figure 5.1(b). The lower boundary of the weld lobe is set to the contour line of the minimum nugget diameter whereas the upper boundary is set to the contour line of the crack index being 0.2 instead of the expulsion current. Within the weld lobe, depicted in green, the resultant weld nugget would be above the minimum nugget size and have a crack index smaller than 0.2. A crack index of 0.2 is chosen to be the upper boundary so that the resultant weld would have a predicted strength loss less than 10% [62]. The data for expulsion current is also super-imposed into Figure 5.2 to visualize the effect of LME cracking on the shrinkage of the traditional weld lobe governed by expulsion current.

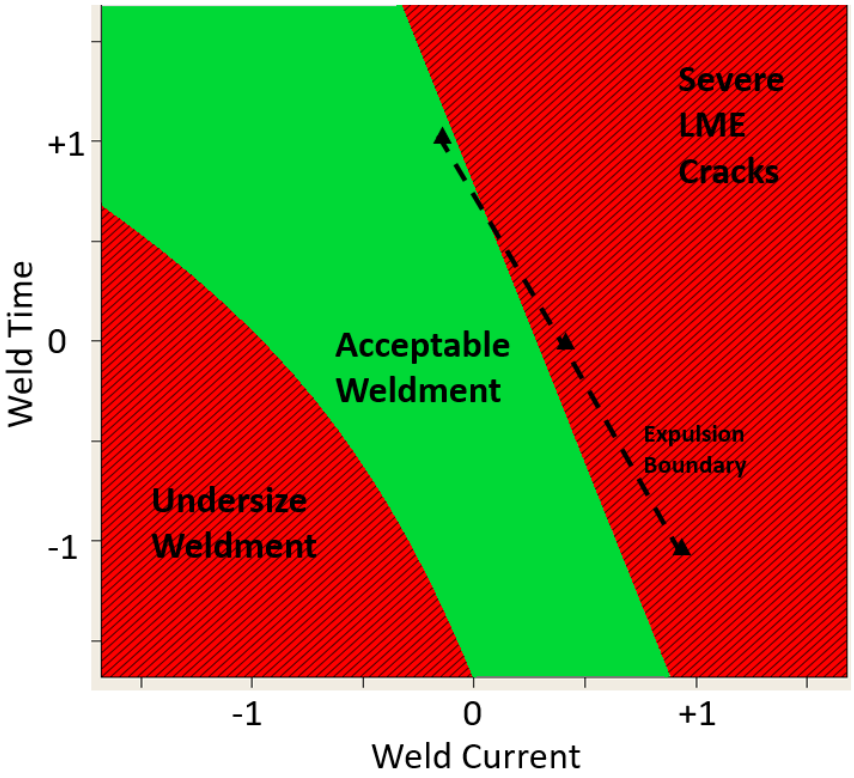


**Figure 5.2: Modified weld lobe of QP980GI**

In Figure 5.2, the contour line of the 0.2 crack index and the expulsion boundary slightly overlap with each other. In this case, LME cracking has minimal affect on the size of the traditional weld lobe. On the other hand, if a crack index of 0.1 were set as the upper boundary, the contour line for the crack index would shift left. This would not only cause it to no longer overlap with the expulsion boundary but also

reduce the weld lob significantly. As a result, the degree at which LME affects the weld lobe is dependent on the industry tolerance of LME cracks and the associated strength loss.

## 5.5 Comparison of Weld Lobes across Materials

In Figure 5.2, LME cracking marginally reduces the size of the traditional weld lobe for QP980GI with a crack index of 0.2. The same analysis was conducted to investigate if QP1180GI and DP980GI have similar trends between their expulsion current and crack index. The results of their modified weld lobes are plotted in Figure 5.3. The contour lines of the crack index is set at 0.2.

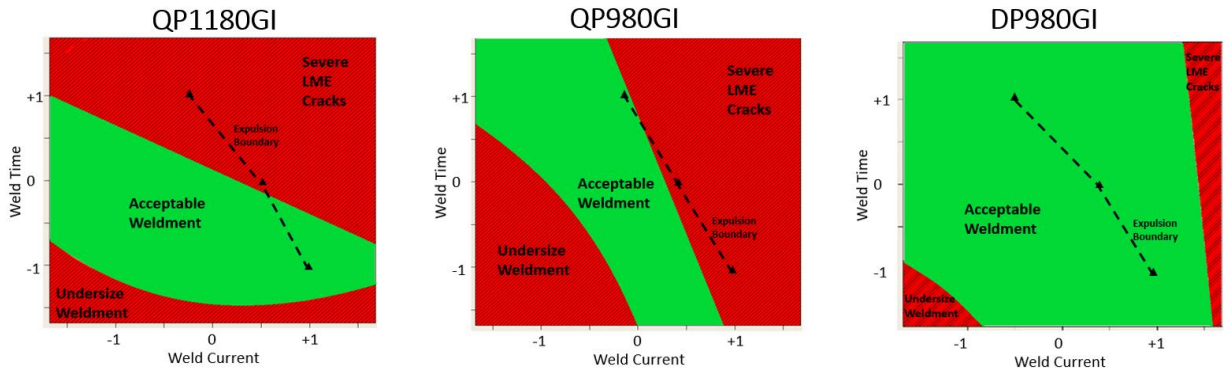


**Figure 5.3: Modified weld lobe of QP1180GI, QP980GI and DP980GI.**

In Figure 5.3, the expulsion current for each GI steel follows a similar trend. When the weld time is low, the steel would expulse at the high current setting. When the weld time is high, the steel would expulse at the mid point between the low and medium current setting. A consistent trend of expulsion current observed across steels helps to compare it with the contour line of the crack index set at 0.2.

The contour line of the crack index varies greatly across steel types. For both QP steel, the contour line of the crack index either run close to the expulsion boundary or intersect with it. For QP1180GI, the contour line of the crack index intersects with the expulsion boundary and restricts the weld lobe at low current and high weld times. On the other hand, the contour line of the crack index for DP980GI does not intersect with the expulsion boundary and does not restrict the weld lobe. The weld lobe of the GI coated DP980 appears to be the least affect by LME cracking. This observation is inline with the hot tensile test results where the GI coated DP980 experienced the least ductility loss.

To quantify the degree at which each steel is affect by LME cracking, the average crack for each steel is shown in Figure 5.4. The average crack index for each material is calculated as the average of the

LME crack index measurements from all 33 process conditions used for the CCD. For example, the average crack index for QP980GI is calculated by averaging the 33 crack index values in

Table 5.1. As shown in Figure 5.4, QP1180GI have the highest average crack index, followed by QP980GI, and then DP980GI. This material ranking is also inline with the average ductility loss ranking from hot tensile testing in Figure 4.15 of Section 4.5.

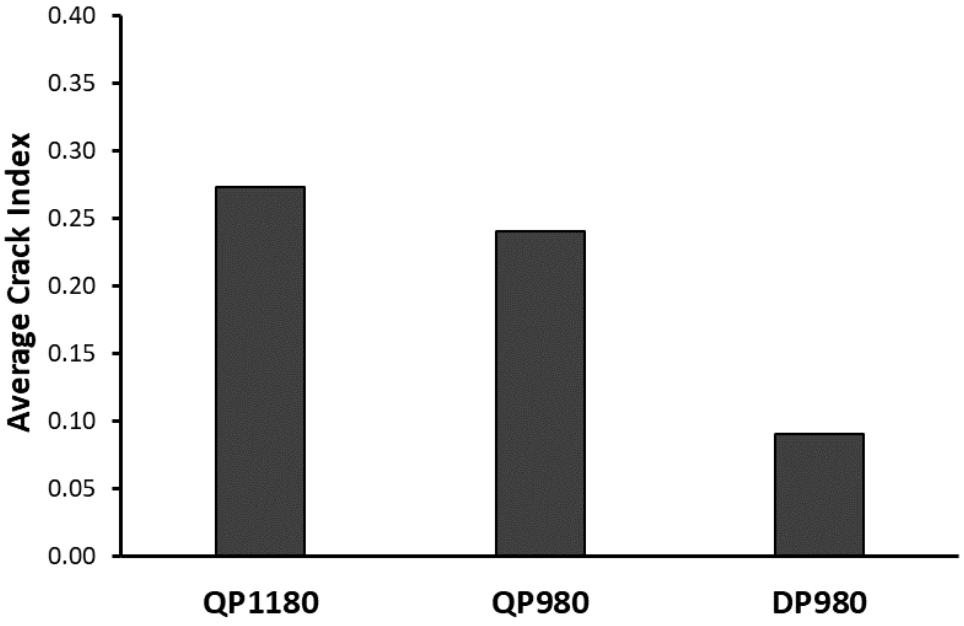


**Figure 5.4: Average crack index of GI coated QP1180, QP980 and DP980**

## 5.6 Effect of Coating Chemistry on LME during RSW

The average crack index for each GA coated steel is compared with their GI coated counterpart in Figure 5.5. The average crack index for each steel is calculated by taking the average of the sum of the crack indexes for all welding conditions across the experiment space. As shown in Figure 5.5, the GA coated steels are far less susceptible to LME than their GI coated counterpart regardless of the material type or strength. This observation is also in line with the findings during hot tensile testing. The GA coated steels are less susceptible than their GI coated counterpart because the GA coating contains less Zn than the GI coating as it is thinner and alloyed with Fe. The Fe alloying also causes the melting point of the GA coating to be 250°C higher than the GI coating. Detailed explanation on the chemistry of the coatings is in Section 4.4 of the thesis.

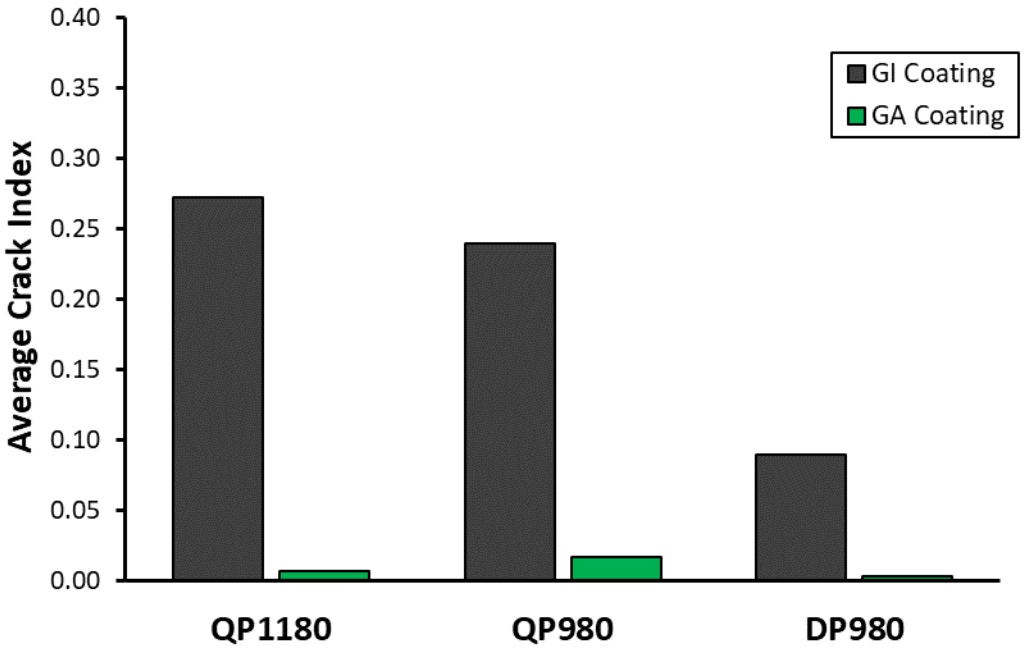


**Figure 5.5: Average crack index of GI and GA coated steels**

## 5.7 Relationship between Hot Tensile Testing and Welding Results

Hot tensile testing has the benefit of evaluating a material's LME susceptibility regardless of the welding schedule. As a result, it is easy to compare multiple materials' susceptibility to LME via hot tensile testing whereas it is difficult to do the same via RSW. However, hot tensile testing might not appropriately replicate the stress and heating conditions during actual spot welding[55]. Scholars have compared LME susceptibility in steels only via hot tensile testing and some even arrived at conflicting results[47,49]. There is no general consensus on whether the LME susceptibility obtained from hot tensile testing corresponds well with the LME cracking results of RSW.

In this study, the LME susceptibility of materials during hot tensile testing is quantified via the average ductility loss shown in Figure 4.15. The LME cracking during RSW is quantified via the average crack index shown in Figure 5.5. The comparison of steel susceptibility using both metrics is illustrated in Figure 5.6. Both metrics in Figure 5.6 reveal the same trend in LME susceptibility between steels. Both tests show that GA coated steels are less susceptible to LME than their GI coated counterparts are; QP steel is more susceptible to LME than DP steel of the same strength; Stronger steels are more embrittled than weaker steels. More importantly, Figure 5.6 shows that the LME result from hot tensile testing is

relevant to RSW and vice versa. Furthermore, the comparison between hot tensile testing and welding results is a novel contribution that has not been achieved before.

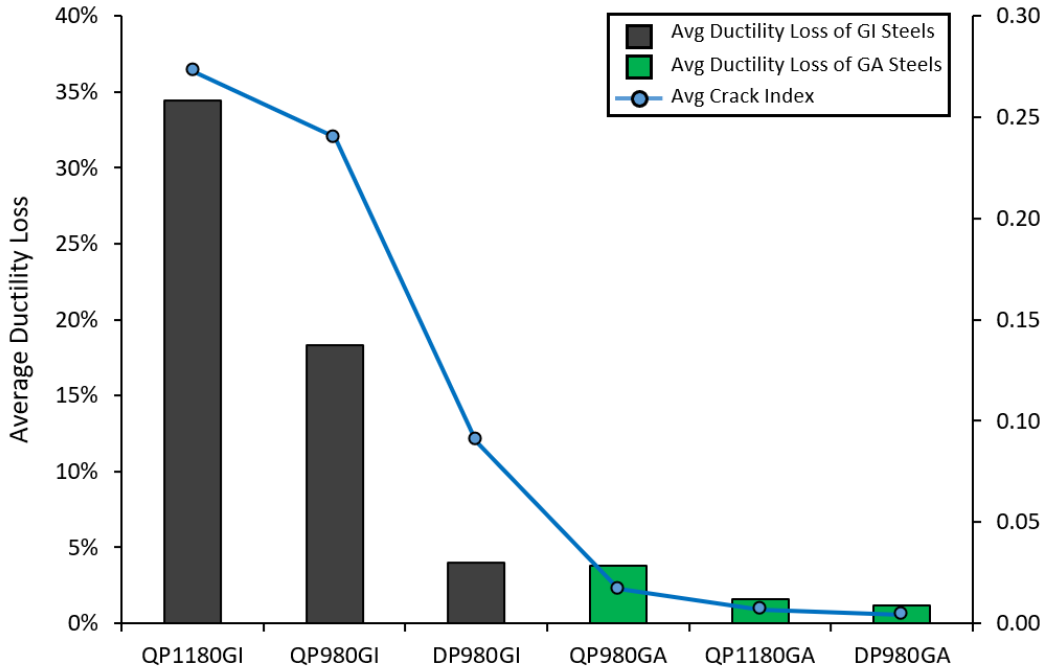


**Figure 5.6: Comparison between the average ductility loss from hot tensile testing and average crack index from RSW. Both metrics show the same trend between steels**

## 5.8 Summary

Central composite design (CCD) was discovered to be a suitable method to evaluate the effect of welding parameters on both nugget size and crack index. The model obtained from CCD was able to provide good estimation of the nugget size within the experimental region. Parameters that increase heat input increases nugget size. The model for crack index could only provide moderate estimation of the crack index within the experimental region due to the challenge in accurately quantifying the distribution of LME cracks in both length and quantity. However, the model still identified statistically significant terms that contribute to LME cracking.

The weld lobe of materials were not equally affected by LME. The weld lobe of DP980GI was completely unaffected whereas the low current and high weld time region of the lobe for QP1180GI was restricted. The influence of each welding parameter on LME cracking varies depending on the steel and it is best to evaluate new steels on an individual basis.

The materials are ranked from the most LME susceptible to the least by comparing their average crack index from spot welding. QP1180GI was determined to be the most LME susceptible, followed by QP980GI, and then DP980GI. GA coated steels were also far less susceptible to LME than their GI coated counterparts. The same trend was also observed during hot tensile testing. Therefore, hot tensile testing results are confirmed to be representative of the LME susceptibility during welding.

# Chapter 6 Suppression of LME via Aluminum Interlayer

As discussed in Chapter 5, the welding parameters have a large impact on the LME severity during RSW. Furthermore, LME can be reduced by selecting welding parameters that are not favourable for it to occur. This entails reducing the heat input by lowering the weld current, lowering the weld time, and increasing the electrode force. However, this method is not ideal as it restricts the weld lobe.

In this chapter, LME cracking in TRIP 1100 and TRIP 1200 steels was suppressed by placing aluminum interlayers added between the electrode and steel contact surface. Compared to welds exhibiting LME, TRIP 1100 with aluminum interlayers showed complete strength recovery while TRIP 1200 with aluminum interlayers resulted in a recovery of strength by 90%. Aluminum interlayers suppress LME by formation of iron aluminides that hinder liquid Zn from coming in contact with the steel substrate, thus preventing LME.

## 6.1 Metallography Examination

Weld nuggets in the coated condition and aluminum interlayer condition were cross-sectioned and examined using a stereo microscope. As shown in Figure 6.1, long cracks (>300 μm) were observed in the cross-section in zinc coated TRIP 1100 while no cracks were observed in the cross-section in aluminum interlayer TRIP1100 in Figure 6.2. The stereo-micrographs show that aluminum interlayer is a potential method of suppressing LME. Further analysis is required to quantify the degree at which LME is suppressed and to understand the reactions responsible for the observed decrease in LME.

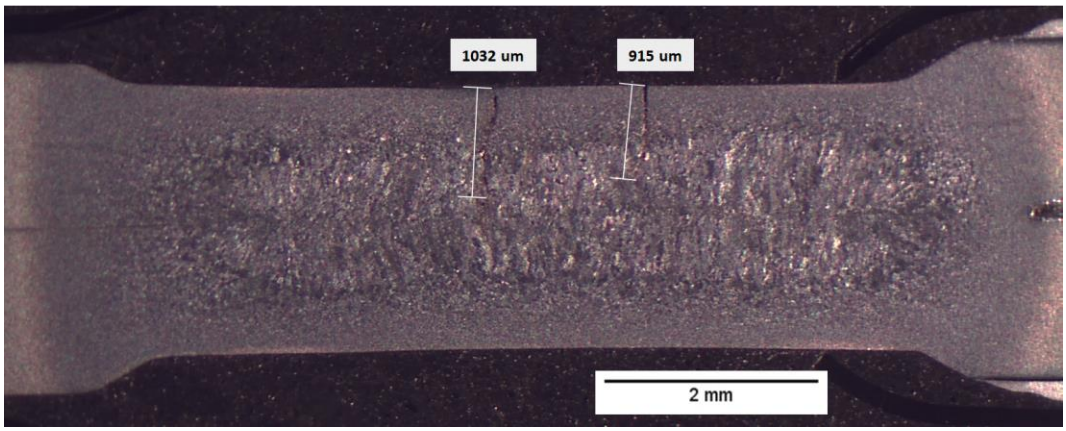


**Figure 6.1 Zinc coated TRIP 1100 sample with observable LME cracks**

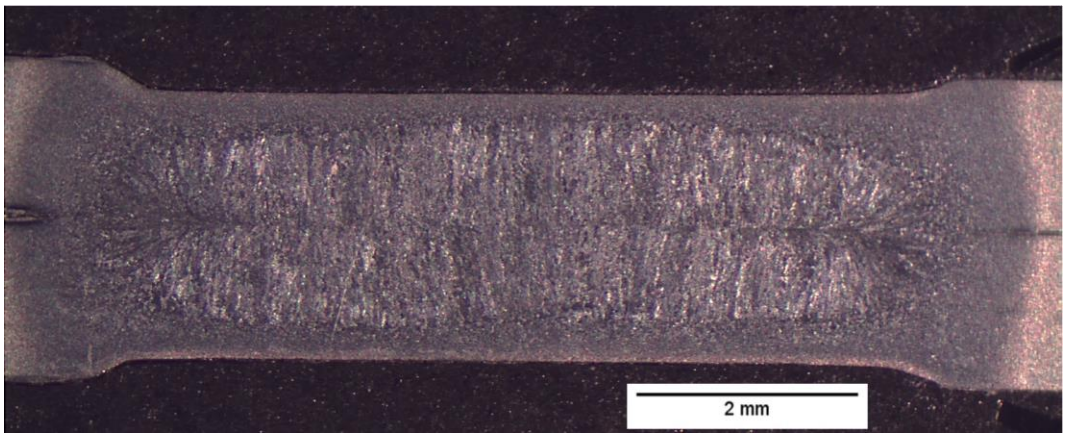


**Figure 6.2 Zinc coated TRIP 1100 sample welded with aluminum interlayer, free of LME cracks**

The number of cracks per sample is one indicator of LME severity [50]. A reduction in number of cracks would further qualify the use of aluminum interlayers as a successful suppression method. For both TRIP 1100 and TRIP 1200 in Figure 6.3 and Figure 6.4, when aluminum interlayers were used, the number of cracks observed between all crack lengths was greatly reduced. Use of the aluminum interlayer is slightly less effective in TRIP 1200 than in TRIP 1100 since more cracking between 10 μm and 25 μm long was observed for aluminum interlayer TRIP 1200 samples.

Through the use of aluminum interlayers, the average length of cracks decreased as well. Compared to coated samples in Figure 6.5, the average crack length for TRIP 1100 samples decreased by 70% while the average crack length for TRIP 1200 samples decreased by 30%. Aluminum interlayer is less effective in the reduction of crack length in TRIP 1200 than in TRIP 1100 possibly due to a difference in base material chemistry. TRIP 1200 has higher manganese content that helps to stabilize austenite formation. Higher austenite content in TRIP 1200 leads to more LME cracking that requires more aluminum interlayer to fully suppress LME [2,83].

The crack index, a method that can account for both crack length and number of cracks, was also used to evaluate cracking [67]. As shown in Figure 6.6, using aluminum interlayers to weld the TRIP 1100 and TRIP 1200 reduced the cracking index for both materials by over 85%. As fewer cracks were seen, and the cracks were shorter, there was less crack initiation along the load path, and the cracks that did initiate did not propagate as far. The low cracking index indicates that there should be minimal deteriation of spot weld mechanical properties due to LME [67].

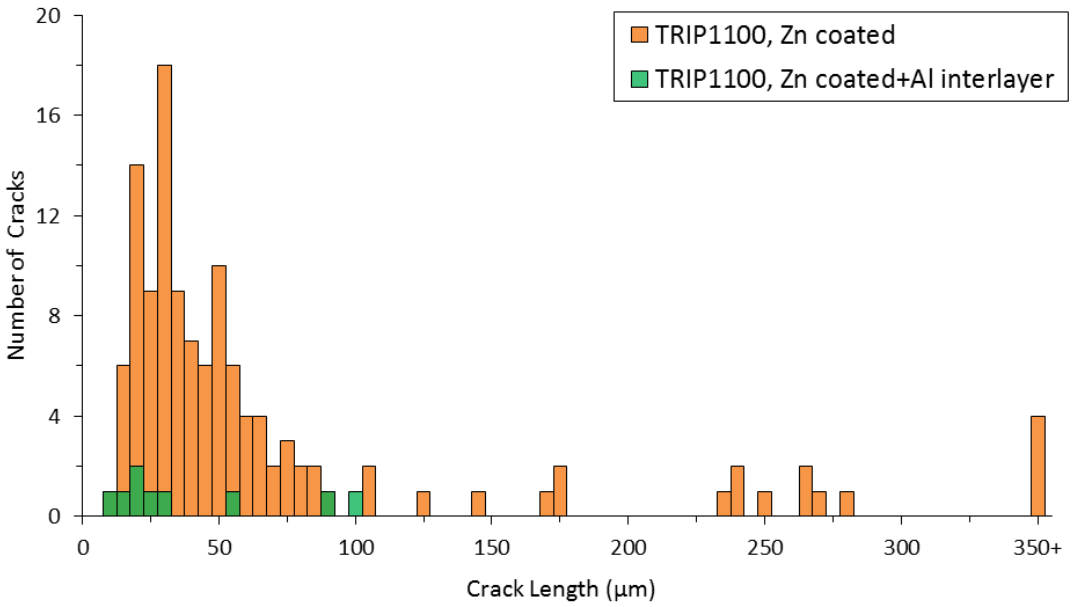


**Figure 6.3 Crack length distribution in five welded samples of TRIP 1100 in coated and aluminum interlayer conditions**

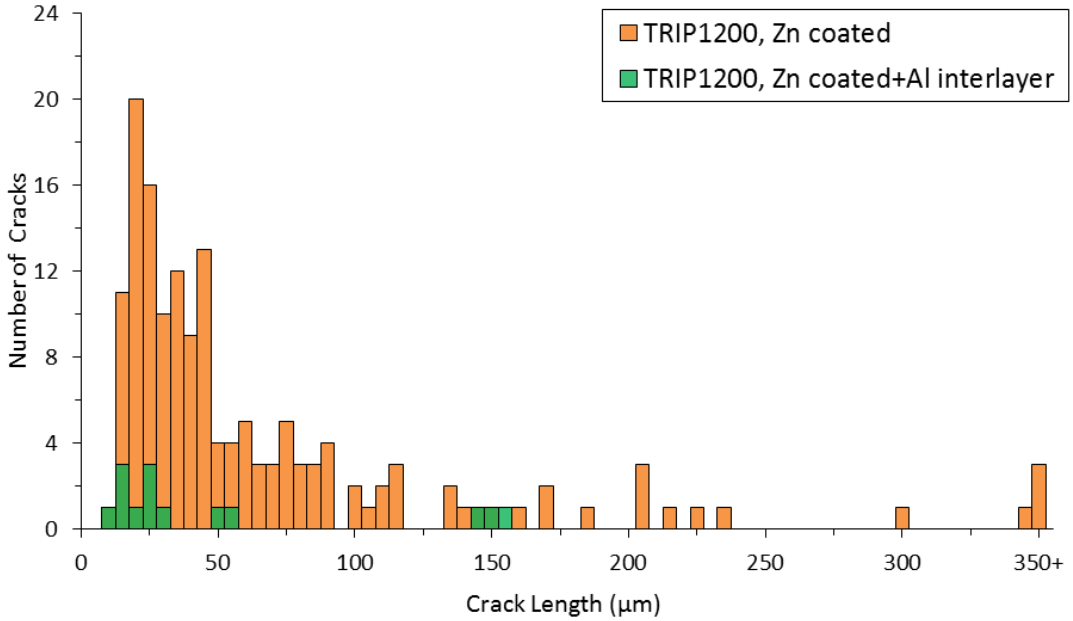


**Figure 6.4 Crack length distribution in five welded samples of TRIP 1200 in coated and aluminum interlayer conditions**

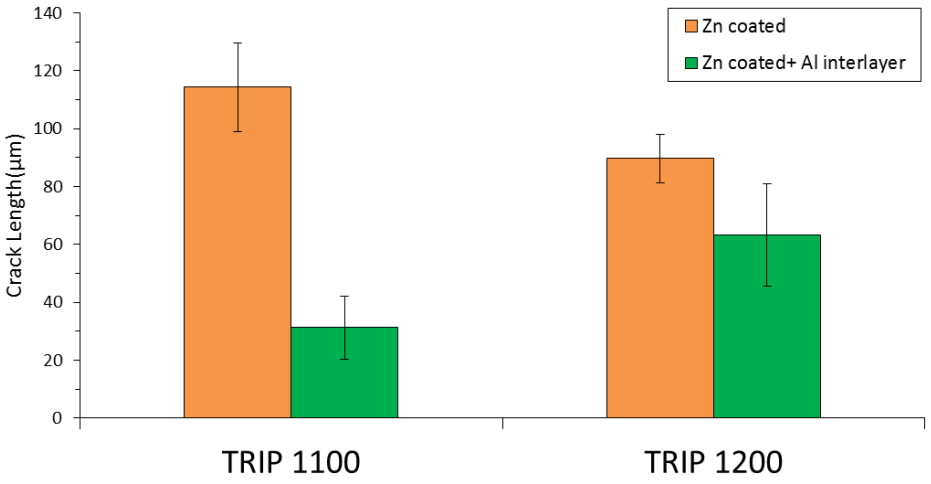


**Figure 6.5: Average crack length for all material conditions**

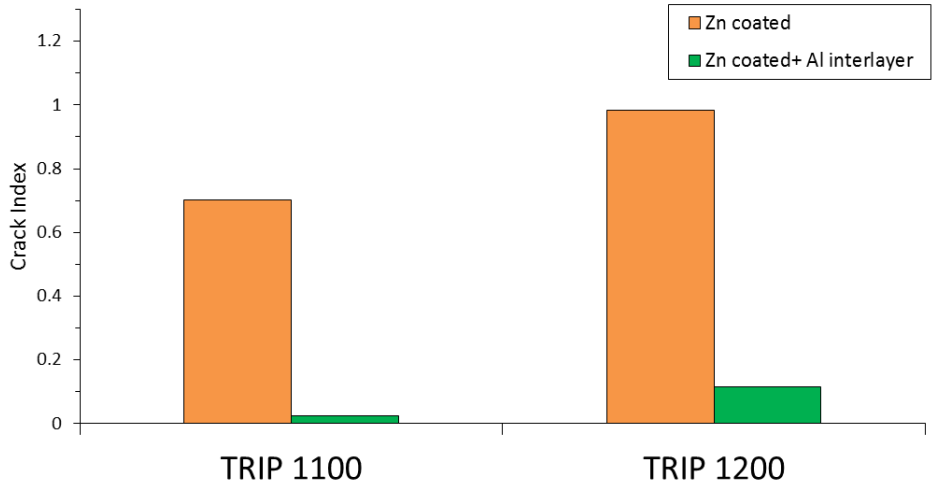


**Figure 6.6: Crack index for all material conditions**

## 6.2 Lap Shear Tensile Strength

LME cracks, from the zinc coating, was responsible for 30% decrease in lap shear strength in both the TRIP 1100 and TRIP 1200 as seen in Figure 6.7. With the use of aluminum interlayers, a full strength recovery was observed for TRIP 1100 while a 90% strength recovery was observed for TRIP 1200. The cause of the incomplete strength recovery in TRIP 1200 is the existence of some small remaining cracks after the application of aluminum interlayer as shown in Figure 6.5. The incomplete strength recovery of TRIP 1200 compared to TRIP 1100 is consistent with their crack index where the crack index of TRIP 1200 remained higher than TRIP 1100 after the application of aluminum interlayer. However, a full strength recovery should be possible for TRIP 1200 with optimized aluminum interlayer thickness and welding parameters.

RSW made with aluminum interlayers was able to highly reduce the degree of LME cracking, resulting in a strength recovery up to that of the welds in the uncoated material. As a result, welds with aluminum interlayers are fit to carry static loads in service life.

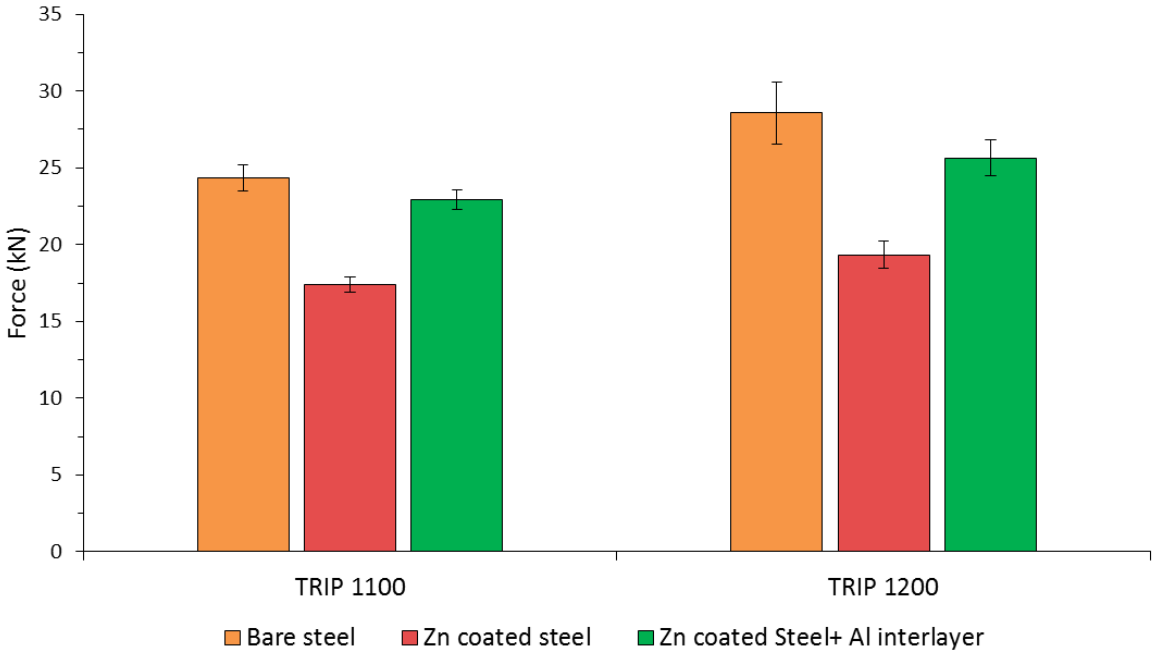


**Figure 6.7 Mean lap shear strength comparison for TRIP 1100 & TRIP 1200 in bare, coated and aluminum interlayer conditions**

## 6.3 Analysis of LME Crack Suppression

To understand the reactions responsible for the observed decrease in LME, SEM and EDX analysis were conducted on the surface region of zinc coated and aluminum interlayer cross-sections. For the zinc coated sample in Figure 6.8, a layer of iron-zinc intermetallic was detected on the steel surface, signifying that liquid zinc was in contact with steel during heating, making the material susceptible to LME. Cross-sections of the sample welded using aluminum interlayer in Figure 6.9 showed a layer of iron-aluminum intermetallic on the surface of the steel, while there was no clear indication of the presence of zinc. Figure 6.8 and Figure 6.9 show that the addition of aluminum caused iron to form iron-aluminum intermetallic at the steel surface, instead of the iron-zinc intermetallic, which formed when aluminum interlayers were not used. The formation of iron-aluminum intermetallic played a role in protecting the steel substrate from LME cracking.

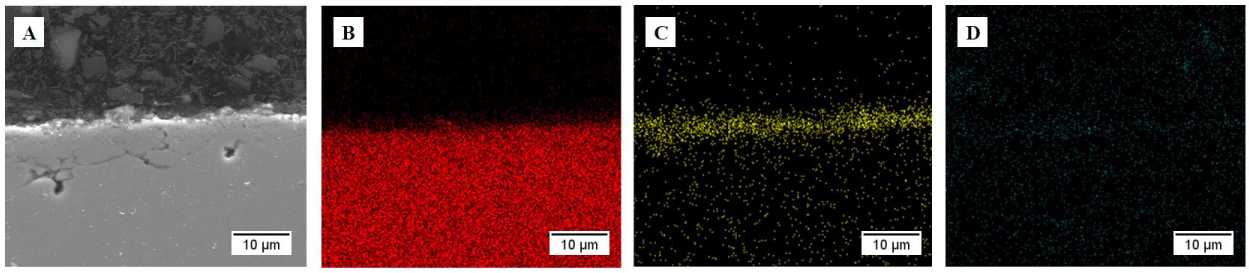


**Figure 6.8 (A) SEM image of welded sample of zinc coated TRIP1100 (B) EDX map for iron (C) EDX map for zinc showing zinc distribution on steel surface (D) EDX map for aluminum showing only noise is detected**

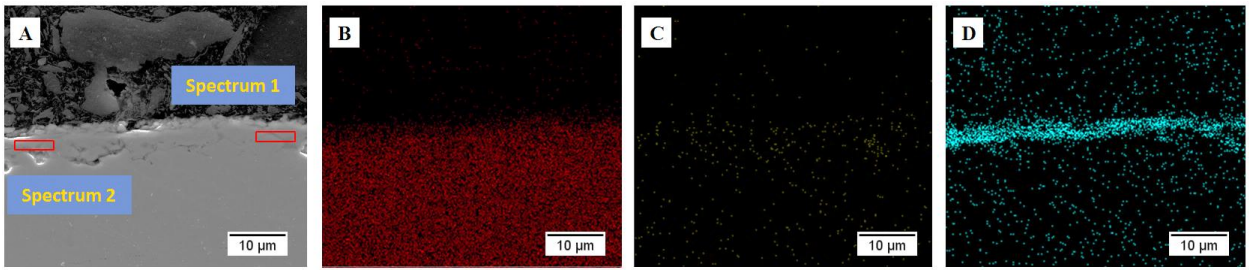


**Figure 6.9 (A) SEM image of welded sample of TRIP1100 with aluminum interlayer (B) EDX map for iron (C) EDX map for zinc showing only noise is detected (D) EDX map for aluminum showing aluminum distribution on steel surface**

At locations where sufficient liquid zinc initiated LME cracking, iron-aluminum intermetallic and trace amounts of zinc was observed in the LME cracks of aluminum interlayer samples. Figure 6.10 are images of an aluminum interlayer sample containing one LME crack 20 µm in length. As shown in Figure 6.10(c,d), LME cracking for aluminum interlayer samples is mostly filled up by aluminum and only shows trace amounts of zinc. During welding, a pocket of liquid zinc likely initiated the LME crack before the

liquid aluminum sufficiently mixed with the liquid zinc. After sufficient time, the liquid aluminum and zinc mixed and then the liquid aluminum-zinc alloy was drawn into the crack. The aluminum from the aluminum-zinc mixture reacted with the base material along the crack walls to form the observed iron-aluminum intermetallic. Not only did the aluminum-zinc mixture result in forming a protective layer on the crack wall, but it also reduced the zinc content that the steel was exposed to, preventing further propagation of the LME crack.

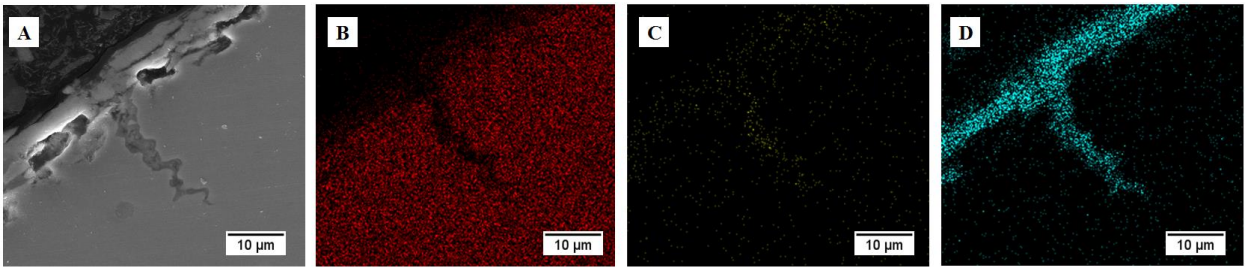


**Figure 6.10 (A) SEM image of welded sample of aluminum interlayer TRIP1100 with LME crack (B) EDX map for iron (C) EDX map for zinc showing trace amounts of detected zinc in LME crack (D) EDX map for aluminum showing aluminum distribution in LME crack**

From the analysis of welds made with aluminum interlayers, iron-aluminum intermetallic were seen both on the steel surface and in the LME cracks, resulting in the rejection of zinc from these areas and protection of the steel substrate from LME. To characterize the iron-aluminum intermetallic, EDX analysis was conducted in Figure 6.9(a) and the results are listed in [15,79,88,89].

Table 6.1. EDX results show that the intermetallic layer has an aluminum atomic percentage between 60-70% while minimal zinc was detected. Referring to the iron-aluminum phase diagram in Figure 6.11 [84], the intermetallic is most likely consisting of a mixture of FeAl, $FeAl_2$, and $Fe_2Al_5$ iron aluminides. It has been reported in literature that iron aluminides have formation energies an order of magnitude more negative than iron-zinc intermetallic [85–87], meaning that iron preferentially reacts with aluminum rather than zinc. This explains the observations in Figure 6.9 and Figure 6.10 that showed even in a zinc rich environment, iron formed intermetallic with aluminum instead of zinc. The observation from this study are consistent with mechanisms observed during hot dip galvanization of steel, where aluminum is added to zinc galvanizing bath to "inhibit" iron-zinc intermetallic compounds from forming [15,79,88,89]. During hot dip galvanizing the iron-aluminum intermetallic layer acts as an inhibition layer and hinders reaction between the steel sheet and molten zinc [15,79,88,89].

**Table 6.1 EDX Spectrums showing atomic percentage of various elements from Figure 6.9(a).**

| Spectrum | Fe at.% | Al at.% | Zn at.% | Cu at.% |
|---|---|---|---|---|
| Spectrum 1 | 35.31 | 59.68 | 0.89 | 4.12 |
| Spectrum 2 | 24.71 | 71.35 | 0.58 | 3.37 |

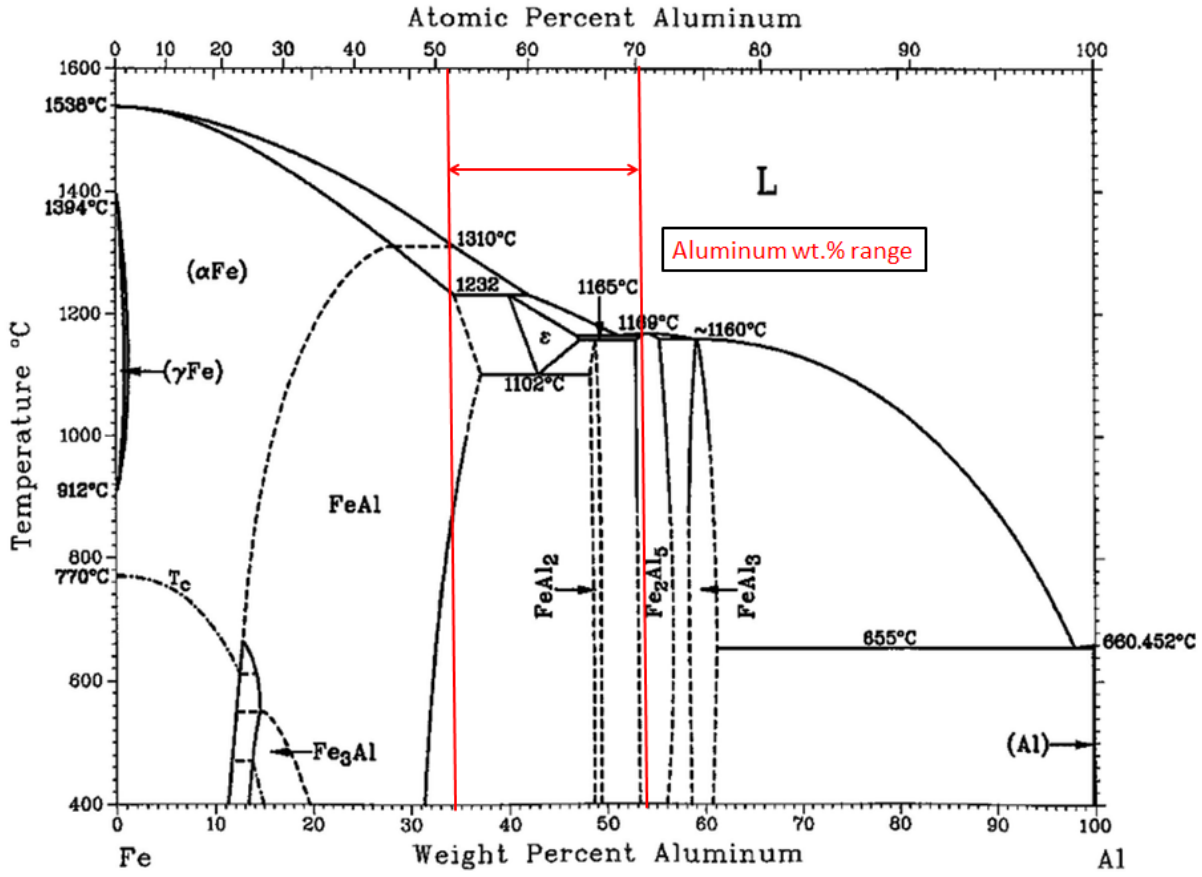


**Figure 6.11 Fe-Al phase diagram*[84]***

Liquid zinc is a main factor in the initiation of LME, as zinc was not observed in the electrode indent for the aluminum interlayer samples, it is critical to locate it in the weld. During the RSW process, the coatings under the electrode indent melt and get squeezed outside the shoulder of the electrode indent. The formation of iron aluminides acts as a wetting barrier that helps the coating get completely squeezed out [90], leaving no zinc under the electrode indent. While only zinc was detected in the squeeze-out for zinc coated samples in Figure 6.12, both zinc and aluminum was detected in the squeeze-out for aluminum interlayer samples in Figure 6.13. EDX analysis was conducted on the squeeze-out from the aluminum interlayer sample in Figure 6.13 and the results are listed in Table 6.2. EDX results show that the weight ratio between the zinc and aluminum in the squeeze out is approximately 1:1, same as the weight ratio

between the original zinc coating and aluminum interlayer prior to welding. Furthermore, the cross-sectional area of the squeeze out in Figure 6.13, measuring 0.167 $cm^2$, is similar with the combined cross-sectional area of the zinc coating and aluminum interlayer in the electrode indent prior to welding, which was calculated to be 0.149 $cm^2$. This shows that the squeeze-out detected outside the shoulder of the weld is the aluminum-zinc liquid alloy that came from the electrode indent during welding.

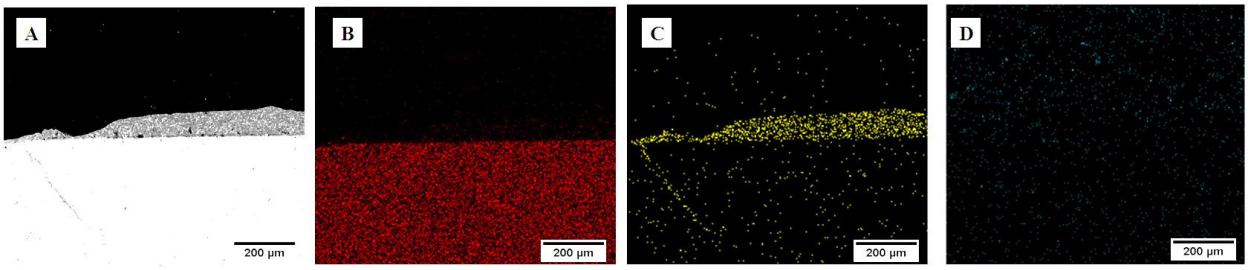


**Figure 6.12 (A) SEM image of welded sample of zinc coated TRIP1100 outside the shoulder of the electrode indent (B) EDX map for iron (C) EDX map for zinc showing zinc distribution in squeeze out (D) EDX map for aluminum showing only noise is detected**

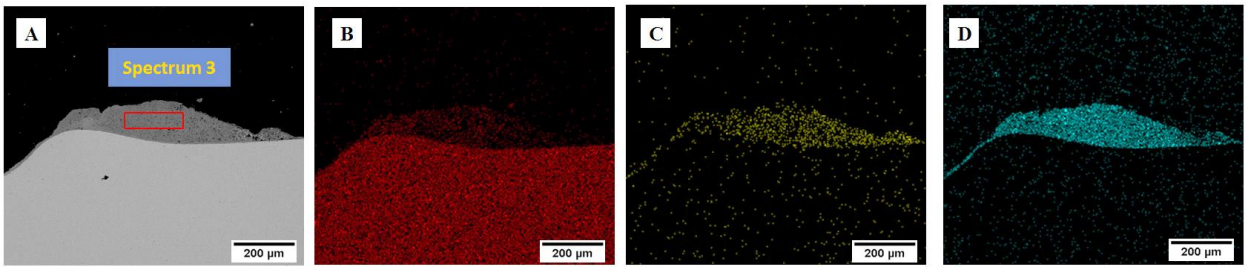


**Figure 6.13 (A) SEM image of welded sample of aluminum interlayer TRIP1100 outside the shoulder of the electrode indent (B) EDX map for iron (C) EDX map for zinc showing zinc distribution in squeeze out (D) EDX map for aluminum showing aluminum distribution in squeeze out**

**Table 6.2 EDX analysis from Figure 6.13(b)**

| Spectrum | Fe wt.% | Al wt.% | Zn wt.% | Cu wt.% |
|---|---|---|---|---|
| Spectrum 3 | 5.55 | 40.12 | 41.60 | 12.73 |

Results from the analysis of LME crack suppression show that the aluminum interlayers result in the formation of iron aluminides. Iron aluminides hinder liquid zinc from contacting the steel substrate during

welding, preventing LME. The remaining aluminum-zinc liquid alloy is pushed outside the shoulder of the weld indent before solidification.

## 6.4 Summary

Aluminum interlayers can significantly suppress LME cracking of TRIP steel, shown by the reduced frequency and length of the LME cracks seen after welding. Zinc coated TRIP samples with aluminum interlayers were resistance spot welded and tested alongside coated samples and uncoated samples. While the strength of welds in zinc coated steels were considerably lower than the weld strengths in uncoated steel, due to LME cracking, welding with an aluminum interlayer resulted in either similar or slightly lower weld strengths measured from welds that were not affected by LME. Analysis of LME crack suppression shows that aluminum interlayers suppress LME in TRIP steel welds by the formation of iron aluminides that hinder liquid zinc from coming in contact with the steel substrate, preventing LME.

# Chapter 7 Conclusion and Future Work

## 7.1 Conclusion

Six combinations of steels and coatings are invested in this study to not only gauge their LME susceptibility, but also identify factors that influence the LME susceptibility of steels in general.

Hot tensile testing was the first tool used. It has the benefit of evaluating a material's LME susceptibility regardless of the welding schedule. Through hot tensile testing, ductile fracture was observed for the bare steels whereas brittle, intergranular fracture was observed for steels affected by LME.

By examining hot tensile testing data together with dilatometry results, it was discovered that the austenite content of the steels' microstructure, Si content in the steels' chemistry and the type of Zn coating all influence the behavior of the ductility trough of the examined steels. As the austenite content of the steel increased, the ductility loss caused by LME increased as well. Approximately 18 vol.% to 31 vol.% austenite is the minimum amount required to trigger the rise in ductility loss of all the studied steels. In addition, steels containing a low Si content are more likely to form a layer of Fe-Zn intermetallic that acts as a barrier to suppresses LME at temperatures below 670°C. It was also discovered that the GA coated steels are far less susceptible to LME than their GI coated counterparts due to it being thinner and containing 25 wt.% Fe in its coating.

Using the hot tensile testing data, the LME susceptibility of the steels are ranked via their average ductility loss. QP1180GA is the most LME susceptible steel while DP980GA is the least. To complement the hot tensile testing results, resistance spot welding tests were done. The cracking index from resistance spot welding shows the same material ranking in LME susceptibility as the hot tensile testing data. This shows that the LME susceptibility obtained from hot tensile testing is relevant to resistance spot welding and vice versa. Furthermore, the comparison between hot tensile testing and welding results is a novel contribution that has not been achieved before.

A mathematical model capable of estimating the crack index within the weld lobe of each material was also developed through resistance spot welding. The model showed that the weld lobe of materials where not equally affected by LME. Furthermore, it identified regions within the weld lobe where welds of sufficient size could be made while minimizing LME cracks.

GA coated steels being less susceptible to LME than their GI coated counterpart showed that its possible to suppress LME by changing the chemistry of the coating. It was discovered that aluminum interlayers can significantly suppress LME cracking of TRIP steel, shown by the reduced frequency and

length of the LME cracks seen after welding. Zinc coated TRIP samples with aluminum interlayers were resistance spot welded and tested alongside coated samples and uncoated samples. While the strength of welds in zinc coated steels were considerably lower than the weld strengths in uncoated steel, due to LME cracking, welding with an aluminum interlayer resulted in either similar or slightly lower weld strengths measured from welds that were not affected by LME. Analysis of LME crack suppression shows that aluminum interlayers suppress LME in TRIP steel welds by the formation of iron aluminides that hinder liquid zinc from coming in contact with the steel substrate, preventing LME.

## 7.2 Future Work

This work has shown that the ductility loss caused by LME increases with the austenite content of the steel. While austenite is an important factor in the occurrence of LME, QP steels were observed to be susceptible to LME at 500°C and 600°C having less than 10% austenite. Barthelmie et al. also observed ductility loss of FeMn steel at temperatures as low as 450°C during hot tensile testing [53]. These observations indicate that the current theories on the effect of austenite content on LME susceptibility is incomplete, especially for temperatures below 600°C. Furthermore, theories on the effect of austenite content on LME susceptibility is predicated on steels that are only susceptible to LME above 700°C, a temperature where plenty of austenite is already present [2,37,45,49]. While austenite phase content influences LME severity at elevated temperatures, it is possible that another LME mechanism exists at low temperatures where it is less dependent on the austenite phase content. In the future, more hot tensile tests should be conducted below 600°C for GI coated QP980 and QP1180 to fully investigate this phenomenon.

In terms of preventing LME, while using the aluminum interlayer is a viable method, more work is required to optimally apply this technology in an industrially setting. More testing must be carried out both on understanding the effect of welding with interlayers on various types of AHSS and on optimizing the interlayers for use with various joint combinations. There may also be alternative elements that are more effective in suppressing LME than aluminum.

# Chapter 8 References


[1] Santos. Moomba Plant update [Internet]. 2004. Available from: https://www.santos.com/media-centre/announcements/moomba-plant-update/.

[2] Beal C, Kleber X, Fabregue D, et al. Embrittlement of a zinc coated high manganese TWIP steel. Mater. Sci. Eng. A. 2012;543:76–83.

[3] Nicholas MGG, Old CFF, Division MD. Review Liquid metal embrittlement. J. Mater. Sci. [Internet]. 1979;14:1–18. Available from: http://www.springerlink.com/content/h30067133t135w9h/.

[4] Autobody/Steel Partnership: AHSS Joining - Resistance Spot Weld Schedules for AHSS [Internet]. 2007. Available from: http://www.a-sp.org/~/media/Files/ASP/Enabling Programs/AHSS Joining - Resistance Spot Weld Schedules for AHSS.pdf.

[5] American Welding Society. American Welding Society: Test Method for Evaluating the Resistance Spot Welding Behavior of Automotive Sheet Steel Materials (AWS D 8.9M). 2012. p. 1–107.

[6] Cooper AI. Cooperative carbon capture. Nature. 2015;519:295.

[7] Jakob, Michael; Hilaire J. Unburnable fossil-fuel reserves. Nature. 2015;517:150.

[8] McNutt M. Climate change impacts. Science. 2013;341:435.

[9] Keeler S, Kimchi M, J. Mooney P. Advanced High-Strength Steels Apllication Guidelines Version 6.0. World Auto Steel [Internet]. 2017;6:314. Available from: http://www.worldautosteel.org/download_files/AHSS Guidelines V6/00_AHSSGuidelines_V6_20170430.pdf.

[10] Bhadeshia H, Honeycombe R. Microstructure and Properties. 4th ed. Elsevier; 2017.

[11] Galán J, Samek L, Verleysen P, et al. Advanced high strength steels for automotive industry. Rev. Metal. 2012;48:118–131.

[12] Sugimoto K, Kobayashi M, Hashimoto S. Ductility and Strain-Induced Transformation in a High-Strength Transformation-. Metall. Mater. Trans. A. 1992;23:3085–3091.

[13] Edmonds D V., He K, Rizzo FC, et al. Quenching and partitioning martensite-A novel steel heat treatment. Mater. Sci. Eng. A. 2006;438–440:25–34.

[14] Tan X, Ponge D, Lu W, et al. Carbon and strain partitioning in a quenched and partitioned steel containing ferrite. Acta Mater. 2019;165:561–576.

[15] Marder AR. The metallurgy of zinc-coated steel. 2004;45. Available from: https://www.taylorfrancis.com/books/E-EPCS.

[16] Simko M, Silva EA, Wolf RH, et al. Sheet Steel: Coated. Encycl. Mater. Sci. Technol. [Internet]. Elsevier; 2001. p. 8451–8456. Available from: https://app.knovel.com/hotlink/toc/id:kpEMSTV001/encyclopedia-materials/encyclopedia-materials.

[17] Zhang H, Senkara J. Electrothermal Processes of Welding. Resist. Weld. Fundam. Appl. Boca Raton: CRC Press; 2006. p. 19–57.

[18] Pouranvari M, Marashi SPH. Critical review of automotive steels spot welding: Process, structure and properties. Sci. Technol. Weld. Join. 2013;18:361–403.

[19] Williams NT, Parker JD. Review of resistance spot welding of steel sheets Part 1 Modelling and control of weld nugget formation. Int. Mater. Rev. [Internet]. 2004;49:45–75. Available from: http://www.tandfonline.com/doi/full/10.1179/095066004225010523.

[20] Donders S, Brughmans M, Hermans L, et al. The effect of spot weld failure on dynamic vehicle performance. Conf. Proc. Soc. Exp. Mech. Ser. 2005;16–24.

[21] Luo Y, Liu J, Xu H, et al. Regression modeling and process analysis of resistance spot welding on galvanized steel sheet. Mater. Des. [Internet]. 2009;30:2547–2555. Available from: http://dx.doi.org/10.1016/j.matdes.2008.09.031.

[22] Wintjes E. A Statistical Approach to Quantifying Impact of Multiple Pulse Resistance Spot Welding Schedules on Liquid Metal Embrittlement Cracking by. University of Waterloo; 2019.

[23] Hou JS. Resistance Spot Welding and In-Process Heat Treatment of Hot Stamped Boron Steel. University of Waterloo; 2016.

[24] Zhang H, Senkara J. Resistance Spot Welding Fundamentals and Applications. 2nd ed. Boca Raton: CRC Press; 2011.

[25] Cho Y, Rhee S. Experimental Study of Nugget Formation. Weld. J. 2003;195–201.

[26] Dickinson DW, Franklin JE, Stanya A. Characterization of Spot Welding Behavior By Dynamic Electrical Parameter Monitoring. Weld. J. 1980;59.

[27] Russo Spena P, De Maddis M, D'Antonio G, et al. Weldability and Monitoring of Resistance Spot Welding of Q&P and TRIP Steels. Metals (Basel). 2016;6:270.

[28] Zhang H. Expulsion and its influence on weld quality. Weld. J. (Miami, Fla). 1999;78:373-s.

[29] Marashi P, Pouranvari M, Sanaee SMH, et al. Relationship between failure behaviour and weld fusion zone attributes of austenitic stainless steel resistance spot welds. Mater. Sci. Technol. 2008;24:1506–1512.

[30] Mallick PK. Joining for Lightweight Vehicles. In: Mallick PK, editor. Mater. Des. Manuf. Light. Veh. 1st ed. Boca Raton: CRC Press; 2010. p. 275–308.

[31] Chabok A, van der Aa E, Basu I, et al. Effect of pulse scheme on the microstructural evolution, residual stress state and mechanical performance of resistance spot welded DP1000-GI steel. Sci. Technol. Weld. Join. 2018;23:649–658.

[32] Hwang IS, Kang MJ, Kim DC. Expulsion reduction in resistance spot welding by controlling of welding current waveform. Procedia Eng. [Internet]. 2011;10:2775–2781. Available from: http://dx.doi.org/10.1016/j.proeng.2011.04.461.

[33] Ashiri R, Shamanian M, Salimijazi HR, et al. Liquid metal embrittlement-free welds of Zn-coated twinning induced plasticity steels. Scr. Mater. [Internet]. 2016;114:41–47. Available from: http://dx.doi.org/10.1016/j.scriptamat.2015.11.027.

[34] Scotchmer N. Widening the Welding Lobe of Advanced High Strength Steels in the Resistance Spot Welding Process. Huys Ind. Ltd. :1–11.

[35] American Welding Society. Test Methods for Evaluating the Resistance Spot Welding Behavior of Automotive Sheet Steel Materials (AWS D8.9M:2012). 2012;7.

[36] Nicholas MG, Old CF. Liquid metal embrittlement. J. Mater. Sci. 1979;14:1–18.

[37] Beal C, Kleber X, Fabregue D, et al. Liquid zinc embrittlement of twinning-induced plasticity steel. Scr. Mater. [Internet]. 2012;66:1030–1033. Available from: http://dx.doi.org/10.1016/j.scriptamat.2011.12.040.

[38] Joseph B, Barbier F, Dagoury G, et al. Rapid penetration of liquid Bi along Cu grain boundaries. Scr. Mater. 1998;39:775–781.

[39] Joseph B, Barbier F, Aucouturier M. Embrittlement of copper by liquid bismuth. Scr. Mater. 1999;40:893–897.

[40] Hugo RC, Hoagland RG. In-situ TEM observation of aluminum embrittlement by liquid gallium. Scr. Mater. 1998;38:523–529.

[41] Ludwig W, Pereiro-López E, Bellet D. In situ investigation of liquid Ga penetration in Al bicrystal grain boundaries: Grain boundary wetting or liquid metal embrittlement? Acta Mater. 2005;53:151–162.

[42] M.H K. Liquid Metal Embrittlement. Met. Handb. 9th ed. Materials Park, OH: ASM International; 1987. p. 171–184.

[43] Hilditch JP, Hurley JR, Skeldon P, et al. The liquid metal embrittlement of iron and ferritic steels in sodium. Corros. Sci. 1995;37:445–454.

[44] Carpio J, Casado JA, Álvarez JA, et al. Stress corrosion cracking of structural steels immersed in hot-dip galvanizing baths. Eng. Fail. Anal. [Internet]. 2010;17:19–27. Available from: http://dx.doi.org/10.1016/j.engfailanal.2008.11.005.

[45] Kang H, Cho L, Lee C, et al. Zn Penetration in Liquid Metal Embrittled TWIP Steel. Metall. Mater. Trans. A Phys. Metall. Mater. Sci. 2016;47:2885–2905.

[46] Béal C. Mechanical behaviour of a new automotive high manganese TWIP steel in the presence of liquid zinc. 2011; Available from: https://tel.archives-ouvertes.fr/tel-00679521.

[47] Jung G. Liquid metal embrittlement of high Mn TWIP steel. POSTECH. Pohang: Graduate Institute of Ferrous Technology; 2015.

[48] Bhattacharya D, Cho L, Ghassemi-armaki H, et al. QUANTITATIVE ASSESSMENT OF THE CHARACTERISTICS OF LIQUID METAL EMBRITTLEMENT DURING RESISTANCE SPOT WELDING OF Zn-COATED HIGH-STRENGTH STEELS. Sheet Met. Weld. Conf. XVIII. 2018;

[49] Beal C, Kleber X, Fabrègue D, et al. Embrittlement of a High Manganese TWIP Steel in the Presence of Liquid Zinc. Mater. Sci. Forum [Internet]. 2012;706–709:2041–2046. Available from: http://www.scientific.net/MSF.706-709.2041.

[50] Sierlinger R, Gruber M. A Cracking Good Story About Liquid Metal Embrittlement During Spot Welding of Advanced High Sterength Steels. Join. car body Eng. 2017;1–15.

[51] Kim YG, Kim IJ, Kim JS, et al. Evaluation of Surface Crack in Resistance Spot Welds of Zn-Coated Steel. Mater. Trans. 2014;55:171–175.

[52] Tolf E, Hedegård J, Melander A. Surface breaking cracks in resistance spot welds of dual phase steels with electrogalvanised and hot dip zinc coating. Sci. Technol. Weld. Join. [Internet]. 2013;18:25–31. Available from: http://www.tandfonline.com/doi/full/10.1179/1362171812Y.0000000068.

[53] Barthelmie J, Schram A, Wesling V. Liquid Metal Embrittlement in Resistance Spot Welding and Hot Tensile Tests of Surface-refined TWIP Steels. IOP Conf. Ser. Mater. Sci. Eng. 2016;118.

[54] Choi D-Y, Sharma A, Uhm S-H, et al. Liquid Metal Embrittlement of Resistance Spot Welded 1180 TRIP Steel: Effect of Electrode Force on Cracking Behavior. Met. Mater. Int. [Internet]. 2019;25:219–228. Available from: http://link.springer.com/10.1007/s12540-018-0180-x.

[55] Bhattacharya D. Liquid metal embrittlement during resistance spot welding of Zn-coated high-strength steels. Mater. Sci. Technol. [Internet]. 2018;34:1809–1829. Available from: https://www.tandfonline.com/doi/full/10.1080/02670836.2018.1461595.

[56] Sigler DR. Observations of Liquid Metal-Assisted Cracking in Resistance Spot Welds of Zinc-Coated Advanced High-Strength Steels. Sheet Met. Weld. Conf. XIII. 2008;1–17.

[57] Jung G, Woo IS, Suh DW, et al. Liquid Zn assisted embrittlement of advanced high strength steels with different microstructures. Met. Mater. Int. 2016;22:187–195.

[58] Ashiri R, Haque MA, Ji CW, et al. Supercritical area and critical nugget diameter for liquid metal embrittlement of Zn-coated twining induced plasticity steels. Scr. Mater. [Internet]. 2015;109:6–10. Available from: http://dx.doi.org/10.1016/j.scriptamat.2015.07.006.

[59] DiGiovanni C, Han X, Powell A, et al. Experimental and Numerical Analysis of Liquid Metal Embrittlement Crack Location. J. Mater. Eng. Perform. [Internet]. 2019;28:2045–2052. Available from: https://doi.org/10.1007/s11665-019-04005-2.

[60] Choi D, Sharma A, Jung JP. Parametric Study for Liquid Metal Embrittlement in. Sheet Met. Weld. Conf. XVIII. 2018;1–9.

[61] Frei J, Rethmeier M. Susceptibility of electrolytically galvanized dual-phase steel sheets to liquid metal embrittlement during resistance spot welding. Weld. World. 2018;62:1031–1037.

[62] Wintjes E, DiGiovanni C, He L, et al. Quantifying the Link Between Crack Distribution and Resistance Spot Weld Strength Reduction in Liquid Metal Embrittlement Susceptible Steels. Weld. World. 2019;63:807–814.

[63] Kaščák Ľ, Spišák E. Evaluation of the Influence of the Welding Current on the Surface Quality of Spot Welds. 2016;32–37.

[64] DiGiovanni C, Biro E, Zhou N. Impact of liquid metal embrittlement cracks on resistance spot weld static strength. Sci. Technol. Weld. Join. [Internet]. 2018;24:218–224. Available from: https://doi.org/13621718.2018.1518363.

[65] Wintjes E, DiGiovanni C, He L, et al. Effect of Multiple Pulse Resistance Spot Welding Schedules on Liquid Metal Embrittlement Severity. J. Manuf. Sci. Eng. 2019;141:1–9.

[66] DiGiovanni C, He L, Pistek U, et al. Role of spot weld electrode geometry on liquid metal embrittlement crack development. J. Manuf. Process. 2020;49:1–9.

[67] E.Wintjes, C.DiGiovanni, L.He, A.Macwan, E.Biro YZ. Quantifying the Link Between Crack Distribution and Resistance Spot Weld Strength Reduction in LME Susceptible Steels. 2018;

[68] Ina K, Koizumi H. Penetration of liquid metals into solid metals and liquid metal embrittlement. Mater. Sci. Eng. A. 2004;387–389:390–394.

[69] Li X, Lawson S, Zhou Y, et al. Novel technique for laser lap welding of zinc coated sheet steels. J. Laser Appl. [Internet]. 2007;19:259–264. Available from: http://lia.scitation.org/doi/10.2351/1.2795755.

[70] Kasuya T, Yurioka N. Carbon equivalent and multiplying factor for hardenability of steel. Weld. J. (Miami); (United States). 1993;72:6:263–268.

[71] R.H. Myers, D.C. Montgomery CMA-C. Response Surface Methodology. 3rd ed. Wiley, New York; 2009.

[72] Boriwal L, Sarviya RM, Mahapatra MM. Failure modes of spot welds in quasi - Static tensile - Shear loading of coated steel sheets. Shear l. Mater. Today Proc. 2017;4:3672–3677.

[73] Nissley NE, Collins MG, Guaytima G, et al. Development of the strain-to-fracture test for evaluating ductility-dip cracking in austenitic stainless steels and Ni-base alloys. Weld. World. 2002;46:32–40.

[74] Beal C, Kleber X, Fabregue D, et al. Liquid zinc embrittlement of twinning-induced plasticity steel. Scr. Mater. 2012;66:1030–1033.

[75] Caballero FG, Capdevila C, García de Andrés C. Kinetics and dilatometric behaviour of non-isothermal ferrite-austenite transformation. Mater. Sci. Technol. 2001;17:1114–1118.

[76] Tariq F. Microstructural evolution during tempering of Quenched and Partitioned Medium Carbon Low Alloy Steel. 2013;

[77] Mesplont C, Jiu Zou Zhao, Vandeputte S, et al. An improved method for determining the continuous cooling transformation diagram of C-Mn steels. Steel Res. 2001;72:263–270.

[78] Dai Z, Ding R, Yang Z, et al. Thermo-kinetic design of retained austenite in advanced high strength steels. Acta Mater. [Internet]. 2018;152:288–299. Available from: https://doi.org/10.1016/j.actamat.2018.04.040.

[79] Jordan CE, Marder AR. Effect of iron oxide as an inhibition layer on iron-zinc reactions during hot-dip galvanizing. Metall. Mater. Trans. B Process Metall. Mater. Process. Sci. 1998;29:479–484.

[80] Lin KC, Lin CS. Effect of silicon in dual phase steel on the alloy reaction in continuous hot-dip galvanizing and galvannealing. ISIJ Int. 2014;54:2380–2384.

[81] Bondareva OS, Melnikov AA. Effect of the silicon content in steel on the hot-dip zinc coating microstructure formation. IOP Conf. Ser. Mater. Sci. Eng. 2016;156.

[82] Lee CW, Fan DW, Sohn IR, et al. Liquid-metal-induced embrittlement of Zn-coated hot stamping steel. Metall. Mater. Trans. A Phys. Metall. Mater. Sci. 2012;43:5122–5127.

[83] Razmpoosh MH, Macwan A, Biro E, et al. Liquid metal embrittlement in laser beam welding of Zn-coated 22MnB5 steel. Mater. Des. [Internet]. 2018;155:375–383. Available from: https://doi.org/10.1016/j.matdes.2018.05.065.

[84] Henager C. Hydrogen Permeation Barrier Coatings. Mater. Hydrog. Econ. [Internet]. 2007;181–190. Available from: http://www.crcnetbase.com/doi/10.1201/9781420006070.ch8.

[85] Klaver TPC, Madsen GKH, Drautz R. A DFT study of formation energies of Fe-Zn-Al intermetallics and solutes. Intermetallics. 2012;31:137–144.

[86] Miao Y, Han D, Xu X, et al. Phase constitution in the interfacial region of laser penetration brazed magnesium-steel joints. Mater. Charact. [Internet]. 2014;93:87–93. Available from: http://dx.doi.org/10.1016/j.matchar.2014.03.019.

[87] Saunders N. Thermochemical database for light metal alloys. COST 507 Thermochem. Databased Light Met. Alloy. 1998.

[88] Culcasi JD, Seré PR, Elsner CI, et al. Control of the growth of zinc-iron phases in the hot-dip

galvanizing process. Surf. Coatings Technol. 1999;122:21–23.

[89] Ghuman ARP, Goldstein JI. Reaction mechanisms for the coatings formed during the hot dipping of iron in 0 to 10 Pct Al-Zn baths at 450° to 700°C. Metall. Trans. 1971;2:2903–2914.

[90] Yang J, Xue S, Wu Y, et al. Wetting behaviour of Zn–Al filler metal on a stainless steel substrate. Sci. Technol. Weld. Join. [Internet]. 2018;23:1–6. Available from: https://doi.org/10.1080/13621718.2017.1314657.